CAAP Final Report

Date of Report: 6/28/2022

Prepared for: *U.S. DOT Pipeline and Hazardous Materials Safety Administration*

Contract Number: 693JK31850004CAAP

Project Title: *Internal Corrosion Monitoring in Pipelines by using Helical Ultrasonic Waves*

Prepared by: Stylianos Livadiotis

Salvatore Salamone (PI)

Contact Information: slivadiotis@utexas.edu

salamone@utexas.edu

Department of Civil, Architectural and Environmental Engineering

University of Texas at Austin

Ferguson Structural Engineering Laboratory,

10100 Burnet Road Building 177,

Austin, TX 78758

Executive Summary

The present report summarizes the activities and results obtained during the project: “Internal Corrosion Monitoring in Pipelines by using Helical Ultrasonic Waves” with contract 693JK31850004CAAP.

The research group worked towards developing a non-destructive evaluation (NDE) technology for detecting, evaluating, and monitoring the progression of internal and external corrosion in pipelines. This technology exploits a novel class of guided ultrasonic waves, the helical guided ultrasonic waves (HGUW), and a network of permanently attached piezoelectric sensors responsible for transmitting and receiving these waves. We investigated both active (i.e., sensors transmit the ultrasonic pulse) and passive (i.e., Acoustic emission - AE) use of the HGUW in combination with numerical modeling and advanced data processing techniques. The main achievements using the active method include the 1) corrosion localization, and 2) corrosion characterization (e.g., thickness mapping) while with the passive mode a qualitative observation of the corrosion evolution was achieved. The HGUW are categorized as short-range guided waves which differentiates them the traditional long-range guided waves used for pipeline inspection. This allows for using higher frequency (i.e., shorter wavelength) waves that can be effectively utilized for defect localization as well as thickness reconstructions. In addition, the helical propagation of the waves helps reducing the requirement for sensing units, making the deployment and operation of the monitoring system more feasible in practice.

The first chapters of this report (Chapters 2 and 3) illustrate the technical approach for using the HGUW in the active mode. Detailed discussion is presented on the localization and tomography algorithms as well as the numerical modeling. The second part of this report (Chapter 4) outlines the acoustic emission monitoring of corrosion using the HGUW. A summary of findings, major contributions and community outreach is presented in Chapter 5.

Table of Contents

List of Tables

List of Figures

Summary of Accomplishments

Major findings and results derived during this 4-year period have been published in peer-reviewed journal papers as well as presented in various conferences and symposiums around the US. The following list contains the published work and the names of the events where our group has participated in the form of conference papers, technical presentations, and posters.

Degrees awarded:

• S. Livadiotis, "Pipeline health monitoring using helical guided ultrasonic waves", PhD thesis, 2022

Peer-reviewed journal publications:

• S. Livadiotis, K. Sitaropoulos, A. Ebrahimkhanlou, and S. Salamone, "Acoustic emission monitoring of corrosion in steel pipes using Lamb-type helical waves", *Structural Health Monitoring*. June 2022. doi:10.1177/14759217221105644

• S. Livadiotis, A. Ebrahimkhanlou, and S. Salamone, "Monitoring internal corrosion in steel pipelines: A two-step helical guided wave approach for localization and quantification," *Structural Health Monitoring*, Nov. 2020, doi:10.1177/1475921720970139.

• S. Livadiotis, A. Ebrahimkhanlou, and S. Salamone, "An algebraic reconstruction imaging approach for corrosion damage monitoring of pipelines," Smart Mater. Struct., vol. 28, no. 5, p. 055036, 2019. doi:10.1088/1361-665X/ab1160

Conference papers & Presentations:

• S. Livadiotis, A. Ebrahimkhanlou, and S. Salamone, "A helical-based ultrasonic imaging algorithm for structural health monitoring of cylindrical structures," Proc. SPIE. Denver, 2019, vol. 1, no. 1, pp. 2–8, 2019.

• S. Livadiotis, A. Ebrahimkhanlou, and S. Salamone, "Structural health monitoring of pipelines by means of helical guided ultrasonic waves and an algebraic reconstruction technique," Struct. Heal. Monit. 2019 Proc. 12th Int. Work. Struct. Heal. Monit., vol. 2, no. December, pp. 1885–1892, 2019.

Conference Presentations:

• S. Livadiotis, Tony Lee, and S. Salamone, “Internal corrosion monitoring using helical ultrasonic waves”, (presented at the 2021 Hydrogen and Emerging Fuels R&D Public Meeting and Forum, November 30, 2021)

• S. Livadiotis, and S. Salamone, “Corrosion assessment in cylindrical structures using helical guided ultrasonic waves”, (presented at the 2021 PRCI Virtual Research Exchange, March 2–5, 2021)

• S. Livadiotis, A. Ebrahimkhanlou, and S. Salamone, “A helical-based ultrasonic imaging algorithm for structural health monitoring of large-diameter metallic pipelines" (presented at the Structures Congress 2019, Structural Engineering Institute (SEI) of ASCE, Hyatt Regency, Orlando, Florida April 24–27, 2019

Posters:

• S. Livadiotis, A. Ebrahimkhanlou, and S. Salamone, “Internal Corrosion Monitoring in Pipelines by using Helical Ultrasonic Waves,” (Presented at the Government/Industry Pipeline R&D Forum, Arlington, Virginia, US, February 19, 2020).

• S. Livadiotis, A. Ebrahimkhanlou, and S. Salamone, “An Integrated Corrosion Monitoring System for Pipelines,” (Presented at the University of Texas at Austin Energy Research Expo, Austin, TX, US, October 2, 2019).

Student Engagement

• Tony Lee (PhD student in Civil Engineering) – 3rd and 4th year of the project

• Konstantinos Sitaropoulos (PhD student in Civil Engineering) – 3rd and 4th year of the project

1. Introduction

1.1. Motivation

Pipelines are predominantly used for the gathering, transmission, and distribution of oil and gas products around the globe. It is estimated that more than 3.5 million kilometers of pipelines are currently in service [1]. These pipes run in a variety of settings like below or above the ground and underwater. The assessment of the structural integrity of pipeline systems is of vital importance due to the impact that natural resources have on a country's economy. Besides, recent pipeline accidents have caused enormous environmental destruction that is extremely difficult to overcome. Considering that pipes stretch for thousands of miles in addition to the limited accessibility in certain areas, there exists a need for developing highly efficient health monitoring schemes that are able to monitor in-real time the structural integrity of these systems and assist the operator's decision making.

Hundreds of pipeline accidents are reported every year which involve damages due to excavation, incorrect operation, and material failure. Of the non-human related accidents, corrosion is the leading cause of steel pipe failures [2]. Corrosion is the electrochemical reaction of the pipe, typically steel, with the environment that results in the destruction and deterioration of the metal. Corrosion can develop in both inner and outer surfaces of a pipe due to the CO_2 contained in natural or refined resources and different environmental conditions. Corrosion develops in various forms like pits, stress cracking, crevice, and uniform. Figure 1.1 shows pictures taken from an oil refinery depicting an externally corroded pipe with additional localized pits. The required effort to localize and quantify the corrosion becomes enormous especially when it develops internally. Currently, the industry relies on preventive methods to mitigate corrosion such as coatings, cathodic protection, and the use of inhibitors. While these methods can be effective, they still carry the overall uncertainty regarding the location and severity of the corrosion at critical regions of the pipe. A more advance method for inspecting segments of pipes involves in-line inspection (ILI) using smart pigs that are inserted into the stream and are responsible for assessing critical regions of the pipe. Even though this is a highly effective inspection method it still requires expensive equipment and well-trained personnel to undertake this task.

Figure 1.1: External corrosion of in-service steel pipe and localized pits on the surface. (Pictures from a field test at Monroe Energy in Philadelphia. The test was performed by the smart structures research group and the author was leading this effort.)

In the context of Non-Destructive Evaluation (NDE) and Structural Health monitoring (SHM), active acoustic methods involve the use of networks of sensors that transmit and receive ultrasonic waves to interrogate the structure. Guided ultrasonic waves (GUW) techniques have been one of the most successful for pipeline inspection and have been extensively studied and commercialized [3], [4]. Some of the most widely used non-destructive testing systems include the Wavemaker from Guided Ultrasonics as well as the MagnetoStrictive Sensor System (MsS) from Southwest Research Institute [5], [6]. These techniques are known to be efficient in locating rather large defects, both internally and externally, corresponding to 2-10% CSA (cross-sectional area) depending on the distance or the pipe covering. These methods utilize rings of transducers, either piezoelectric elements (PZTs) or electromagnetic acoustic transducers (EMATs), attached to the external surface of the pipe and can operate in either pulse-echo or pitch-catch configurations [7], [8] as shown in Figure 1.2. These rings have the capability to excite and sense various guided wave modes usually below 100 kHz, which are then interpreted according to transmission and reflection measurements.

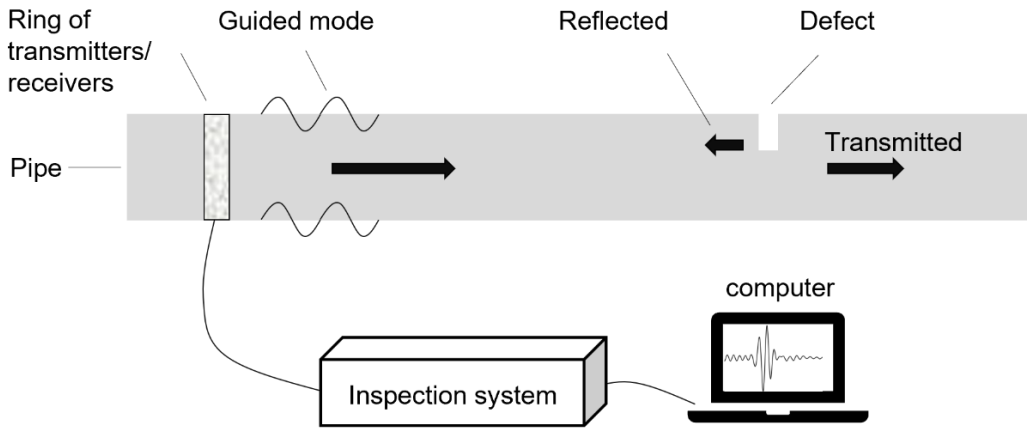

Figure 1.2: Schematic of the conventional guided ultrasonic wave (GUW) inspection method for pipelines.

Although widely used for rapid pipe screening, these methods are still not able to provide information regarding the amount of pipe thickness-loss or the actual profile of the damage. Recent studies have investigated the potential of guided ultrasonic wave imaging and tomography for pipelines [9]–[12]. In particular, Lamb waves have been utilized extensively due to their dispersive nature, which allows the correlation of the propagating wave speed with the thickness of the waveguide. Besides, these waves can be easily excited and sensed using low-profile sensors making this method attractive for fast and low-cost condition assessment.

The acoustic emission (AE) method has also found wide application for passively monitoring corrosion in pipes, tanks, and vessels [13], [14]. Corrosion related activities like pitting and peeling of the pipe's surface emit acoustic energy whose intensity is directly related to the severity of the damage [15]. In AE applications, a network of transducers is continuously recording the acoustic activity and attempt to quantify the remnant capacity of the interrogated structure using different features of the recorded data. A typical AE sensor layout is shown in Figure 1.3.

Recently, helical guided ultrasonic waves (HGUW) have emerged from the consideration of the Lamb wave propagation in cylindrical structures. These waves are thought to travel in the circumference of a pipe, enabling the consideration of multiple wave packets excited at a single source location that follow different trajectories before reaching a receiver. Ultimately, employing the HGUW offers the advantage of reducing the requirement in sensing units while the pipe

inspected area is increased significantly. While research to date has reported some promising results on the potential of employing HGUW, a comprehensive study has not yet been published.

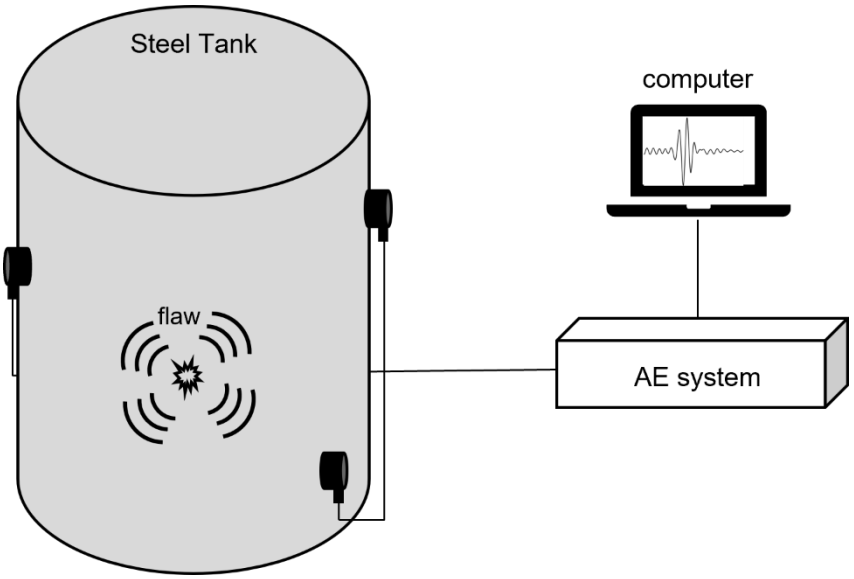

Figure 1.3: Schematic of AE monitoring for the evolution of different defects in pipes, tanks, and pressure vessels.

During this project, the potential of utilizing the HGUW was explored, for active and passive monitoring, as the main tool for the comprehensive evaluation of the structural integrity of pipelines. Both approaches require the permanent installation of low-profile sensors along the segment of the pipe that is under investigation. The active HGUW inspection scheme involved the development of algorithms that allow the performing of both qualitative and quantitative evaluations of the pipe condition. The former deals with the localization of corrosion-related defects in pipes through an algebraic reconstruction technique (ART) that utilizes the scattering of HGUW. This procedure can depict the locations that are severely damaged, and which require additional evaluation. A local tomographic algorithm is then utilized to reconstruct the remnant thickness at these locations using a minimization process between a 2-dimensional (2D) acoustic model and experimentally obtained phase velocity measurements. The sensitivity of the helical guided modes was investigated using detailed finite element simulations with a variety of different scatterers. An accelerated corrosion test was carried out for evaluating the effectiveness of the proposed methodology.

The passive monitoring scheme investigated the use of helical-type AE to study corrosion mechanisms in steel pipes. It was found that the energy and amplitude of the generated acoustic activity contain rich information regarding the initiation and progress of corrosion. Specifically, an adapted *b*-value analysis is proposed for extracting the corrosion growth while the cumulative amplitude and energy of the AE activity could indicate critical stages of the wall-thickness loss of the pipe. A numerical model was also developed to examine the energy distribution of a simulated AE source when happening at thinner portions of a waveguide, representing a wall-thinning due to corrosion.

2. Helical guided ultrasonic waves (HGUW)

In this chapter, a comprehensive guide for exploiting the helical guided waves towards pipeline condition assessment is presented. The HGUW are essentially plane strain guided waves considered to propagate circumferentially in large diameter cylindrical structures with the same properties of Lamb waves. Thus, throughout this report the pipes are represented by an equivalent plate with the same thickness. The excitation and sensing of the HGUW are achieved using circular piezoelectric sensors, that can be permanently attached to the pipe. These waves are utilized for in-transmission measurements of amplitude and phase velocity under the straight-ray assumption where no diffraction or refraction effects take place. Specifically, amplitude measurements are used as the damage indicator in an adopted algebraic reconstruction technique (ART) while the phase velocity is used in the tomographic algorithm which is based on a parametric 2D acoustic model. The developed methodology is valid for pipes with large diameter and is capable of detecting and sizing low-contrast defects. This chapter also discusses different topics including optimal sensor placement, operational frequencies as well as the attenuation of HGUW in fluid-filled pipes.

2.1. Theoretical framework

Studies have shown that in thin-walled curved structures with a radius-to-thickness ratio of more than 10/1, Lamb-type guided waves can propagate [16], [17]. Most of the oil and gas transmission pipelines have a minimum diameter of 6 inches and a minimum thickness of 0.4 inches (based on Schedule 40) which allow the consideration of Lamb wave propagation. This assumption enables the reduction of the guided wave propagation problem from the 3-dimensional (3D) cylinder to a 2-dimensional (2D) plate, with the same thickness. For visualization purposes, an arbitrary meridional line is selected representing the unwrapping axis of the pipe. This line is noted as the x-axis while the unwrapped circumference is noted as y'-axis.

Let us now consider a pair of circular piezoelectric transducers attached to the unwrapped two-dimensional (2D) surface of a cylinder with diameter D as shown in Figure 2.1(a). This type of transducer is capable of exciting circularly crested wavefronts of Lamb-type waves which is similar to an omnidirectional acoustic source. Due to the continuity of the cylinder surface,

multiple repetitions of the surface κ could be considered, which allows the transducers to virtually reappear vertically at $\pm\kappa\pi D$ from their original location with $\kappa = 0, -1, 1, -2, \infty$. Thus, a wavefront initiated at the transducer s_i containing an infinite number of rays will eventually be sensed by the transducer s_j and its virtual locations. If the wavelength of the excited wave is much smaller than the size of the defected area, diffraction can be neglected, and the rays can be represented by straight lines. In the physical geometry of a cylinder, these straight rays can be viewed as helically propagating waves as shown in Figure 2.1(b)**.** The number of unique rays connecting the same pair of actuator-receiver is termed helical order, h, thus, each ray (or path) connecting transducers s_i, s_j is noted as s_{i-j}^{h}, its length is indicated as l_{i-j}^{h} and h coordinate locations are considered $\left(x\,, y'_{s_j^h}\right)$. The total number of transducers is noted as n.

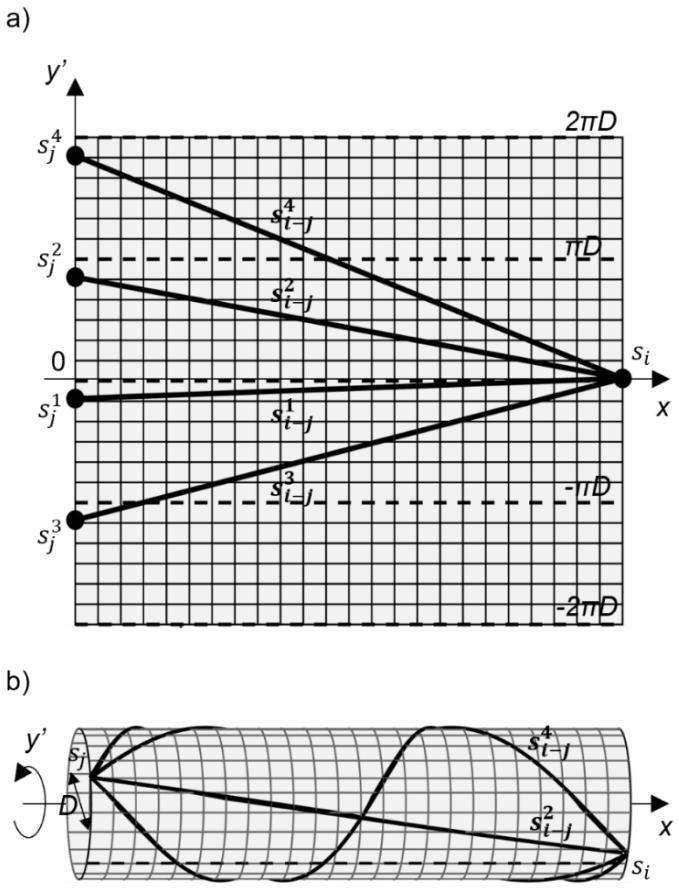

Figure 2.1: Demonstration of the first four helical orders s_{i-j}^{1-4} in, a) the unwrapped 2D and b) the physical 3D space.

The coordinates of the virtual receivers as well as the corresponding distances could be estimated using

$$y_j'^{(h)} = y_j'^{(1)} + n_h \pi D$$
$$n_h = 0,1,-1,2,-2,\dots,\infty \tag{2.1}$$

$$l_{i-j}^{h} = \sqrt{\left(x_j - x_i\right)^2 + \left(y_j'^{(h)} - y_i'\right)^2} \tag{2.2}$$

With the use of the Lamb waves dispersion curves, it is possible to temporally track any mode, by simply using the following relationships:

$$t_{i-j}^{h,S} = \frac{l_{i,j}^{h}}{C_g^S}$$
$$t_{i-j}^{h,A} = \frac{l_{i,j}^{h}}{C_g^A} \tag{2.3}$$

where, C_g^S is the group velocity of any of the symmetric modes, C_g^A is the group velocity of any of the anti-symmetric modes, i, j the pair of sensors and h the helical order.

2.1.1. Transmitter-receiver layout

To fully exploit the benefits of using the HGUW, the distinction between the consecutive helical modes in the time domain should not be tedious. This is achieved by properly choosing the relative position of the transducers which can minimize the ambiguity in mode identification. Considering now the propagation of two consecutive helical paths $h, h-1$ between sensors i, j attached on the unwrapped pipe circumference as demonstrated in Figure 2.2, the difference in arrival time of a non-dispersive Lamb mode can be calculated according to

$$\Delta t_{i,j}^{h-1,h} = \frac{l_{i,j}^{h}}{C_g} - \frac{l_{i,j}^{h-1}}{C_g} \tag{2.4}$$

Substituting Eq.(2.2) into Eq.(2.4) the difference in arrival time takes the following form:

$$\Delta t_{i,j}^{h-1,h} = \frac{\mathrm{L}}{C_g} \kappa_{\mathrm{i,j}}^{\mathrm{h,h-1}} \tag{2.5}$$

with $\kappa_{i,j}^{h,h-1}$ defined as the separation coefficient between consecutive helical paths according to [18]

$$\kappa_{i,j}^{h,h-1} = \left(\sqrt{1 + (\beta + n_h \pi\delta)^2}\right) - \sqrt{1 + (\beta + n_{h-1}\pi\delta)^2} \tag{2.6}$$

where $\beta = B/L$ and $\delta = D/L$. In the cases where $\theta = 0^{\circ}$ or $\theta = 90^{\circ}$, the separation coefficient is equal to zero, meaning that complete overlap of consecutive modes will occur making it impossible to distinguish the helical modes. This is the case when two sensors are placed either on the same meridional line or in two meridional lines with 90° relative angle and are termed ambiguous pairs. By examining the limits of Eq.(2.6), it is easily observed that the separation coefficient increases for larger values of diameter D while it decreases for shorter pipe lengths L.

Three different transmitter-receiver layouts, based on the cross-hole method for imaging, are presented in Figure 2.3 assuming 12 sensors. The first two are the typical parallel configurations with two arrays of sensors at each side. Their difference is that for the rotated-parallel layout the two arrays are rotated from-one another as to avoid having sensors on the same meridional line. The third layout is a rectangular type.

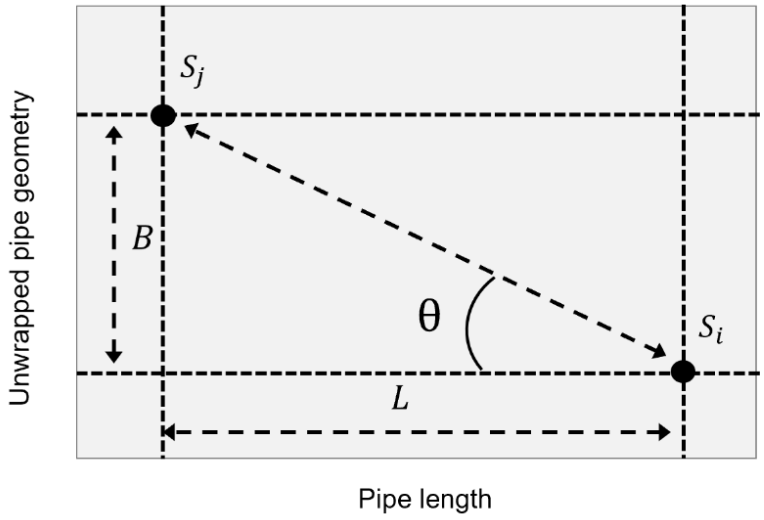

Figure 2.2: Relative position of sensors i, j on a pipe circumference. The longitudinal distance L, the circumferential distance B and the angle θ affect the separation coefficient $\kappa_{i,j}^{h,h-1}$.

The effectiveness of each layout can be measured in terms of the independent number of transmitter-receiver pairs N that have non-zero separation coefficient $\kappa_{i,j}^{h,h-1}$ according to

$$N = \frac{(n_s-1)\times n_s}{2} - \text{ambiguous pairs} \qquad (2.7)$$

where n_s the total number of sensing units and ambiguous pairs defined as the total number of transmitter-receiver pairs with κ = 0. For the parallel layout N = 30, for the rotated-parallel layout N = 36 and for the rectangular layout N = 48. The rectangular layout has the higher number of independent pairs, although the short distance between the sensors is causing the separation coefficient to be extremely small. In addition, when tomography is performed, the areas around the transmitters can introduce artifacts thus, the rectangular layout was rejected. From the two variations of parallel layouts, the rotated one was selected for its higher number of independent pairs as well as the ability to be reproduced along the pipe length. For rotated-parallel layout applied on pipes with 6-12 inches diameter an effective length of inspection was found to range from 0.5 – 1.5 meter. At each circumferential array, any number of sensors can be used although two or more are usually adequate.

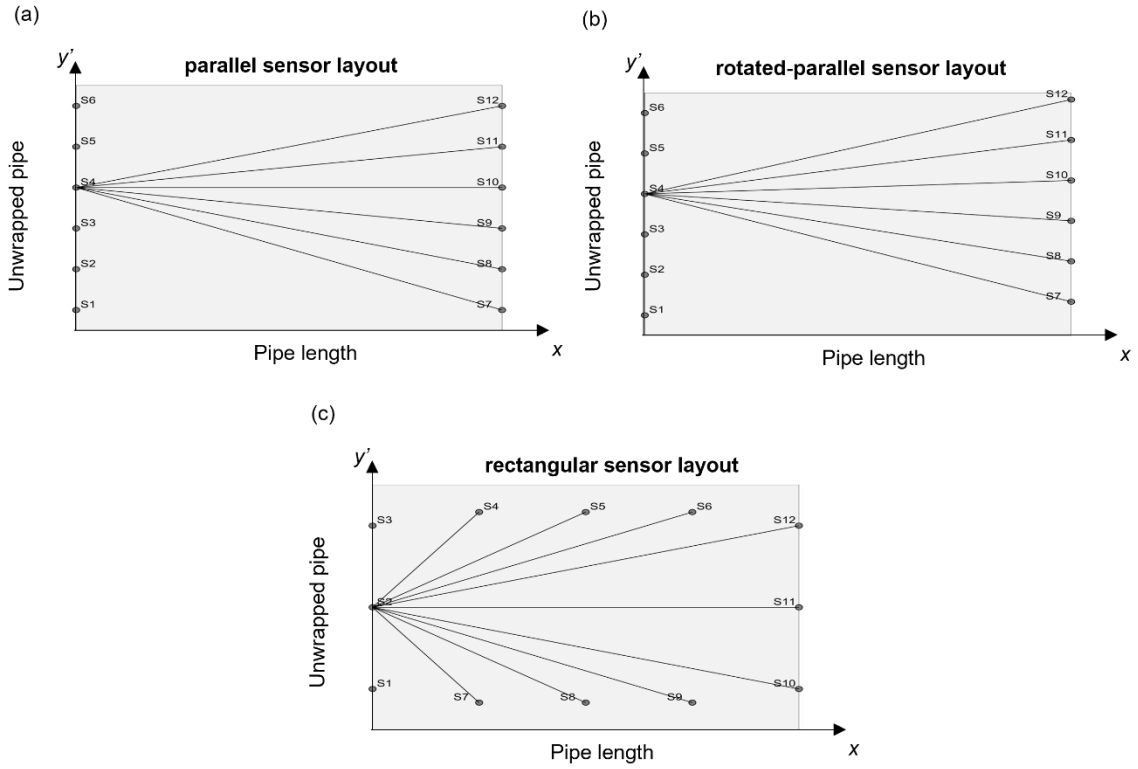

Figure 2.3: Three different transmitter-receiver layouts for a total of 12 sensors. a) the parallel, b) the rotated-parallel, and c) the rectangular layouts.

2.1.2. Number of sensing units and maximum helical order

In addition to the relative position of the sensing units, the total number of sensors that is used and the maximum helical order that is considered affect the overall effectiveness of the HGUW. The objective is to optimally position a minimum number of sensors in the pipe that will allow the helical waves to cover as much of the surface as possible. First, based on the desired area to be monitored the signal to noise ratio (SNR) must be large to allow for tracking and comparing the guided modes. In practice, attenuation can significantly impact the SNR, especially when the distance between the exciting and receiving sensors increase.

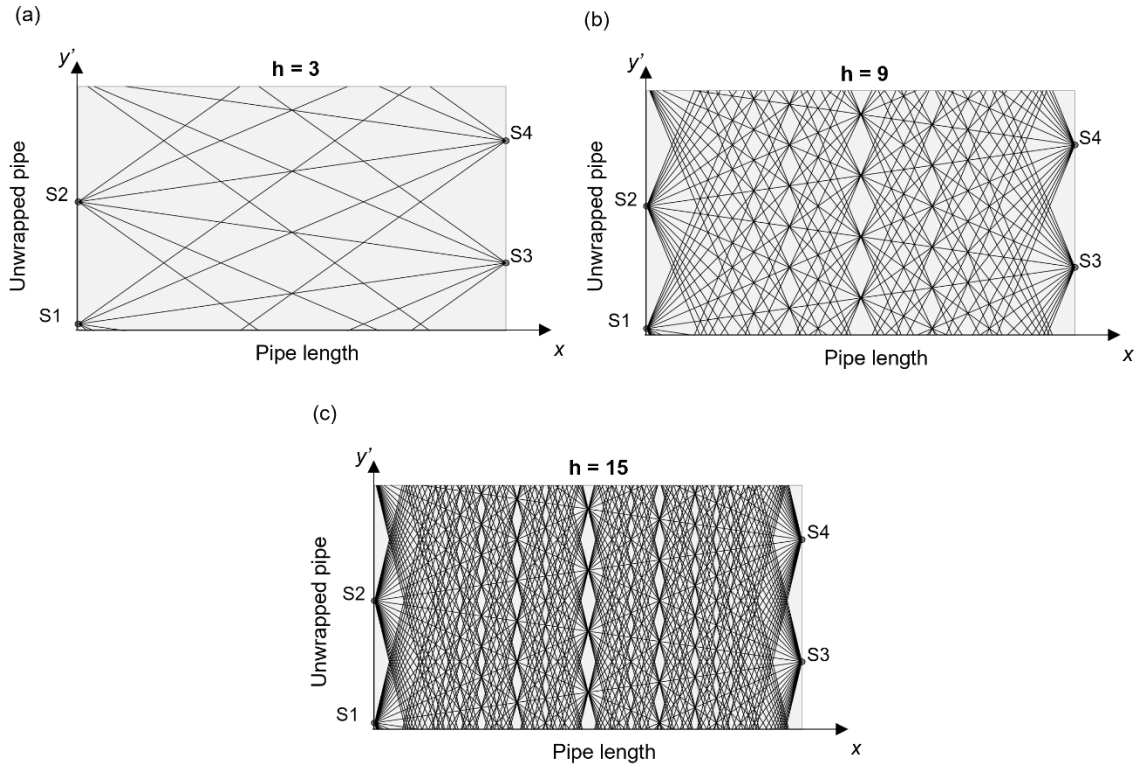

Figure 2.4: Schematic showing the ray density on the unwrapped pipe between four sensors considering different number of helical paths: a) h = 3, b) h = 9, and c) h = 15.

Upon deciding on the sensor layout and number, the maximum helical order must be determined. According to Figure 2.4, by simply plotting the superposition of helical paths between the sensors, it is easy to realize the effectiveness of increasing the helical order h. An analytical method to investigate the optimal helical order h, comprises of discretizing the 2D unwrapped pipe in square pixels and calculating the number of pixels being at least once crossed by a helical path. The remaining pixels are termed blind pixels. The size of the pixel should be at most equal to the smaller wavelength that is considered during testing. A typical curve obtained for the number of blind pixels against the helical orders is presented in Figure 2.5. The number of blind pixels exponentially decreases when the number of helical orders increases, eventually reaching a plateau where any further increase in the helical order does not significantly affect the blind pixels. The decision on the maximum number of helical orders should also consider experimental data in order to quantify the SNR. While theoretically 12 helical orders might be deemed enough, attenuation in experiments can severely limit this number.

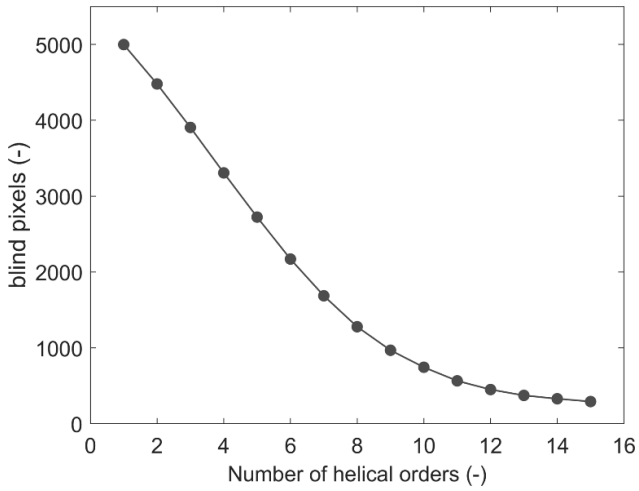

Figure 2.5: The typical relationship between the number of helical orders and the number of blind pixels. This example is based on a four-sensor configuration located 1 m apart on a 10 in. diameter pipe.

2.1.3. Operational frequency

When using the helical Lamb waves, it is imperative that the distinction between the different orders of the helical modes is non-trivial. Thus, the first cut-off frequency is often utilized as the upper frequency-thickness product. According to Figure 2.6(a) for a steel plate this fd corresponds to approximately 1.5 MHz-mm. Operating below this point aids to avoid exciting higher order modes which adds complexity in temporally separating different modes. In addition, higher frequencies are typically avoided because at these bandwidths the attenuation of Lamb modes tends to increase exponentially which affects the SNR in experimental settings.

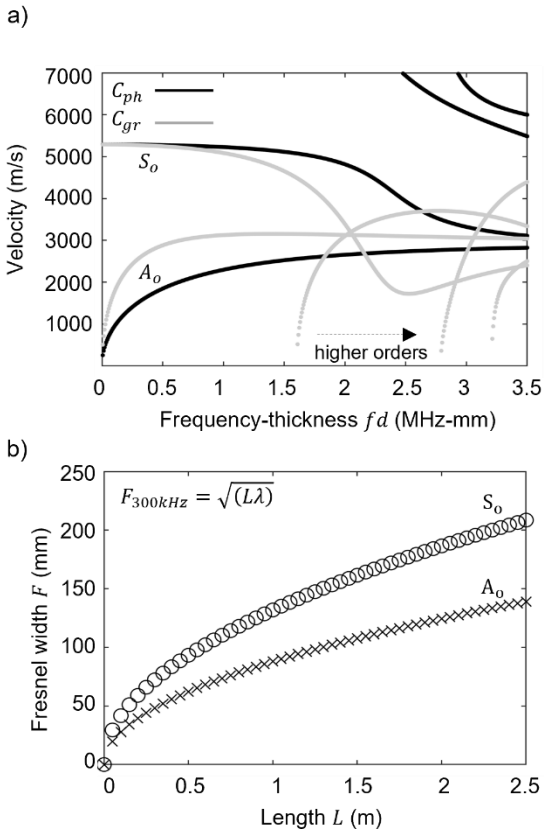

Figure 2.6: a) Lamb wave dispersion curves for a steel plate and b) the width of the Fresnel zone for modes S_0 and A_0 at 300 kHz for range of transmitter-receiver lengths up to 2.5 m

For Lamb wave imaging, the operating frequencies define the resolution of the reconstruction. The behavior of an incident Lamb mode on a defect depends on the defect depth, shape, as well as the wavelength of the mode. In general, if the wavelength of the incident mode is very large compared to the extent of the defect, the effect on the propagating mode will be minimal. On the other hand, if the defect and the excited mode have wavelengths of a similar order, the interaction of the two will result in a partial reflection and partial transmission. The lower limit of the frequency range is decided based on the initial assumption made that diffraction effects will be negligible. For this statement to be valid, the ray theory must be respected, thus the width of first Fresnel zone $\sqrt{(L\lambda)}$ has to be smaller than the characteristic size of the targeted damage [19] where, L is the distance between transmitter and receiver and λ the wavelength of the incident wave. For example, let's consider a defect with dimensions (~200 mm×200 mm). By setting the lower frequency at fd = 1 MHz-mm ($\lambda_{S_o} \sim 17\text{mm}$, $\lambda_{A_o} \sim 7\text{mm}$) and considering that the length of

the helical rays could extend to infinity, a plot of the Fresnel zone could be constructed according to Figure 2.6(b). To maintain the width of the Fresnel zone for both fundamental modes smaller than the corrosion extent, the maximum helical order that can be considered should have a propagation distance smaller than 2.5 m.

2.1.4. Fluid bordering

In pre-stressed waveguides that cause the propagation energy to dissipate, the group velocity C_g no longer represents the velocity of the energy propagation. Instead, the term energy velocity C_e is used. Studies have investigated the effect of the fluid pressure on the energy velocity of the helical Lamb waves [20]. This is not only dependent on the pressure but is also dependent on the angle of propagation of the HGUW. For example, Figure 2.7 demonstrates the variation of the energy velocity C_e of the first couple orders of helical Lamb modes for constant internal pressure when the transmitter-receiver pair is located on the same meridional line 0˚ and when the transmitter-receiver pair is located on the same circumferential line 90˚. Below the first cut-off frequencies, the fundamental symmetric mode is primarily affected by the pressure compared to the fundamental anti-symmetric mode. Overall, it is reported that a linear dependance of internal pressure and the variation of energy velocity ΔC_e exists that is more significant when the propagation direction is along the pipe's circumference. Practically, these curves provide correction coefficients for the helical wave velocity that should be applied to account for the internal pressure of the pipe.

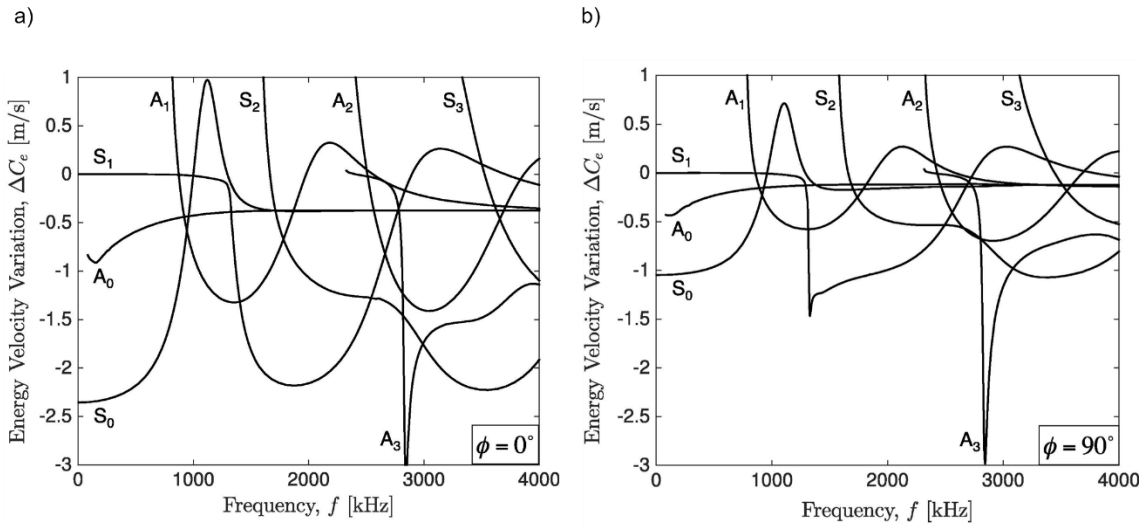

Figure 2.7: Mode and frequency dependence of the change in energy velocity for different propagation directions (a) circumferential and (b) longitudinal, in a stressed steel plate bordered by water on one side. (Figure from Dubuc et. al. [20]).

2.2. The algebraic reconstruction technique (ART) adopted for HGUW

By discretizing the surface of the pipe in square cells (or pixels) and under the assumption of small refraction effects, the algebraic reconstruction technique (ART) traces the helical rays between pairs of transmitting and receiving sensors. The pixels that are being intersected by a given helical ray are assigned a certain weight according to the length of the ray that crosses them. The overall problem can be categorized as a linear algebra problem [21] that can be written as

$$\boldsymbol{A}_{(m\times n)}\boldsymbol{x}_{(n\times 1)} = \boldsymbol{d}_{(m\times 1)} \tag{2.8}$$

where $\boldsymbol{A}_{(m\times n)}$ is the matrix storing the weight of the helical ray on the pixel for a given pair of sensors s_i, s_j. This can be evaluated by calculating the distance that each helical path travels along each pixel normalized by the diagonal of each pixel, according to Figure 2.8. Each row of the matrix $\boldsymbol{A}_{(m\times n)}$ represents a linear equation with n number of unknown coefficients each one representing a pixel of the image.

$$A_{(mxn)} = \begin{bmatrix} w_{1,2}^{1,1} & w_{12}^{1,2} & w_{1,2}^{1,3} & \dots & w_{1,2}^{1,n} \\ w_{1,2}^{2,1} & w_{12}^{2,2} & w_{1,2}^{2,3} & \dots & w_{1,2}^{2,n} \\ w_{1,2}^{3,1} & w_{12}^{3,2} & w_{1,2}^{3,3} & \dots & w_{1,2}^{3,n} \\ \vdots & \vdots & \vdots & \ddots & \\ w_{i,j}^{m,1} & w_{i,j}^{m,2} & w_{i,j}^{m,3} & \dots & w_{i,j}^{m,n} \end{bmatrix} \tag{2.9}$$

The vector $\boldsymbol{d}_{(m\times 1)}$ stores the damage coefficients. Those coefficients represent a measure of the similarity of a waveform from a pair of sensors before and after a damage is introduced in the pipe. This method is known as baseline subtraction method [22] and can track changes for a large period of the structure's life. In this work a damage coefficient, $\boldsymbol{d}_{i,j}^{m}$ was calculated using

$$\boldsymbol{d}_{i,j}^{m} = \int_{t_{i,j}^{h,A_0}}^{t_{i,j}^{h,A_0}+\delta\tau} \frac{\left(R_{i,j}^{h}(t) - D_{i,j}^{h}(t)\right)^2}{\left(R_{i,j}^{h}(t)\right)^2} dt \tag{2.10}$$

where $R_{i,j}^{h}(t)$ and $D_{i,j}^{h}(t)$ are the time waveforms from pristine and damaged states of the pipe, and $\delta\tau$ is the duration of the excitation pulse. The vector $\boldsymbol{x}_{(n\times 1)}$ contains the unknown image values for which the system of linear equations will be solved.

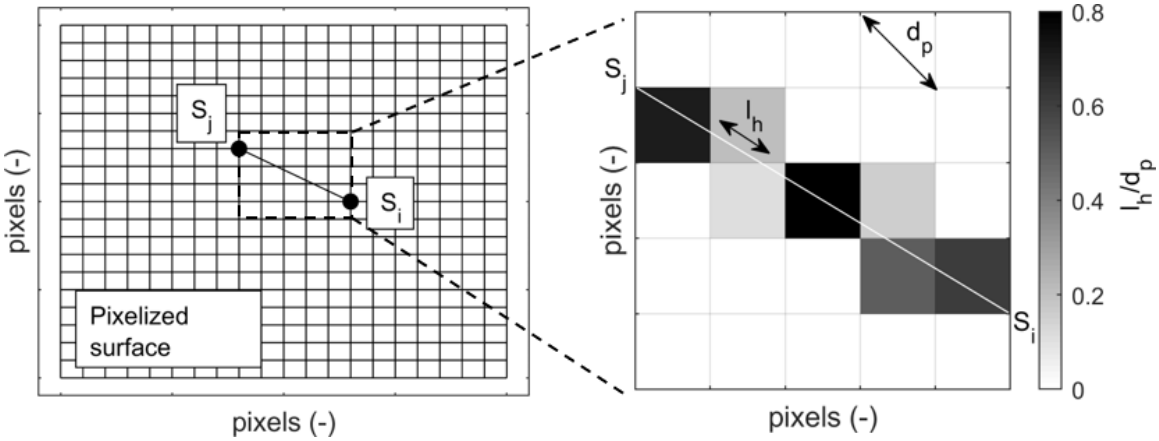

Figure 2.8: Procedure for calculating matrix $A_{(m\times n)}$

In general, Eq.(2.8) is ill-posed, meaning that the number of independent equations m is smaller than the number of unknown coefficients n thus producing an underdetermined system of equations. To solve Eq.(2.8), an iterative scheme based on the Kaczmarz's method [21], [23] was formulated as follows:

$$\vec{\boldsymbol{x}}^{(i)} = \vec{\boldsymbol{x}}^{(i-1)} + \frac{\boldsymbol{d}_{(\mathrm{i})} + \vec{\boldsymbol{x}}^{(\mathrm{i}-1)} \cdot \vec{\boldsymbol{A}}_{\mathrm{i}}}{\vec{\boldsymbol{A}}_{\boldsymbol{i}} \cdot \vec{\boldsymbol{A}}_{\boldsymbol{i}}} \vec{\boldsymbol{A}}_{\boldsymbol{i}} \tag{2.11}$$

where operation $(\cdot)$ is a dot product. This method assumes that each row of the matrix A represents a hyperplane and seeks solutions at their intersection point. The algorithm starts with an initial guess $\vec{\boldsymbol{x}}^{(0)}$ which projects sequentially on all the hyperplanes until converging to a solution. For a given matrix $A_{(m\times n)}$ with $m < n$ the algorithm converges to a solution as long as $\left|\vec{\boldsymbol{x}}^{(0)} - \vec{\boldsymbol{x}}^{(i)}\right|$ is minimized.

2.2.1. Test 1 - Simulated damage using magnets

An overview of the experimental setup is presented in Figure 2.9. Tests were conducted on a 1.52 m (5 ft) long carbon steel pipe (ASTM A153 standard). The diameter and wall thickness were 304.8 mm (12 in.) and 3.42 mm (0.1345 in.) respectively. A total of six piezoelectric (PZT) disks of 6.35 mm (0.25 in.) diameter were permanently attached on the surface of the pipe using epoxy adhesive as shown in Figure 2.9. Separation of consecutive helical A_0 wave packets is crucial to minimize ambiguity in the imaging [18] thus, the locations of the sensors were chosen to fulfill that requirement as shown in Figure 2.10. To simulate corrosion damage, a pair of high-pull, rare-earth magnets with 12.70 mm (1/2 in.) thickness and 19.05 mm (3/4 in.) diameter were attached at the same location in both inner and outer surface of the pipe. The magnets act like scatters once they interact with the propagating guided wave modes and have been used in other studies to simulate local damage [24], [25]. Two different locations, D1 and D2, of this double side magnet configuration were encountered each time as shown in Figure 2.10 to simulate potential defects. Signals from the sensors were amplified using OLYMPUS 5560B with a gain of 40 dB and recorded through a LabVIEW software. Waveforms were generated using a 20 MHz bandwidth, 14 Bit PXI 5412 and recorded with a 60 MHz, 8 Channel, 12 Bit PXI 5105. A 5.5 cycle

toneburst with a center frequency in the range of 300 400 kHz was used as excitation. Excitation toneburst was amplified using a high-voltage amplifier. The excitation frequency was between 300-400 kHz which is below the first cut-off frequencies in order to excite only the fundamental symmetric and anti-symmetric modes.

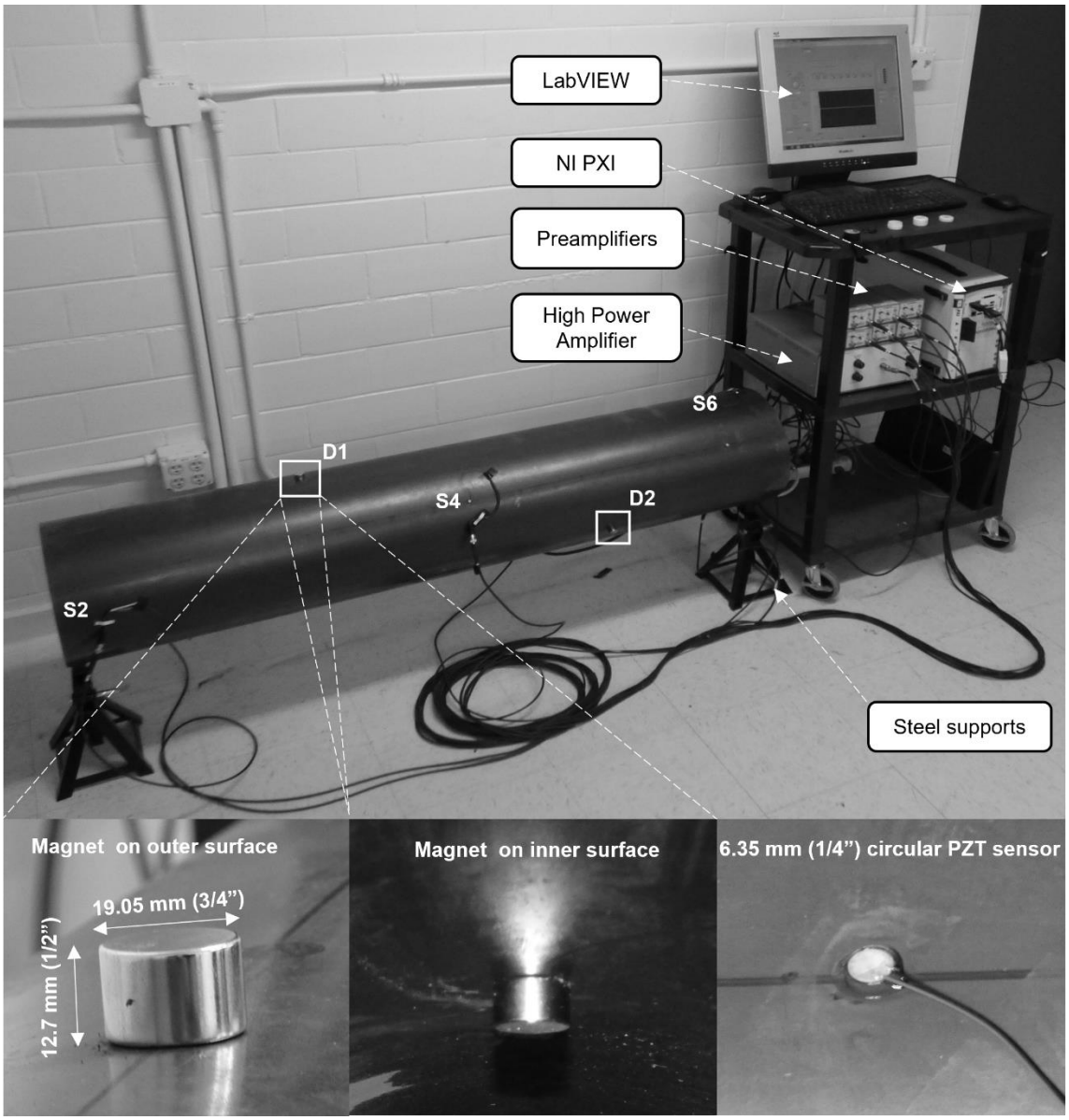

Figure 2.9: An overview of the experimental setup used for test 1. A 5-ft long pipe was instrumented with 6 PZT sensors and damage was simulated by attaching pairs of magnets on its surface. The pipe was supported with tripods at the two ends.

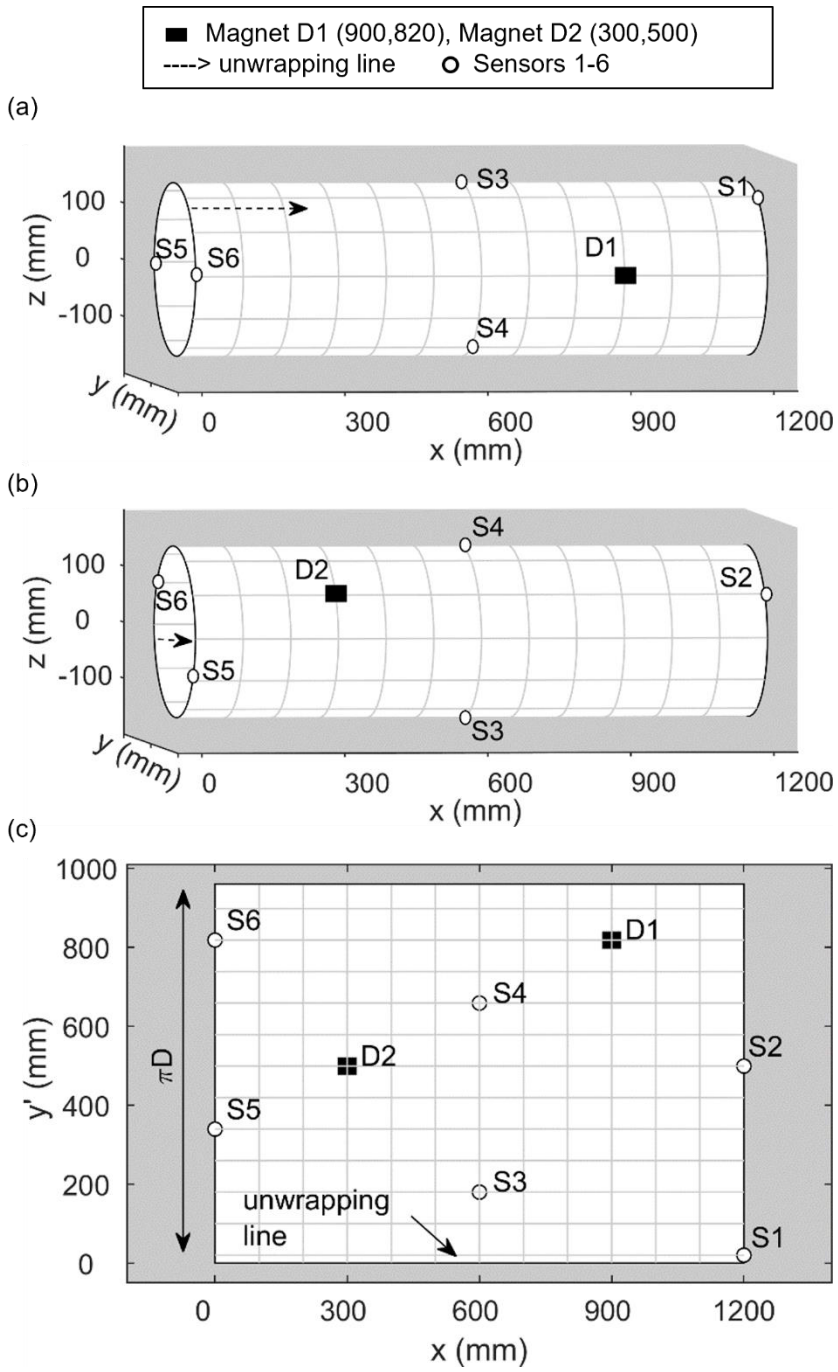

Figure 2.10: 3D representations of sensor and magnet locations: (a) defect D1, (b) defect D2, and (c) 2D unwrapped representation of the pipe. Note: at each location D1 and D2 a pair of magnets was placed in the inner and outer surface of the pipe and no couplant has been used.

2.2.2. Operational frequency

Figure 2.11 presents the dispersion curves for the specific steel pipe that was used in the experimental setup. Below the first cut-off frequency, the fundamental symmetric S_0 and anti-symmetric A_0 modes exist. Excitation and sensing of these Lamb modes had been achieved using conventional circular piezoelectric (PZT) transducers, which are known to have a dominant sensitivity to the out-of-plane vibrations and are rather insensitive to the in-plane vibrations [26], [27]. Thus, any effect from the shear horizontal mode (SH_0) was omitted.

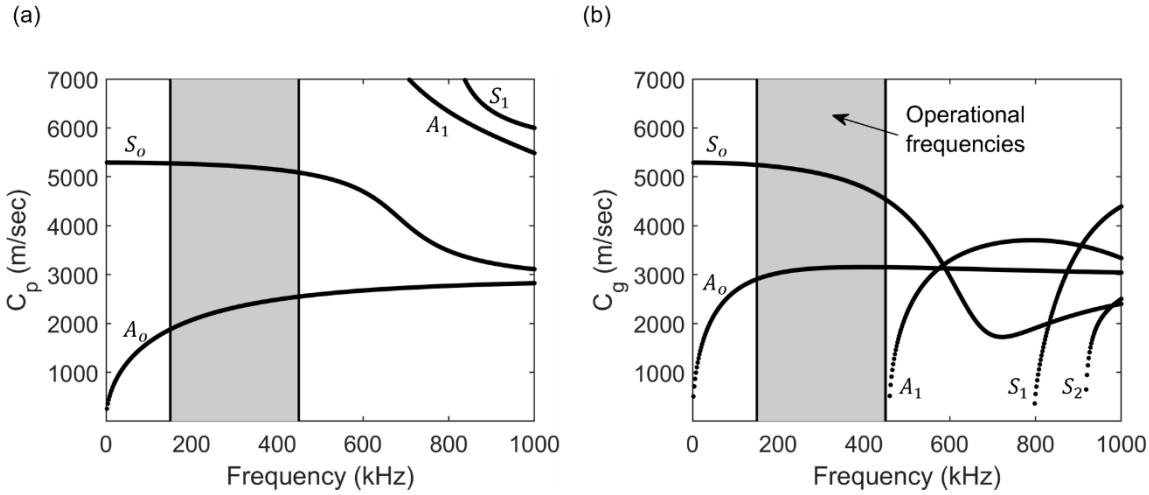

Figure 2.11: Solutions to the Lamb problem for 3.42 mm thick steel plate: (a) phase velocity C_p (b) group velocity C_g. Shaded region indicates the chosen operational frequencies.

The shaded region in Figure 2.11 indicates the excitation frequency range used for this test. The lower limit of this bandwidth is defined by the point where the group velocity (C_g) of the A_0 mode becomes constant. The upper limit is primarily defined to avoid the complexity of exciting higher order modes. In this specific bandwidth, the asymmetric A_0 mode has some relative merits compared to the symmetric S_0 under the assumption that there is no fluid inside the pipe. One of the most important attribute is that its group velocity (C_g) is basically constant but its phase velocity still remains dispersive enough to make it sensitive to thickness variations [28]. Physically this property, implies that A_0 mode will maintain its speed for any helical path in the problem and any potential interaction with damage will affect only the received shape of the A_0 mode. Another important feature of working is the described frequency range is that the excitability and sensing

of A_0 mode is significantly higher than S_0 while its group velocity is significantly smaller than S_0 making the distinction between the two easier.

This experiment leveraged the fact that the expected transmitted mode from a circumferential defect will be significantly different in terms of amplitude and phase compared to the one traveling the same path but propagates through the pristine material. The frequency range specified in Figure 2.11 corresponds to wavelengths in the range of 10 mm (0.4 in.) and thus the simulated defects for this work have been chosen to be no larger than 30 mm (1.2 in.).

2.2.3. Maximum helical order

The accuracy of the algebraic reconstruction technique depends heavily on the density of the helical rays since ART is based on solving a set of algebraic equations. The natural extension of the potential inspection area is defined by the pair of sensors lying farther apart across the length of the pipe that being sensors S1, S2 and S5, S6. In order to increase the ray density in that region, a certain number of helical orders has to be considered. The tomography grid used for the ART algorithm is based on pixels with size 10 mm × 10 mm (0.39 in. × 0.39 in.) totaling 11520 pixels. The size of the pixels is small enough to cover the smallest defect in both experiments and numerical simulations.

Blind pixels are termed the pixels that are not intersected by any helical ray. Figure 2.12 shows the estimated number of blind pixels against the helical orders. The curve illustrates that the rate at which the blind pixels are reduced is large until roughly the seventh order. The amount of those blind pixels tends to converge to a certain number after the consideration of nine or more helical orders. Based on this observation, the number of helical orders was chosen to be nine which results in a blind pixel value of 6.94% of the total pixels.

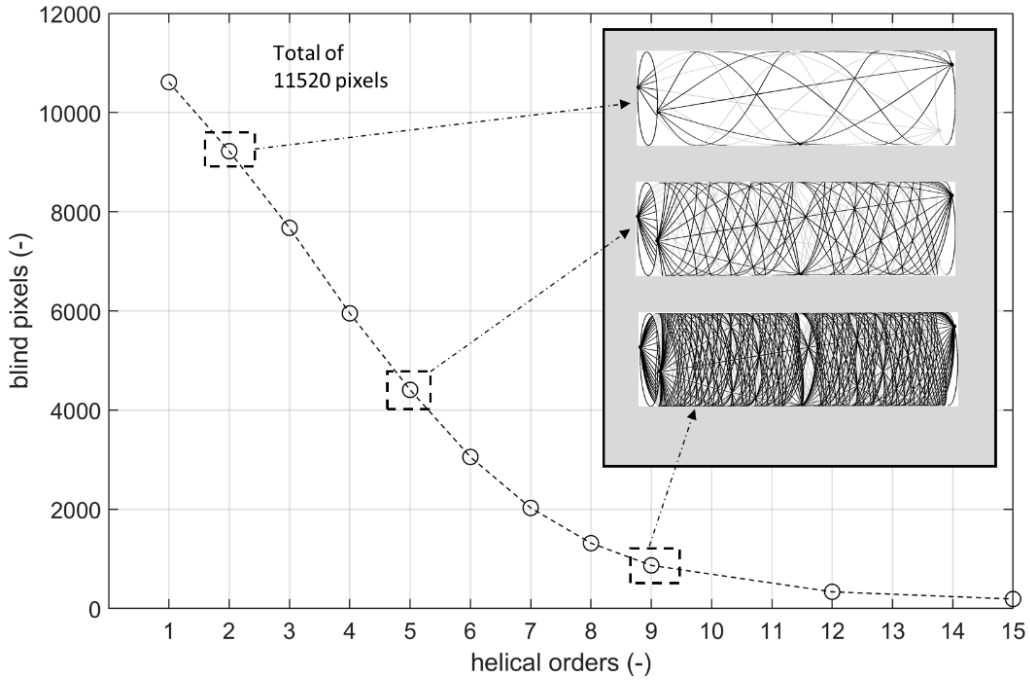

Figure 2.12: Comparison of the total number of blind pixels with the helical order. A 3D schematic of the 2-nd, 5-th and 9-th helical order ray density on the top corner

The selection of the highest helical order was also based on a number of other parameters. First, higher orders will generally require a much larger time window since the helical paths are becoming larger. By doing so, uncertainty is introduced in the overall problem by the attenuation of Lamb modes, increased overlap of S_0 and A_0 modes, as well as noise from the experimental setup. Furthermore, the computational time will be higher since a larger number of equations have to be solved simultaneously. Figure 2.13 represents a schematic of the nine helical orders ray density in the 3D and 2D representation, respectively. Table 2.1 presents the length of each helical path from sensor S1 to respective sensors S2 - S6. Based on these values the arrival time of each mode was estimated by using Eq.(2.3) The initial number of equations from the consideration of nine helical orders and 6 sensors is $m = 5 \times 9 \times 6 = 270$. Two corrections should be made to the number of equations. First, between sensors that are placed on the same y'- coordinate or x - coordinate, for example, S1 and S2, helical paths become ambiguous. This means that all the helical paths connecting those two sensors follow the same geometrical path, thus are not being used in this study. The ambiguity of helical paths is also demonstrated in Figure 2.13 where no helical path exists to connect the pairs S1-S2, S3-S4, and S5-S6. Second, due to reciprocity, a

helical path is the same when traveling from S1 to S5 and vice versa. For every helical path that experience reciprocity, the damage coefficient $d_{i,j}^{m}$ is averaged. Thus, the total number of m unique equations results to be 98 yielding a matrix $A_{98\times11520}$.

Table 2.1: The lengths of nine helical paths from sensor S1 to sensors S3-S6

	Sensors			
	3	4	5	6
L^1 (mm)	620.86	679.62	1241.72	1210.57
L^2(mm)	998.37	876.08	1359.23	1441.09
L^3(mm)	1268.08	1410.70	1752.16	1639.52
L^4(mm)	1855.22	1704.99	1996.74	2126.47
L^5(mm)	2159.73	2313.46	2536.16	2396.75
L^6(mm)	2778.63	2623.03	2821.40	2966.61
L^7(mm)	3091.06	3247.76	3409.98	3261.08
L^8(mm)	3719.35	3561.94	3710.45	3861.81
L^9(mm)	4034.69	4192.57	4319.45	4166.38

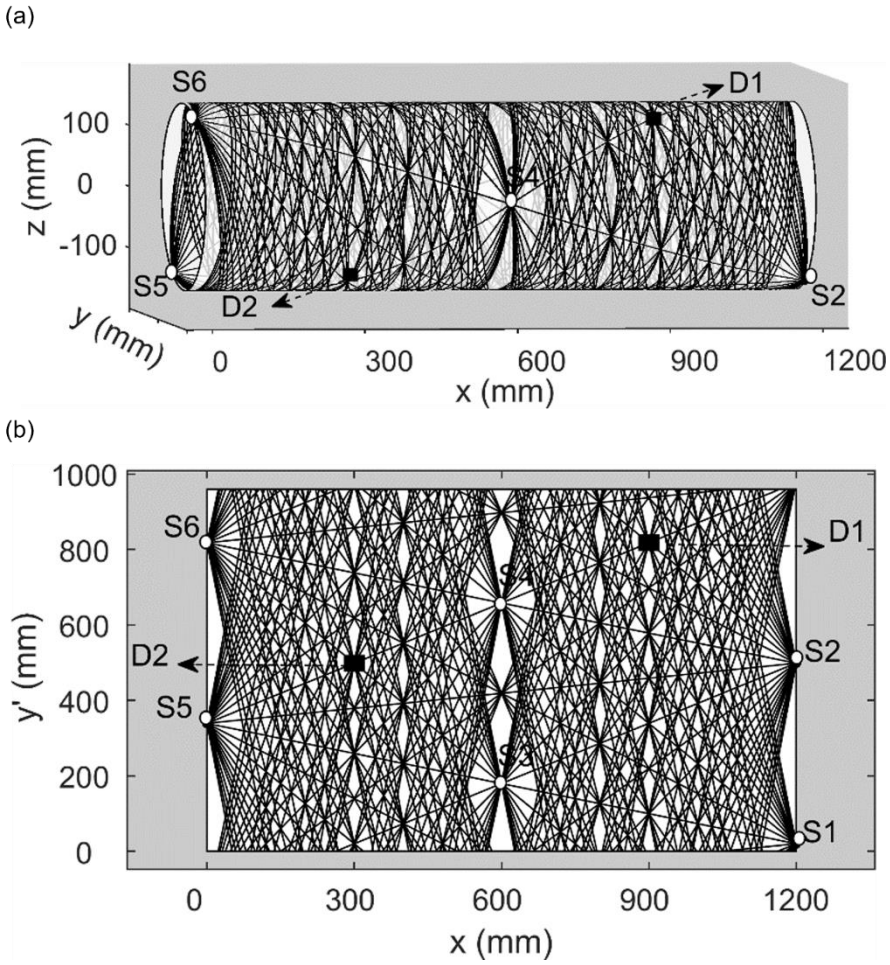

Figure 2.13: Demonstration of the 9 helical orders ray density and exact locations of simulated defect D1, D2: (a) 3D view, (b) 2D unwrapped view.

2.2.4. Damage localization using the ART

Overlapping of high orders of helical S_0 and A_0 modes means that certain S_0 wave packets can occur at the same time instance as the arrival of A_0 packets. Since the proposed algorithm utilizes only the A_0 mode, the quality of the final reconstructed image can be severely compromised when overlapping is present. For example, the arrival time of S_0 mode $t = 0.2$ms of the second helical path $L_{1,3}^2 = 1$ m for $C_g^{S_0} = 4970$ m/s at 340 kHz, it is really close to the arrival time of A_0 mode $t = 0.2$ ms of the first helical path $L_{1,3}^1 = 0.62$ mm for a given $C_g^{S_0} = 3140$ m/s. Therefore, the operational frequency which basically changes the group velocity of the S_0 mode should be chosen in order to maximize the separation of the two fundamental modes.

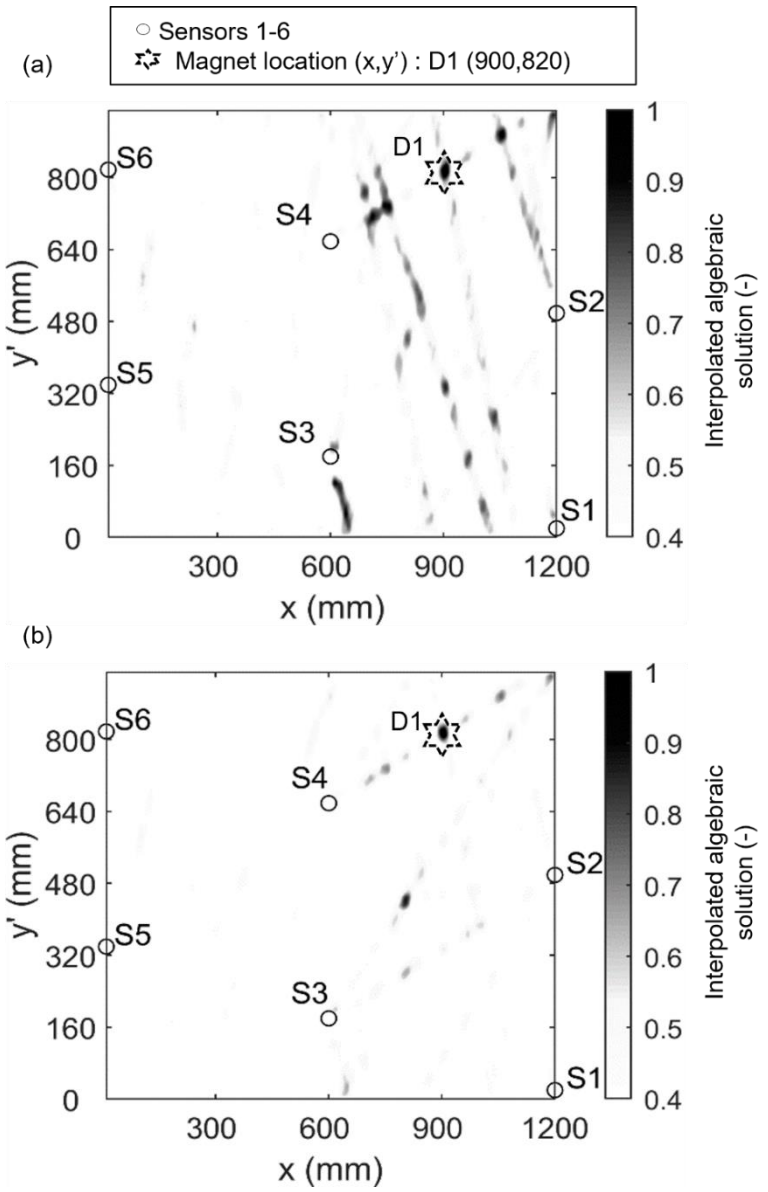

Figure 2.14: Reconstructed images from experimental setup when magnet pair is at location D1 using excitation frequency: (a) 340 kHz, (b) 400 kHz in the 2D unwrapped representation of the pipe.

Figure 2.14 shows the reconstructed image using two operational frequencies 340 kHz and 400 kHz in the 2D unwrapped representation. A total of eight S0 and A0 modes are calculated to arrive at the same time instance for the case of 340 kHz in comparison with no mode overlapping in the case of 400 kHz. The direct effect of this mode overlapping can be observed through a comparison of the two reconstructed images. In the case of 340 kHz artifacts are being introduced and the overall quality of the image is relatively low. For the 400 kHz operating frequency the

defect D1 is clearly localized with minimum artifacts. Thus, for the all cases, 400 kHz operational frequency was chosen.

Figure 2.15 shows the reconstructed image for the two different damage locations D1, D2 of the pair of magnets respectively. These images were obtained using an operational frequency of 400 kHz and nine helical orders. The proposed ART algorithm shows great potential at localizing the scattering effect of the magnets. Artifacts in the image can be seen primarily in diagonal lines along the damage location or parallel to it. This is due to the interference of helical paths having significantly lower damage coefficient and the dominant ones. The largest artifacts in the two images have magnitudes smaller than the actual damage by 12% for the case of the magnets at location D1 and 30% at D2. These artifacts are limited to the area around the magnet locations and have extension several pixels fewer than the true indications, proving that the proposed algorithm has a relatively large accuracy.

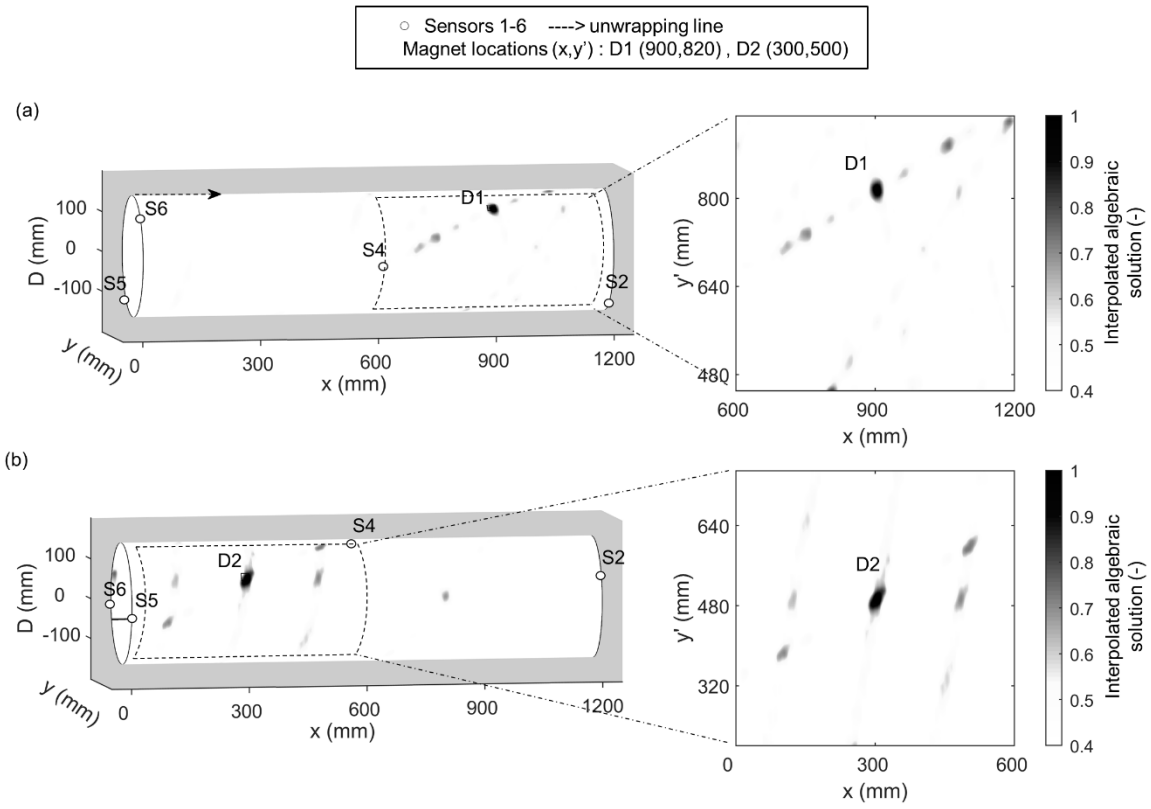

Figure 2.15: Reconstructed images from experiments: (a) magnet location at D1, (b) magnet location at D2.

2.2.5. Test 2 - Machined damages

Experiments were performed on a 60-cm section of a 1.52 m (5 ft) long carbon steel pipe, with diameter and wall thickness of 30.48 cm (12 in.) and 3.416 mm (0.1345 in.) respectively. The pipe was instrumented with 12 PZT disks in two groups of circular arrays. For each array the sensors had an angle difference of 60 degrees and between the two arrays the angle difference was 30 degrees. The locations of the PZT sensors were chosen in such a way to minimize ambiguity in the tomography occurring from the overlapping of consecutive helical paths. Damage was introduced in the pipe by machining its surface at multiple locations and then the remaining thickness was measured using a conventional ultrasonic probe. The first simulated damage (D1) had a size of 50 mm × 30 mm and the second damage (D2) had a size of 30 mm × 30 mm. The reduction in thickness for both the damages was estimated to be near 30%. Attempt for pipe imaging has been made first for damage D1 and then for both damages D1-D2. Signals from the sensors were amplified using OLYMPUS 5560B with a gain of 40 dB and recorded through a LabVIEW software. Waveforms were generated using a 20 MHz bandwidth, 14-Bit PXI 5412 and recorded with a 60 MHz, 8 Channel, 12-Bit PXI-5105. A 5.5 cycle toneburst with a center frequency in the range of 250-425 kHz was used as excitation. Excitation toneburst was amplified using a high-voltage amplifier. The collected time-domain waveforms had a length of 2 ms to allow for a comparative study on the influence of using different helical orders when applying the ART. Specifically, 3,5 and 8 helical orders have been considered for the damage localization.

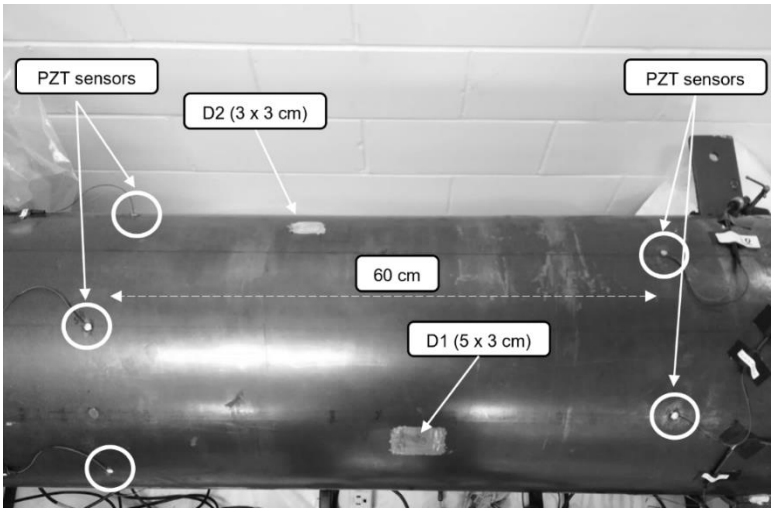

Figure 2.16: An overview of the second experiment. A total of 12 PZT sensors located 60 cm apart, and two different spots were machined to remove approximately 30% of the wall thickness.

2.2.6. Damage localization using different number of helical orders

Figure 2.17 represents a schematic of the first five helical paths connecting sensors S3 and S9 as well as a typical time domain signal. The interaction of helical paths 1, 4, 5 with the damage result in alterations of the received mode shape of the A_0 mode, like amplitude variations and slight phase shift. These differences can be observed in the differential signal where those three modes appear to have the largest deviations as opposed to the rest on the received modes. In contrast, the symmetric mode S_0 appear to be less sensitive to the damage being suppressed by the baseline subtraction.

Figure 2.18 shows the reconstructed images for damage D1 with the consideration of three, five, and eight helical orders. The accuracy of localization is improved with the use of more helical orders, while the number of artifacts is considerably smaller when using fewer helical orders. This is due to the higher density of the helical rays but at the same time attenuation of higher orders of helical modes and partial temporal overlapping between the S_0 and A_0 can severely compromise the quality of the image. Thus, for the rest of the reconstructions, five orders were assumed adequate. False positives can also be seen near the sensor locations. Physically, a sensor location consists of the intersection of all the helical paths initiating at that point thus a possible solution to the linear algebra problem. In general, these artifacts are relatively small compared to the actual damage location and can be filtered out from the final image.

To further exploit the potential of the proposed imaging algorithm, an effort has been made to localize two damages simultaneously. Figure 2.19 represents the tomographic image for damages D1 and D2. The accuracy of the ART algorithm remains high, giving clear indications on the locations of the damages.

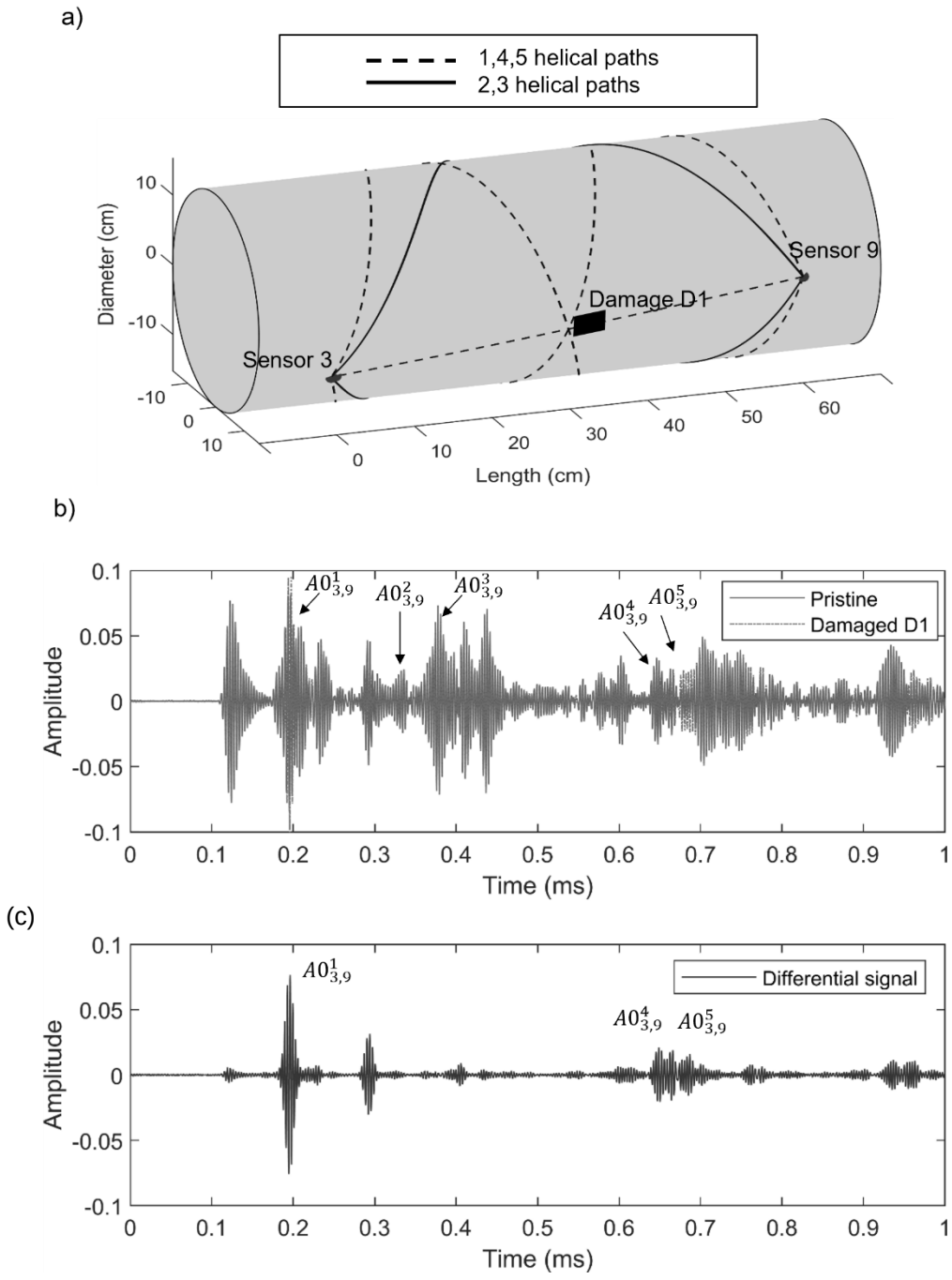

Figure 2.17: Transmitting and receiving sensors 3 and 9. a) Representation of the first five helical paths, b) typical signals obtained from pristine and damaged stages and c) the baseline subtraction

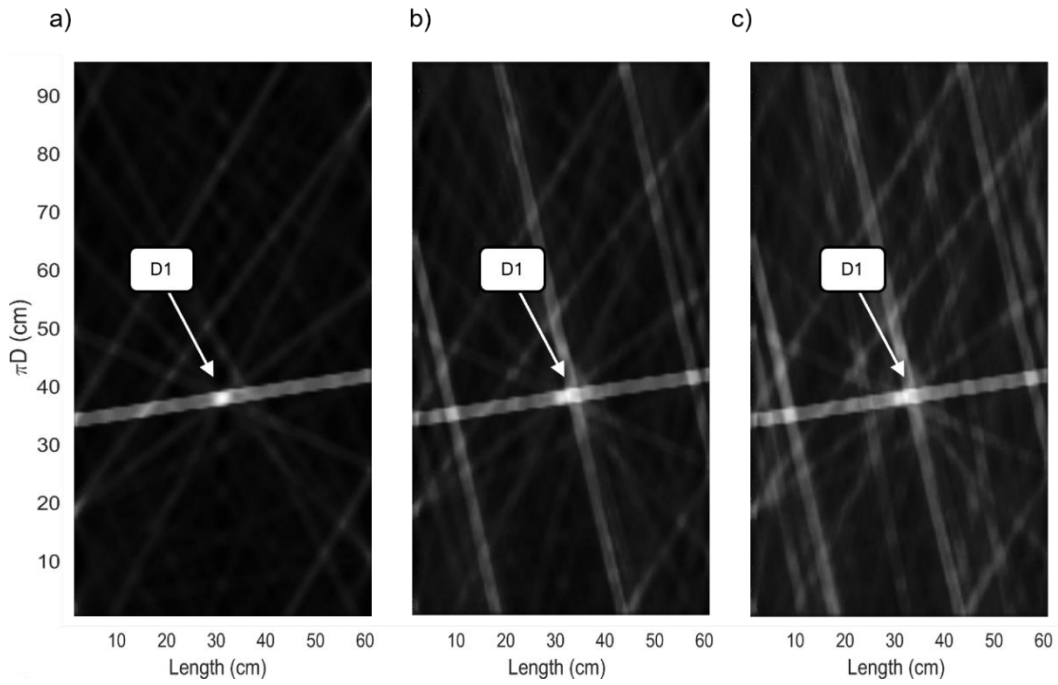

Figure 2.18: Reconstructed images for damage D1 with the use of a) three b) five and c) eight helical orders

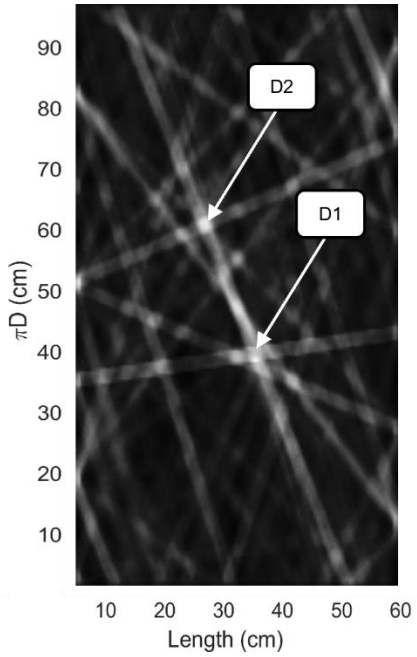

Figure 2.19: Reconstructed image for damages D1&D2 using five helical orders

2.3. 2D acoustic modeling

In Lamb wave tomography, to properly characterize the shape of the corrosion in the pipe it is critical to have an accurate forward model based on which the experimental readings will be inverted to produce a thickness map. Such forward modeling could be achieved by iteratively solving a 3D guided wave problem using a finite element method (FEM) until a desired convergence to the experimental data occurs. Considering the size of the pipe, and the additional mesh discretization required to model high frequency guided waves, such an approach is considered time consuming. An alternative approach is to reduce the 3D problem to an approximate 2D acoustic wave problem, under the assumption that the ray theory is valid, and that the corrosion is anticipated to have a slowly varying thickness profile. In this way, the thickness can be modeled as a single value of velocity, which is decided according to the dispersion relationships (fd product). Thus, in a discretized 2D domain where each node is assigned a velocity value, the travel time of Lamb waves is defined by the those nodes lying on their propagation path [10] . A theoretical model could be based on the frequency domain Helmholtz equation,

$$(\nabla^2 + k^2)p(x, y', \omega) = s(x, y', \omega) \tag{2.12}$$

where, $k(x, y', \omega) = \omega/c(x, y')$ denotes the wavenumber with velocity c and, angular frequency ω, $p(x, y', \omega)$ is a scalar displacement wavefield and $s(x, y', \omega)$ the source. Assuming a solution of the form $p = A \times exp\big(-i\omega\tau(x, y')\big)$ with $\tau(x, y')$ describing the time delay and A a complex constant, Eq.(2.12) can be simplified to its high-frequency approximation, known as the eikonal equation,

$$\left(\frac{\partial\tau}{\partial x}\right)^2 + \left(\frac{\partial\tau}{\partial y'}\right)^2 = \frac{1}{c^2(x, y')} \tag{2.13}$$

where $c(x, y')$ is the wave velocity. Solution to Eq.(2.13) could be thought as the expansion of wavefronts with constant phase. In the (x, y') domain, such solution provides an approximation of the arrival time of a given wavefront everywhere in the domain. Following the ray theory, potential wall-thickness reductions in the pipe correspond to changes in the velocity field, affecting

thus the arrival times of the Lamb modes. By monitoring these variations in the arrival times, it is possible to make correlations to the fd product and thus invert them into the current thickness of the pipe. The speed c could be either the group or phase velocity depending on the application and frequency range. To have accurate inversions, it is essential that the chosen symmetric (S) or asymmetric (A) Lamb mode be in a highly dispersive region meaning that it will be sensitive enough to small variations in thickness. At frequency range between 1 MHz and 1.4 MHz, the phase velocity of A_o is the most attractive due to its dispersiveness and thus was chosen as the best candidate for the acoustic modeling.

An approximate solution to Eq.(2.13) could be obtained numerically using the fast-marching method (FMM) proposed by Sethian [29], which is based on Dijkstra's algorithm that is capable of calculating the shortest path between nodes in a graph. The FMM adds to Dijkstra's algorithm an upwind finite-different scheme to approximate the gradient which enables the calculation of propagating continuous wavefronts in arbitrary velocity models. The FMM initially requires the discretization of the (x, y') domain of the pipe in a regular grid in which every grid point is assigned a velocity value C_i according to Figure 2.20. Based on these values and given an initial arbitrary shaped wavefront, the algorithm estimates the shortest path and thus the arrival time of the wavefront at each node of the grid. While the solution to the eikonal equation does not consider the scattering that occurs when helical paths intersect, it is still a robust and consistent approach to approximate the arrival times in the problem [30], [31]. In addition, Eq.(2.13) is solved with the FMM in a fraction of a millisecond which is great advantage over the FEM.

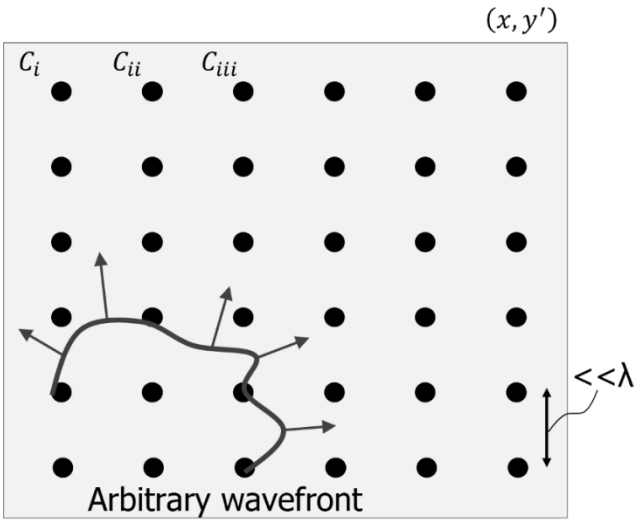

Figure 2.20: Discretization of the 2D acoustic domain, and velocity assignment at each node based on the assumed fd product. The FMM is then utilized to solve the problem.

2.4. Two-step corrosion assessment

The proposed corrosion assessment methodology consists of two main steps: 1) corrosion localization (CL), and 2) corrosion sizing (CS). Corrosion localization is achieved by using an algebraic reconstruction technique (ART). The localization data obtained in the first step, are then used in the second step of the methodology, where the acoustic wave equation described by Eq.(2.13) is solved iteratively, to minimize the phase velocity travel time of the A_0 between the experiment and 2D acoustic model. The overall methodology is outlined in Figure 2.21.

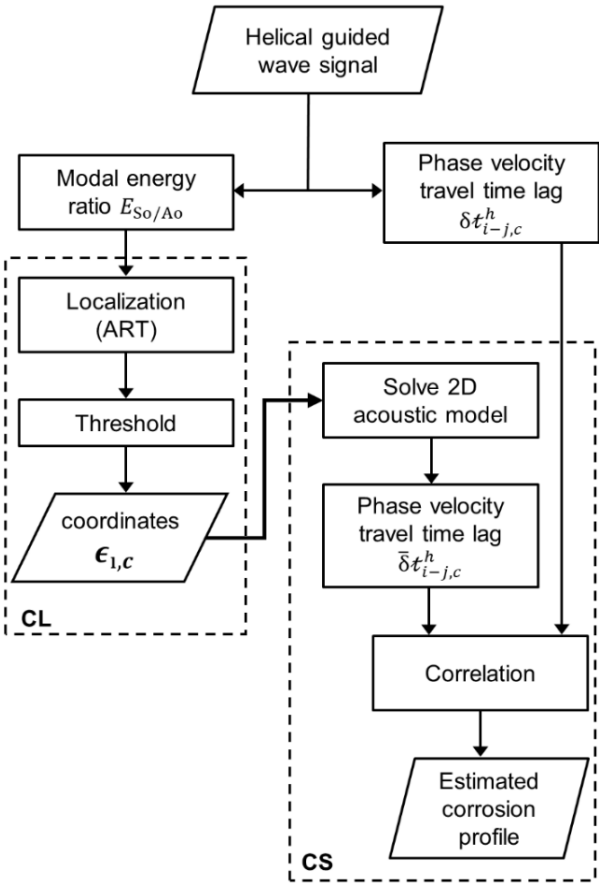

Figure 2.21: Flow chart of the proposed corrosion assessment methodology.

2.4.1. Corrosion localization

In general, algebraic reconstruction algorithms model the medium as an array of unknowns and then attempt to construct algebraic equations for these unknows in terms of measured quantities, e.g. attenuation, travel-time [21]. These algorithms offer an efficient alternative to probabilistic reconstructions due to their ability to handle sparsity extremely well. The algebraic reconstruction algorithm (ART) is suitable for quantitatively mapping low-contrast, similar-to-incident wavelength damages in pipes. [32]. In this work, the potential of ART to be used as localization scheme for a large internal corrosion damage, is exploited. For the sake of clarity, the implementation of the ART algorithm is here briefly summarized. The overall procedure can be described by a set of linear equations according to

$$\boldsymbol{A}_{(m\times n)}\boldsymbol{x}_{(n\times 1)} = \boldsymbol{d}_{(m\times 1)} \tag{2.14}$$

with $\boldsymbol{A}$ being the weight matrix, $\boldsymbol{d}$ the damage coefficient vector and $\boldsymbol{x}$ containing the unknowns. Implementation of the ART first requires the consideration of multiple replicas of the pipe's unwrapped surface to allow all helical rays to be represented by straight lines and the resulting surface is then discretized in square cells. Every helical ray has a row vector entry $\boldsymbol{w}_{1\times n}^{i-j}$ in the weight matrix $\boldsymbol{A}$ with length equal to the total number of the cells n in the problem. This vector $\boldsymbol{w}_{1\times n}^{i-j}$ contains a metric of the influence of the given helical ray to the specific cell estimated by the length that intersects that cell and by excluding any refraction effects this operation becomes linear. The total number of rows m in the weight matrix $\boldsymbol{A}$ corresponds to the maximum number of individual helical rays considered in the problem. The right side of the Eq.(2.14) requires the estimation of the damage coefficient $\boldsymbol{d}$ which represents the baseline difference of a certain quantity for each helical path considered in the problem. The attenuation of either A_0 or S_0 could serve as damage coefficient, since the first was found to be robust in detecting similar to wavelength defects, and the second sensitive in large shallow defects [9], [21]. In this work, the modal energy ratio E_{S_0/A_0} attempts to combine the attributes of both modes and was defined as the non-dimensional ratio:

$$E_{i-j,c}^{h} = \frac{\mathcal{H}\left(s_{(i-j)}^{(h,S_0)}\right)}{\mathcal{H}\left(s_{(i-j)}^{(h,A_0)}\right)} \tag{2.15}$$

where $\mathcal{H}$ is the peak of the envelope of the Hilbert transformed signal of the corresponding pair of actuator-receiver $i-j$ of the helical order h. Each mode was isolated in time by dividing its helical path length with the corresponding group velocity $t_{i-j}^{h} = l_{i-j}^{h}/C_{gr}$. The damage coefficient ($\boldsymbol{d}$) is thus calculated according to

$$\boldsymbol{d}_{\mathrm{i-j,c}}^{h} = \left(\frac{E_{i-j,0}^{h} - E_{i-j,c}^{h}}{E_{i-j,0}^{h}}\right)^2 \tag{2.16}$$

where, subscripts 0,c denote the damage free and current states of the pipe, respectively. Column vector $\boldsymbol{x}$ with size n contains the unknowns for every cell that the problem will be solved for. Solution to this system of linear equations can be obtained by an iterative scheme based on Kaczmarz's method as follows:

$$\vec{\boldsymbol{x}}^{(i)} = \vec{\boldsymbol{x}}^{(i-1)} + \frac{\boldsymbol{d}_{(\mathrm{i})} + \vec{\boldsymbol{x}}^{(\mathrm{i}-1)} \cdot \vec{\boldsymbol{A}}_{\mathrm{i}}}{\vec{\boldsymbol{A}}_{\boldsymbol{i}} \cdot \vec{\boldsymbol{A}}_{\boldsymbol{i}}} \vec{\boldsymbol{A}}_{\boldsymbol{i}} \tag{2.17}$$

Once the method converges to a solution, the additional replicas considered initially, are superimposed to yield the physical unwrapped surface of the pipe, and the corresponding value of each pixel is normalized to the maximum. This produces an image whose pixels intensity shows areas that according to the energy ratio depict potential damage.

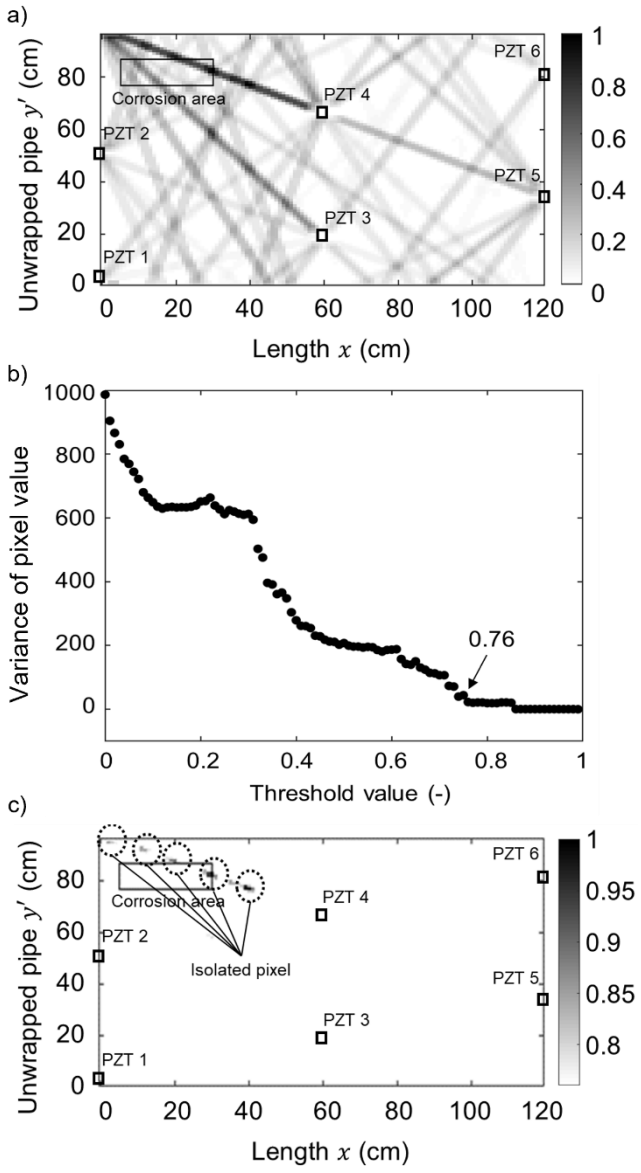

Figure 2.22: Thresholding the output of the ART to localize areas depicting damage. a) example of image obtained by using the ART, b) estimation of the optimal threshold point and c) the filtered output.

To extract information from the image, a threshold must be applied to help isolate the pixels with the highest algebraic values and eliminate potential artifacts. By varying the threshold level and plotting the variance of the pixels that are active at each step, it is possible to identify an approximate value at which the image becomes stable. Clusters of pixels appear in the image after thresholding, thus for every cluster the one with highest intensity is considered. The coordinates

are stored in vector $\epsilon_{\iota,c}$ where ι the number of coordinates extracted from each image at current state of the pipe c. Figure 2.22(a) shows a typical image output of the ART based on the experimental readings of the six-sensor layout and Figure 2.22(b) the corresponding variance plot. Choosing a threshold is a manual procedure, thus the value needs to be larger than 0.5 and in a flat region of the variance plot. For the case in Figure 2.22(b**)** threshold was chosen around 0.76 which enables the isolation of the pixels that are close to the corroded area as shown in Figure 2.22 (c**)** and of whose Cartesian coordinates will be passed to the second step of the methodology.

2.4.2. Corrosion sizing

The corrosion sizing process assumes a single, Gaussian-shaped damage that is described by three parameters $l_1,\ l_2,\ t_w^c$, the first two representing its circumferential and meridional extent and the latter corresponding to the current thickness at its center. Other shapes could also be considered by introducing additional parameters, although this typically works in the expense of the overall computational efficiency of the algorithm. Parameters $l_1,\ l_2$ are chosen to range between the smallest size of damage that straight ray tomography can detect i.e., the width of Fresnel zone, and a maximum no larger than the smallest distance between the PZT's attached on the pipe. Parameter t_w^c ranges from 0 to initial undamaged thickness t_w^o. For a given set of values of $l_1,\ l_2,\ t_w^c$ the assumed corrosion profile cp is constructed according to:

$$\mathrm{cp} = \mathrm{t_w^o} - \exp\left((-l_1^2 - l_2^2) * \{(t\}_w^o - t_w^c)\right) \tag{2.18}$$

and then translated to a phase velocity distribution using the dispersion relationships. A typical example of the constructed cp is illustrated in Figure 2.23. For each state c of the pipe, CS accepts the coordinates $\left(x_{\epsilon_{\iota,c}}, y_{\epsilon_{\iota,c}}\right)$ from vector $\epsilon_{\iota,c}$ one at a time and places the center of cp velocity distribution at that coordinate location on the 2D-(x, y') acoustic grid. The centroid of the cp velocity distribution is replicated κ times in coordinate locations $(x_{\epsilon_{\iota,c}}, y'_{\epsilon_{\iota,c}} \pm \kappa\pi D)$ according to the maximum number of helical orders h considered. The remaining nodes of the grid are assigned the undamaged fd product phase velocity. An additional parameter r is then introduced, to allow

the assumed *cp* velocity distribution to be shifted in the area around the initial coordinate location provided by $\epsilon_{\iota,c}$. This has the potential to reduce uncertainties derived from localization and potentially increase the location accuracy. The eikonal equation is solved sequentially for the range of the four parameters $\mathscr{g} = (l_1,\ l_2,\ t_w^c, r)$ assuming that the initiation of the wavefront happens at a single location. This process is repeated for the total number of the transducers n, while the phase velocity travel time $t_{i-j,c}^{h,\mathscr{g}}$ is calculated at $n-1$ nodes corresponding to the receivers. Baseline subtraction is then performed on the estimated travel time to define the simulated set of travel time lag $\bar{\delta}t_{i-j,c}^{h,\mathscr{g}}$ according to:

$$\bar{\delta}t_{i-j,c}^{h,\mathscr{g}} = t_{i-j,0}^{h} - t_{i-j,c}^{h,\mathscr{g}} \tag{2.19}$$

with $t_{i-j,0}^{h}$ being the undamaged travel time.

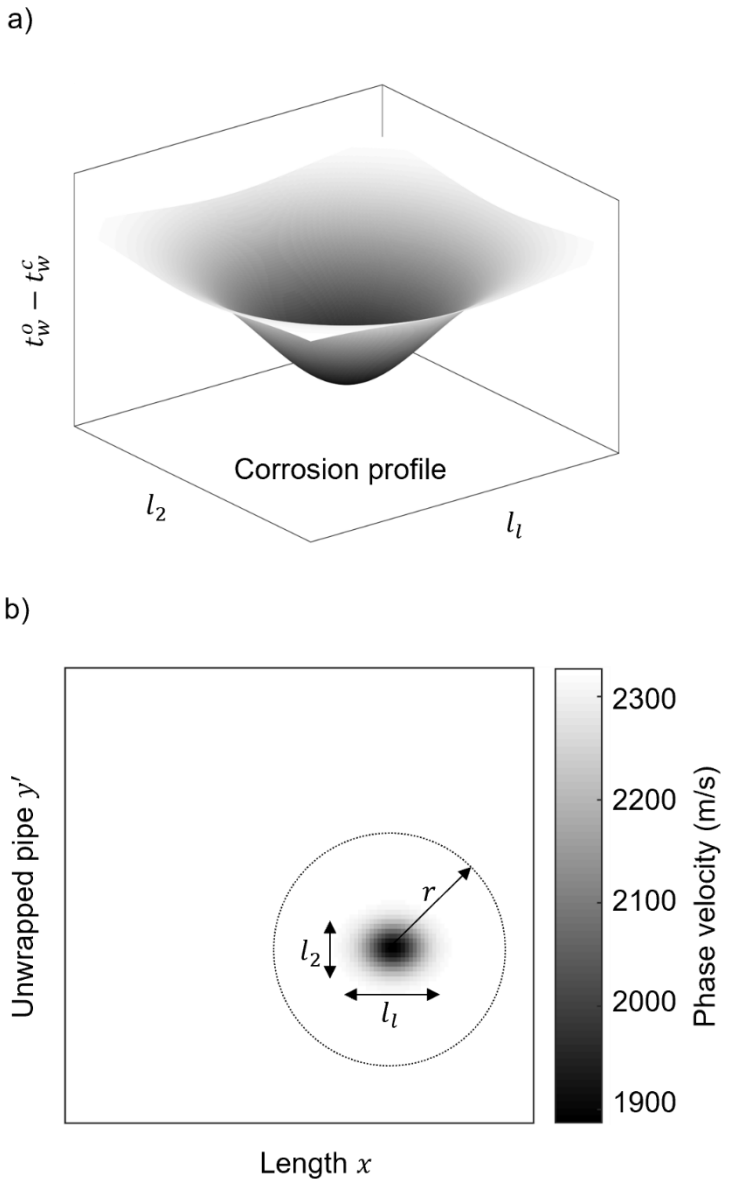

Figure 2.23: Modeling of a local wall-thinning in the 2D acoustic model. a) A Gaussian shaped phase velocity distribution defined by l_1, l_2, t_w^c and b) the corresponding phase velocity distribution that runs in the area confined by $r = 5$ cm.

The observed set of travel time lag $\delta t_{i-j,c}^h$ is calculated using the zero-crossing method [33], in the same manner as in Eq.(2.19**)**. The combination of the parameters $\mathcal{g} = (l_1, l_2, t_w^c, r)$ that minimize the simulated and observed travel time lag for all coordinates $\epsilon_{\iota,c}$ is the final estimated profile of the corrosion, according to:

$$I_c^{\mathscr{g}} = \min\left(\sum \left| \frac{\delta t_{i-j,c}^{h} - \bar{\delta} t_{i-j,c}^{h,\mathscr{g}}}{\delta t_{i-j,c}^{h}} \right| \right) \tag{2.20}$$

2.4.3. Test 3 – Accelerated corrosion

An accelerated corrosion test was performed inside a steel pipe using the impressed current technique [34], [35]. The test specimen was a 1.52 m (5') long carbon steel pipe with outer diameter and wall thickness of 304.8 mm (12 in.) and 3.4 mm (0.13 in.) respectively. Saltwater solution was sustained in the pipe by a rectangular Plexiglas tank of approximate size 250 mm × 100 mm that was installed in the six o'clock location and 160 mm (7 in.) away from the pipe edge. The tank was attached to the steel surface using epoxy adhesive and sealant was applied to the perimeter to avoid potential leakage. Direct current was applied to the saltwater solution through the stainless-steel wire mesh that was secured around the tank. The pipe was instrumented with six PZTs of diameter 6 mm, in pairs of two diametrically opposed. These pairs where 0.6 m apart and with 30° relative angle between them. The layout of the PZT transducers was chosen in order to minimize the overlapping between helical modes 15. Waveforms were generated using a 20 MHz Bandwidth, 1-Channel, 14-Bit PXI waveform generator and recorded with a 60 MHz, 12-Bit PXI oscilloscope. Each PZT signal was amplified using OLYMPUS 5560B with a gain of 40 dB, averaged with 1000 samples and had a total duration of 1.5 ms. An overview of the experimental setup is shown in Figure 2.24. The test was concluded after 10 cycles during which the remaining thickness was estimated using conventional pulse-echo. Readings were taken at the outside bottom of the cylinder, on a 7 × 5 rectangular grid using a 10 MHz probe as shown in Figure 2.24 (b).

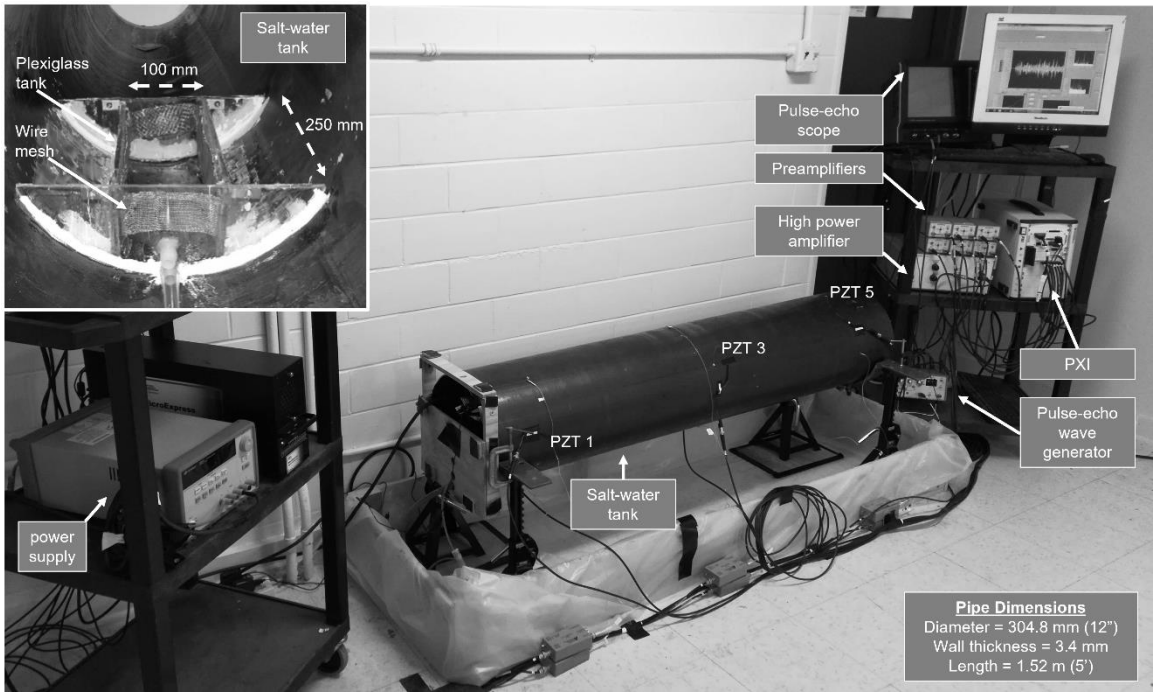

Figure 2.24: Overview of the experimental setup. a) View of the salt-water tank inside the pipe and b) the corroded surface of the pipe during the test

At each cycle of the corrosion test the following steps were carried out: 1) remove the saltwater from the tank; 2) perform pulse-echo measurements; 3) perform helical guided wave inspection; 4) refill the tank with saltwater; 5) apply a five-hour DC current (5A, 20V). The test was concluded at cycle no.10 where the remaining wall thickness was approximately half of the initial. The remaining thickness of the pipe t_w^c after each cycle, was estimated based on the Faraday's law of electrolysis:

$$\mathrm{t}_w^c = t_w^o - \frac{M_{Fe} I t}{2 F A_c \rho_{Fe}} \tag{2.21}$$

The values of the variables and constants used in Eq**.** (2.21**)** are summarized in the Table 2.2. According to the theoretical model, the wall thickness was reducing at a rate of 0.154 mm/cycle that correlates well with the pulse-echo readings. Faraday's relation as well as the images of the water tank reconstructed from pulse echo are shown in Figure 2.25. To obtain the thickness profiles of the water-tank according to Figure 2.25 (b) cubic interpolation was performed on the original pulse echo-grid data.

Table 2.2: Variables and constants used in Eq**.** (2.21**)**

Variables & Constants	Value
Initial thickness $\boldsymbol{t_w^o}$ (m)	0.0034
Molar mass $\boldsymbol{M_{Fe}}$ (mol/kg)	0.055845
Current **I** (A)	5
Faraday's constant	96485.3329
Steel density $\boldsymbol{\rho_{Fe}}$ (kg/m^3)	7800
Corroded region area $\boldsymbol{A_c}$ (m^2)	0.025
Elapsed time $\boldsymbol{t}$ (h)	5 hr./cycle

Considering five helical orders propagating between all sensor pairs for the PZT layout resulted in a total of sixty unique helical paths. The illustration of these paths in the 2D (x, y') domain is shown in Figure 2.26. A distinction between those paths propagating through the corroded area and the ones propagating away from it, is also performed using purely geometric characteristics of the HGUW. It was estimated that 21 of these paths intersect the corrosion area, while the total length of intersection ranged from 5 cm to15 cm.

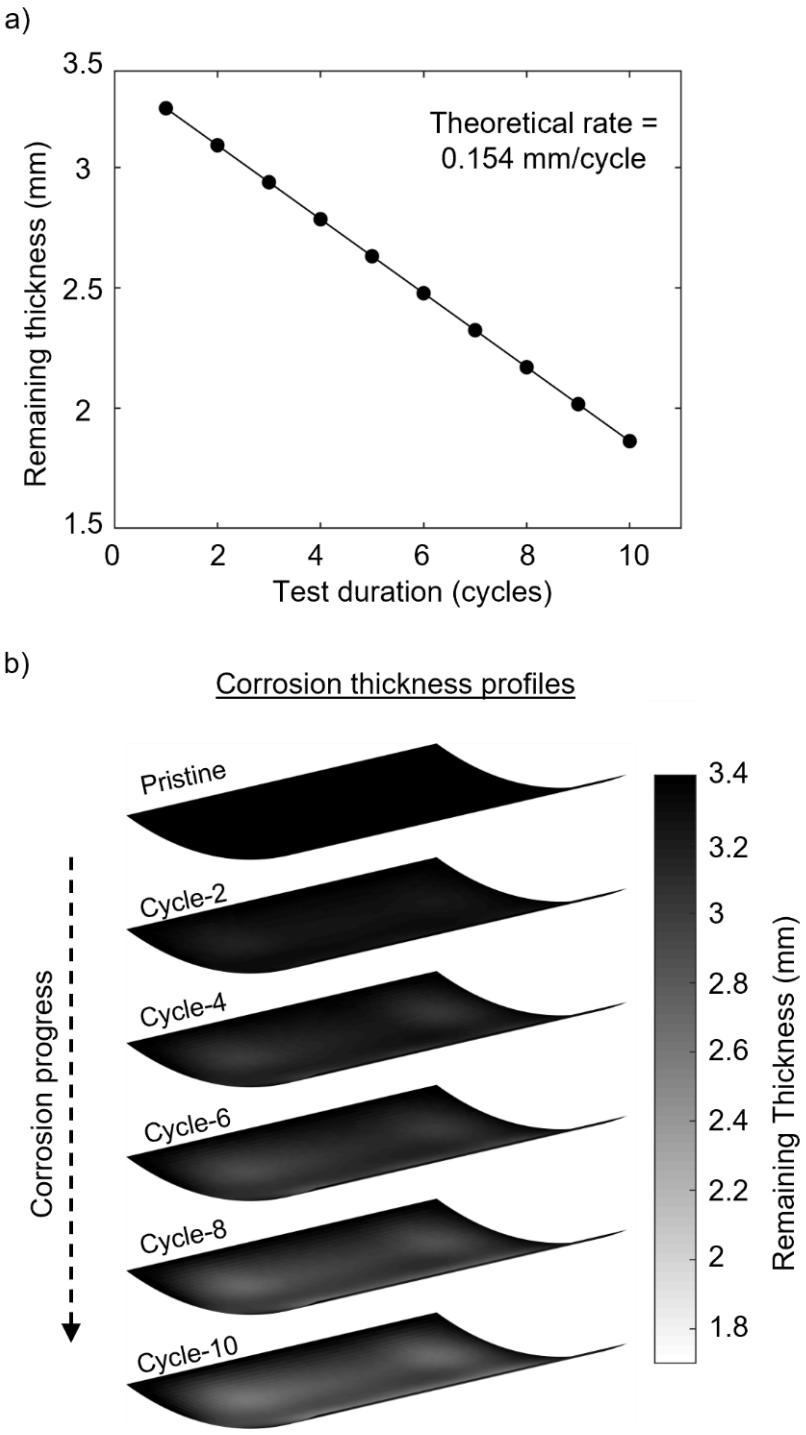

Figure 2.25: Estimations of the remaining thickness of the corroded area for every cycle of the test based on a) the Faraday's Law of electrolysis and b) Pulse-echo measurements on the bottom side

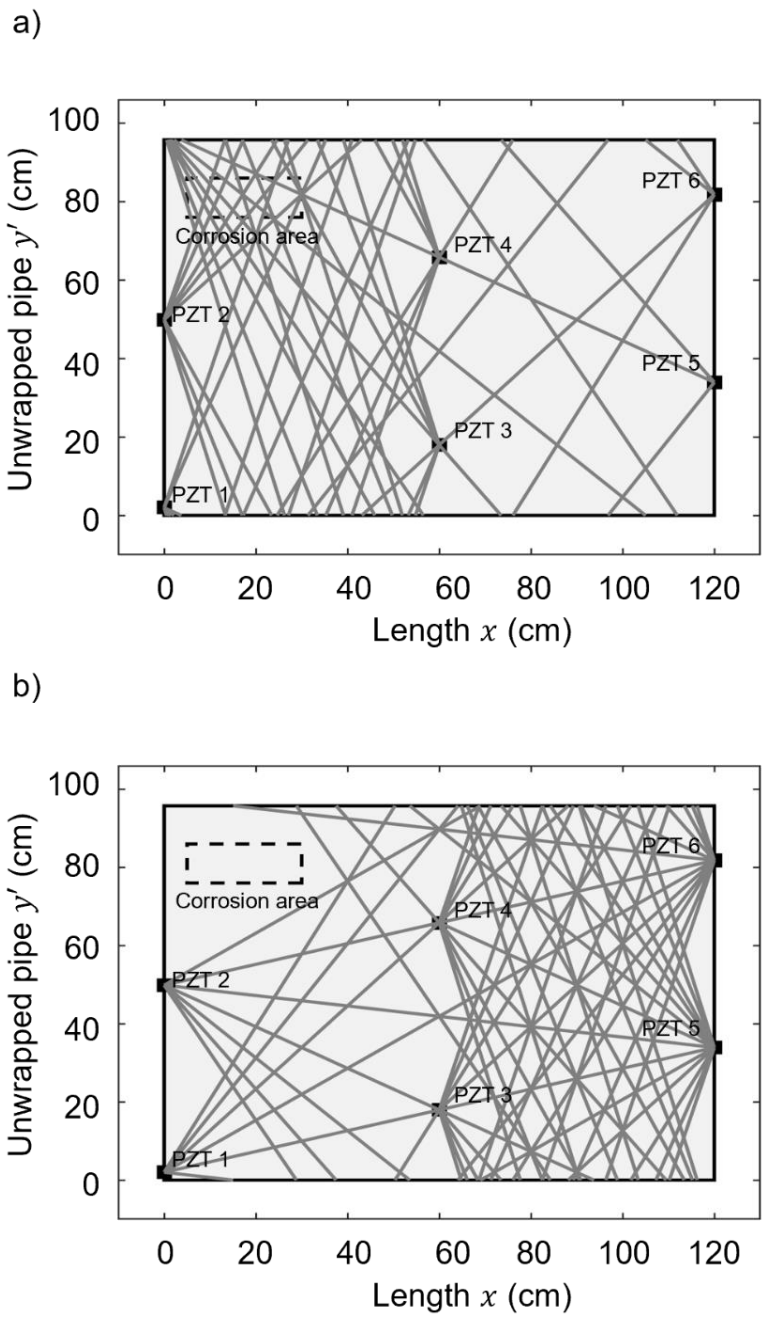

Figure 2.26: Demonstration of the five helical orders considered in the problem. a) The paths traveling though and b) the paths traveling away from the corrosion

The output coordinate locations of the CL step, $\epsilon_{\iota,c}$, are presented in Figure 2.27 for cycles 1-10 of the experiment. Overall, it can be observed that the proposed ART scheme can accurately depict potential damage locations in the pipe surface, since most of the coordinate points are

gathered around the corrosion patch. Outliers away from the actual corrosion area are present only during the first cycles of the test, suggesting that the localization process is progressively getting more accurate. This is quantitatively demonstrated by normalizing the distance of each coordinate in $\epsilon_{\iota,c}$ to the corrosion area, with the maximum potential distance on the pipe for every cycle of the test. Cycle 1 has an overall accuracy of 86.6% while cycle 10 reaches accuracy of 96.6%. The cumulative damage coefficient d_m was also calculated for the experimentally estimated energy ratio based on Eq.(2.16) and the results are presented in Figure 2.28. The energy ratio of the helical paths intersecting the damaged region shows to be much more sensitive compared to the paths propagating in pristine material which strongly agrees with conclusions drawn from the finite element models. While numerically the cumulative damage coefficient of the through-corrosion paths has an increasing monotonic relation with the corrosion progression, experimentally such relation is not observed. This might originate from the sensitivity of the PZT to each mode, considering that a disk-like sensor is attached on a curved surface. Despite this mismatch, the overall sensitivity of the energy ratio shows strong correlation with the wall-thinning which is the main objective in the CL step.

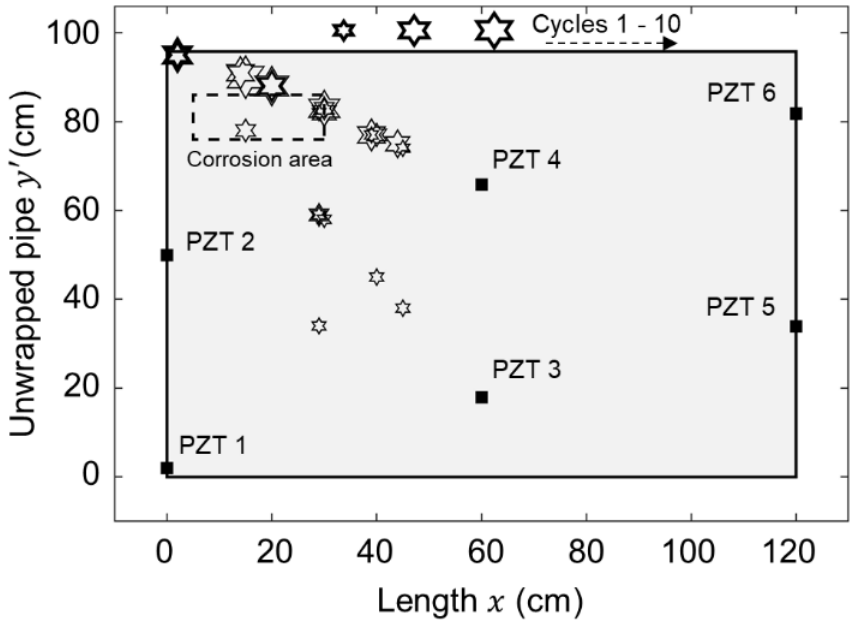

Figure 2.27: The output coordinate locations of the ART localization ($\epsilon_{\iota,c}$) for cycles 1-10.

Findings of the CS are summarized in Figure 2.29**.** The estimated corrosion profiles are presented for the corresponding test cycles 2, 5, and 10. In terms of sizing the corrosion patch, the proposed scheme is shown to perform well even in the early stages of the test. Thickness loss was estimated to be around 5%, 25%, 47% for the three cycles in which the thickness loss was expected to be 10%, 25%, and 50% respectively. Regarding the overall shape of the corrosion patch, cycles 2 and 5 slightly underestimate it, suggesting a more circular profile, while in the case of the 10^{th} cycle the reconstructed shape approaches a more elliptical shape with dimensions almost exact to the original damage. A possible source of error especially in the early stages of the corrosion process (large fd products), is the fact that the phase velocity of the A_0 experiences less dispersion adding some uncertainty to the numerical and experimental data correlation. This rapidly changes once the wall thickness loss nears a quarter of the initial thickness loss and the phase velocity enters a much more dispersive region.

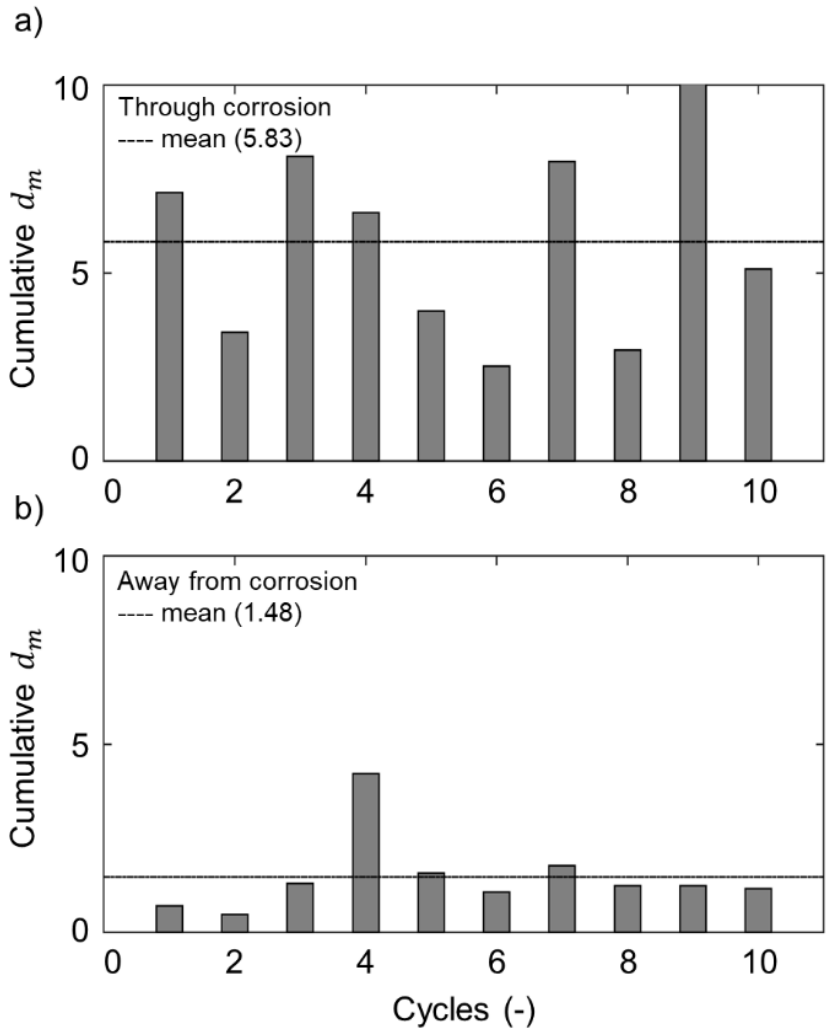

Figure 2.28: The cumulative damage coefficient d_m extracted experimentally for each cycle for the helical rays that a) interfere and b) do not interfere with corroded area.

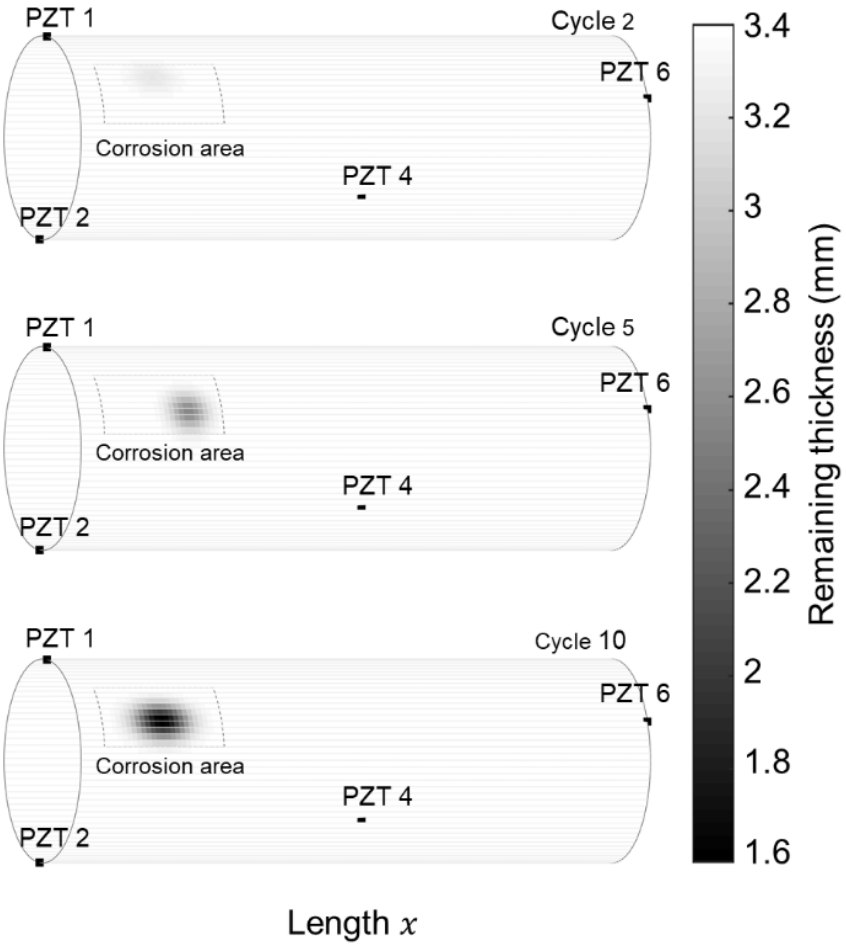

Figure 2.29: The CS estimations for cycles 2, 5, and 10.

Furthermore, allowing the parametrization of l_1, l_2, t_w^c in a distance r from the initially estimated coordinate point, aided overall in improving that initial estimation according to Figure 2.30. The gray markers, representing the center of the estimated remaining thickness profiles, have a noticeable improvement in their accuracy suggesting that CS has the capacity to also improve the localization of the damage. Despite the additional accuracy that the parameter r is offering, a certain upper limit needed to be set (50 mm) to avoid increasing the computational time needed for solving the acoustic model

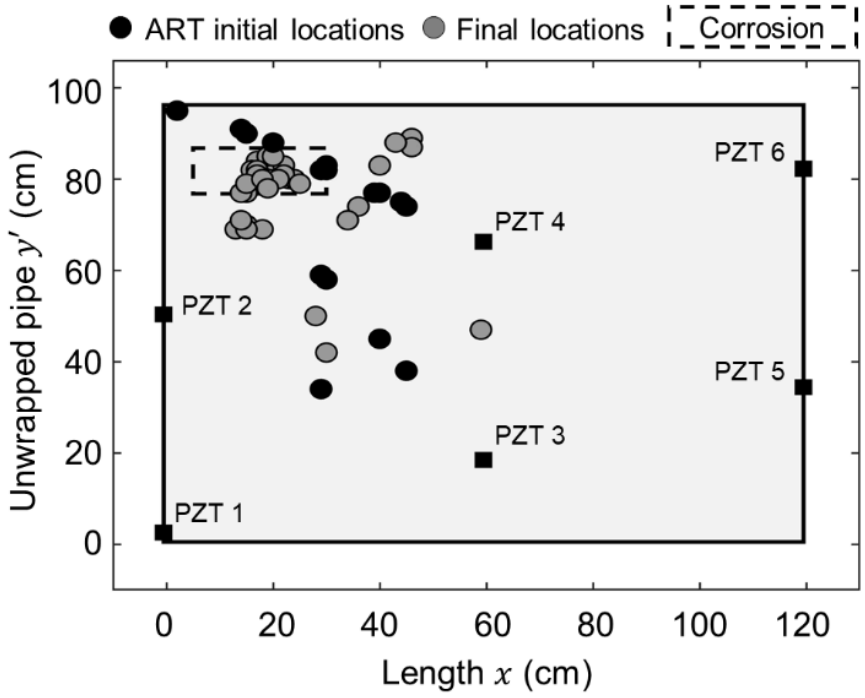

Figure 2.30: Accuracy improvement though the CS. Black marker shows the damage locations initially estimated by CL and grey markers the adjusted locations suggested by the CS.

2.5. Field test – Monroe Energy, Philadelphia

A field test was conducted from 8/30-8/31 at the facilities of Monroe Energy in Philadelphia with the coordination of Amerapex. This test involved the use of the active guided wave inspection using the HGUW. A segment of in-service pipeline was designated by Amerapex for conducting tests, which included both corroded and damage-free areas. An overview of the testing site is illustrated in Figure 2.31. The pipe was approximately 6 in. in diameter and 0.3 in. thick.

Figure 2.31: An overview of the experiments conducted at Monroe Energy.

Two 2-meter-long sections of the pipeline were instrumented with a total of nine piezoelectric disks each. The PZT's were attached using epoxy adhesive, and the layout followed the guidelines outlined in section 2.1.1. The objective of the experiment was to collect two sets of helical guided waves from sections A and B and then apply first the localization and then the 2-step corrosion assessment techniques. Section A was in an overall good external condition with no significant thickness loss at any location. In contrast, section B had at least three oval-shaped pits and an estimated thickness loss of at least 0.13 in. at these locations.

.

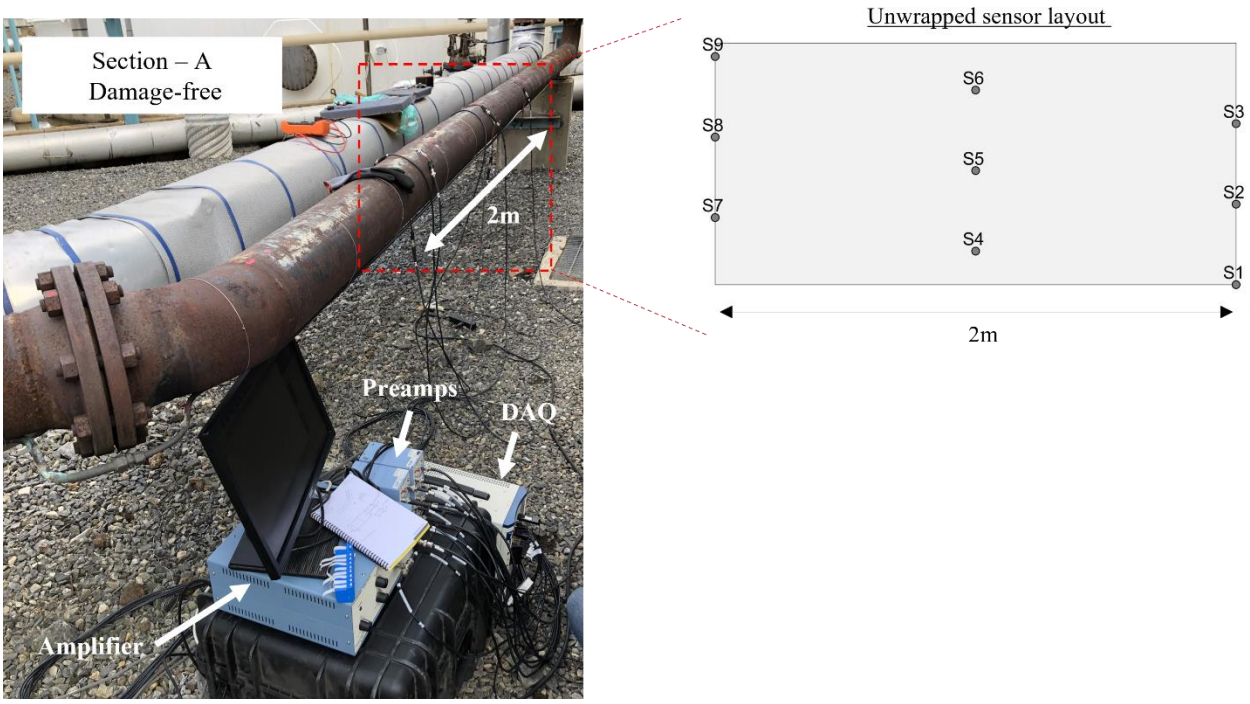

Figure 2.32: The damage-free section of the pipeline (Section A)

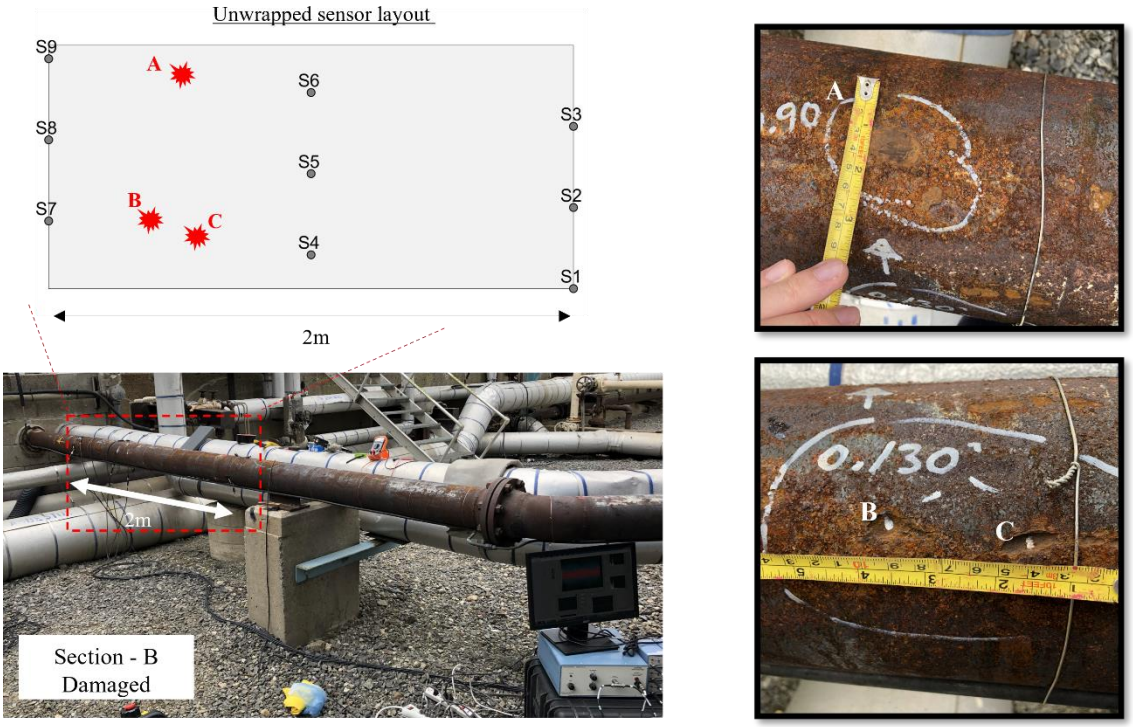

Figure 2.33: The damaged section of the pipeline (Section B)

The HGUW were excited using a frequency sweep between 50-250 kHz and amplified with 60dB. During the post processing of the time domain signals, the fast Fourier transform was initially used to investigate its frequency components. According to Figure 2.34 the signal is comprised of dominant frequencies up to 1.5 MHz which was far beyond the frequency of excitation. Bandpass filtering was also applied at the signal but since frequencies, more than 500kHz were initially dominant, it was impossible to maintain a large enough amplitude. Similar frequency content had been recorded from all the sensors in the test.

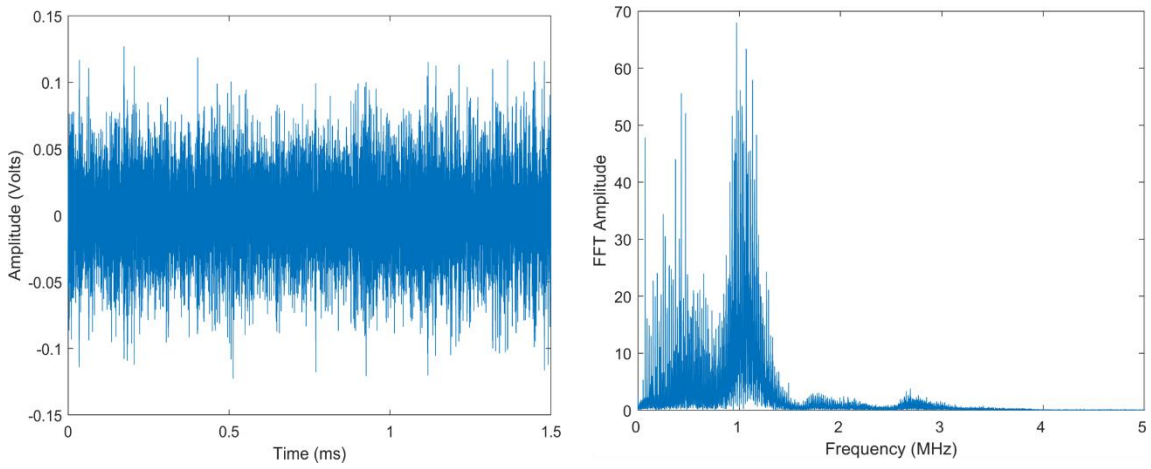

Figure 2.34: Typical time-domain signal and the corresponding Fast-Fourier transform.

Conclusions from the test

After an intensive effort to denoise the collected signals, we concluded that it was impossible to be used towards corrosion localization and for tomography purposes. We believe that the main contributor to this outcome was the poor contact of the PZT sensor to the pipe's surface. Typically, a smooth surface beneath the sensor is required for a proper ultrasonic excitation to occur. During the field test, it was impossible to locally create such ideal conditions primarily due to restrictions from the operator. In addition, the relatively high surface temperature of the pipe did not allow for the epoxy to properly dry out, thus resulting in a poor sensor-to-structure contact. Besides, vibrations were induced in the pipe from surrounding machinery leading to a very poor signal-to-noise ratio.

In future field tests, special attention should be given to the selection of the specimen and make sure that the locations of the sensors are not heavily corroded or extremely rough. An option would be to use sandpaper to locally smooth out the surface without compromising the thickness of the pipe. Also, an epoxy with a higher temperature rating can be used to overcome the issues of hot pipe surface and to ensure strong bonding of the sensor to the structure.

2.6. Summary

In this chapter, a comprehensive study on the theoretical aspects and practical considerations of the HGUW has been presented. It has been demonstrated that HGUW can be effectively utilized in large diameter pipes for both damage localization and imaging. This class of waves allow to consider multiple propagation paths around the cylinder's surface thus radically reducing the need for sensing units. An adopted ART has been developed for localizing different damages on the pipe's surface based on a baseline comparison of the fundamental Lamb modes. Furthermore, an approach for reconstructing the pipe wall thickness has been developed based on a 2D acoustic model. This algorithm allows to estimate the current thickness of the pipe using a parametric scheme that attempts to minimize the phase velocity from experimental readings and the numerical results. This approximation is valid when the damage profile is significantly larger than the incident wavelength.

During the collection of field-testing data, several practical issues introduced extremely high levels of noise in the collected signals making the application of the HGUW impossible. Such issues included the poor bonding of the PZT sensor to the pipe, the overall poor external condition, and the high surface temperature of the inspected pipeline.

3. Numerical modeling of HGUW

The finite element methods (FEM) for GUW modeling, has been a powerful tool which allows the study of various parameters that affect the propagation of the waves. Through parametric studies, it is possible to introduce different defects in the structure while exciting GUW's at different frequencies. Analyses can be carried out in both time and frequency domains, and typically the scattered field is monitored through nodal displacements. Most of the literature reports findings using simplified 2D models since they can be accurate and time efficient. Moser et al.[36] have set the foundation for properly using finite element procedures to solve guided wave propagation problems. They compared analytical solutions to finite-element models and concluded that FEM can be successfully used especially when analytical solutions are difficult to obtain which is the case for complicated geometries. Their work was based on 2-dimensional analyses that assume plane-strain conditions along the width of the waveguide. They also proposed guidelines for ensuring adequate temporal and spatial resolution of the FEM obtained solution. Lowe et al. [7] studied the reflection coefficient of the A_0 mode from rectangular notches and cracks of various sizes and depths. These defects have been introduced in the models by means of removing elements and creating step-like thickness variations. They used FINEL, an FEM program developed at Imperial College, and assumed 2D plane strain conditions. One of the significant outcomes of this study was that the A_0 mode is very sensitive when the depth of a notch is larger than the 20% of the initial thickness. In addition, they proposed applying anti-symmetric nodal displacements to excite pure A_0 mode in the model. More recent studies have considered 3-dimensional (3D) FEM models with more realistic defect modeling. For example, Howard et al. [37], [38] presented a numerical study, where the sensitivity of circumferential guided waves to wall thinning in pipes was evaluated based on both their reflection and transmission. They considered three Lamb modes S_0, A_0 and SH_1 propagating through different thickness profiles in a pitch catch configuration in the circumference of a pipe. It was reported that S_0 has the potential to be utilized when large and shallow defects are under investigation while SH_1 was more sensitive when used in transmission. They also highlighted that anti-symmetric A_0 is less sensitive compared to the other two modes. In addition to studying the interaction of guided wave modes with defects, the FEM have been also used for generating synthetic data which are used in inverse problems

dealing with guided wave imaging. Willey et al. [39] used the commercially available Multiphysics software COMSOL to simulate experimental datasets to be used in an iterative scheme that estimates the remaining thickness in a steel pipe.

The current section of this report is providing the framework for modeling the helical guided waves using the finite element method. While the literature is extensive on the modeling of guided waves, limited work has been reported on investigating the numerical modeling of HGW. First, a discussion is made on selecting typical parameters concerning the HGW like the excitation types, the numerical integration step, the element size, and ways to eliminate reflections using absorbing layers. Second, a sequence of models is presented which use approximately the same geometries of pipes used in experimental tests. The locations of PZT sensors used in experiments, are approximated by nodal displacement recordings in the FEM. The objective is to verify the efficiency and applicability of the proposed methodology presented in Chapter 3, in a noise-free environment. In addition, qualitative observations are made on the propagation of the fundamental Lamb modes and the scattered field when the modes are incident on corrosion-like wall thinning. The simulations presented in this report have been created using the ABAQUS commercial software and solved using ABAQUS-explicit [40], a time-domain solver based on explicit integration.

3.1. Modeling considerations

Excitation

Different approaches exist that allow the excitation of Lamb-type guided waves in a finite-element model. This can be achieved by either a nodal displacement or force. It should be noted that the displacement field imposed by guided waves is orders of magnitude smaller compared to pipe global vibration modes thus, no boundary conditions are required in finite-element modeling. Considering that no boundary conditions are imposed, a displacement excitation is easier to cause a model instability or rigid body movement. For this reason, unit force excitations are chosen.

Excitation of purely symmetric or anti-symmetric Lamb modes can be achieved by imposing equivalent distributions of nodal displacements through the cross-section of the cylinder as demonstrated in Figure 3.1. These forces attempt to reproduce the radial displacement

distribution of each of either symmetric or anti-symmetric modes. Regarding the 3rd force excitation, it has been reported that it is the most efficient approach to simulate the piezoelectric effect, without the requirement of elaborate simulations [26].

Element size & integration step

The overall accuracy of finite element modeling of elastic waves is dependent on the spatial and temporal resolution on the model. The largest size of a finite element l_{max} is related to the smallest wavelength λ_{min} expected in the analysis. To achieve appropriate spatial resolution, 10 nodes per wavelength are considered adequate [41] even though for increased accuracy studies have suggested using 20 or more nodes per smallest wavelength [42]. This condition is expressed as

$$l_{max} = \frac{\lambda_{\min}}{20} \tag{3.1}$$

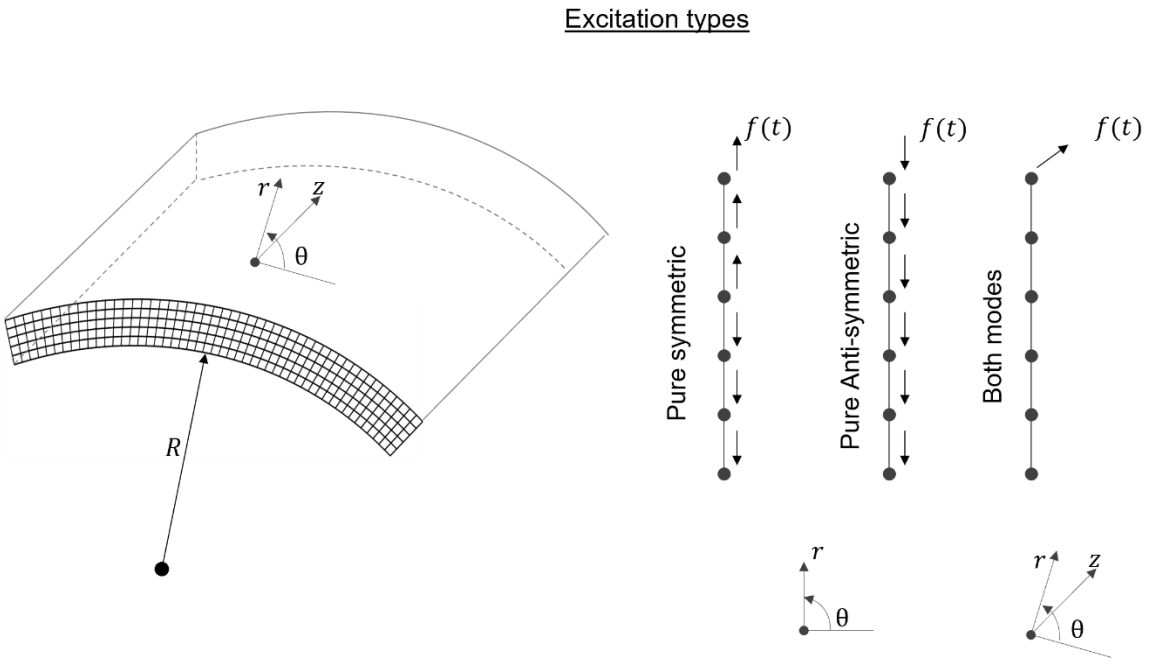

Figure 3.1: Demonstration of the input displacements required to excite different Lamb wave modes. Excitations may create pure symmetric and anti-symmetric Lamb modes or a piezoelectric-type input that contains both modes.

Typically, the A_0 mode is depicting l_{max} since it has the smaller phase velocity at frequencies below 1.5 MHz-mm. In addition, another condition must be met for through-thickness resolution according to

$$l_{max} = \frac{d}{10} \tag{3.2}$$

where d is the thickness of the pipe [43]. The stability of the numerical integration schemes is usually achieved by properly choosing the integration time step Δt . Stability is usually maintained using 20 points per cycle at the highest frequency [36] according to

$$\Delta t = \frac{1}{20 f_{max}} \tag{3.3}$$

although the smallest size of the element chosen in the mesh imposes another stability criterion typically

$$\Delta t = \frac{l_{max}}{C_d} \tag{3.4}$$

where the dilatational wave speed. The smallest value of Δt derived from Eq.(3.3) and Eq.(3.4) and is used in the analysis.

Non-reflecting boundaries – ALID

The easiest approach to minimize the effect of reflected waves is to extend the size of the finite element model such that reflecting edges are far from the area of interest. This approach is often convenient in 2-dimensional numerical models. Considering the size of the 3-dimensional pipe in addition to the required refinement in element size to capture high frequency perturbations, extending the FE model size is prohibitive because it leads to extremely large analysis times. Other methodologies exist to mitigate the unwanted reflections which are based on introducing a small number of finite element layers near the edges with gradually varying acoustic properties aiding to damping the energy of the incident wave. Two methodologies have been widely used and are

the Absorbing Layers with Increased Damping (ALID) and the Perfectly Matched Layers (PML) [44]. In this work, the ALID approach has been used due to easier implementation in ABAQUS.

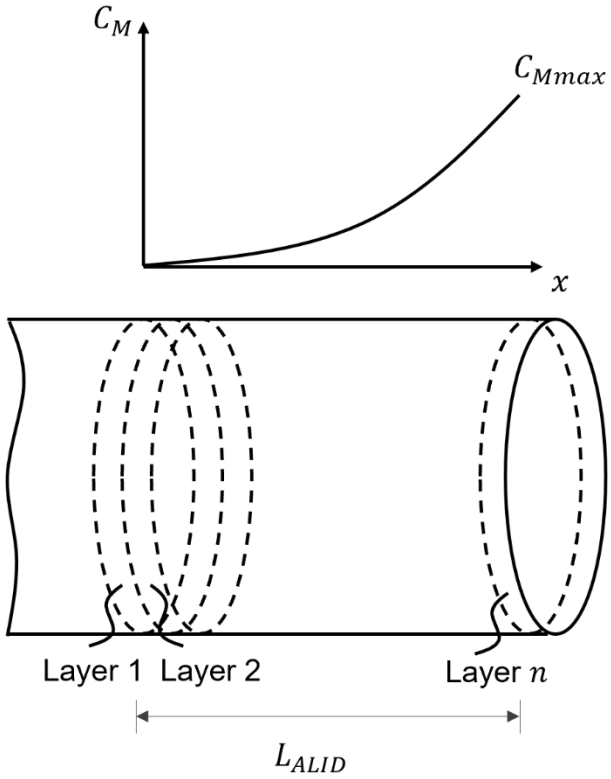

Figure 3.2: Details on constructing the ALID on the cylinder edge to avoid reflections. n number of FEM-width size layers needed, and each layer is assigned a progressively higher mass-proportional damping coefficient C_M.

ALID is based on introducing mass-proportional Rayleigh damping C_M in the layers adjacent to the model edge according to Figure 3.2. The required length of the ALID layer L_{alid} is typically decided using the maximum wavelength λ_{max} anticipated, according to

$$L_{alid} = \lambda_{\max} \times 3 \tag{3.5}$$

Over the ALID length, damping C_M varies according to a cubic law between 0 and a maximum value C_{Mmax} which is determined based on trial and error until a certain criterion of the amplitude of the reflection is met [45]. For guided wave applications at lower frequencies, C_{Mmax} can be taken as 2.1×10^6 thus the ALID profile can be expressed as

$$C_M(x) = C_{Mmax}\left(\frac{x}{L_{alid}}\right)^3 \quad (3.6)$$

According to studies [46], the change in C_M between adjacent layers of the ALID should be minimized thus its suggested to have one finite element per layer.

Other modeling parameters

Linear elastic conditions have been considered for all analyses. The elastic properties of steel are presented in Table 3.1. Linear 8-node elements (C3D8R) were used throughout the modeling. The analyses have been carried out on a on a workstation computer with an Intel Xeon W-2145 CPU clocked at 3.7 GHz and 64 GB of RAM.

Table 3.1: Elastic Properties of steel utilized in FEM simulations

Modulus of Elasticity (E)	210 (GPa)
Poisson's ratio (ν)	0.3 (-)
Density (ρ)	7800 (kg/m^3)

3.2. Scattering of the A_0 from 30 mm × 30 mm, 50% uniform wall thinning

The geometry of the FE model is demonstrated in Figure 3.3. The element size was 0.43 mm through the thickness and 0.8 mm in the other two dimensions. This corresponds to roughly 10 elements per wavelength in the longitudinal direction, eight elements in the through-thickness direction resulting in approximately 18 million elements. The stable time increment was set at 20 ns and the duration of the analysis was set at 1.5 ms. Anti-symmetric mode A_0 was excited by applying nodal forces in the radial direction and the excitation consisted of a 5.5 Hanning-windowed toneburst with central frequency at 300 kHz. The normal to surface displacement was recorded at the six exact locations of the piezoelectric PZT sensors used later in the corresponding experimental setup.

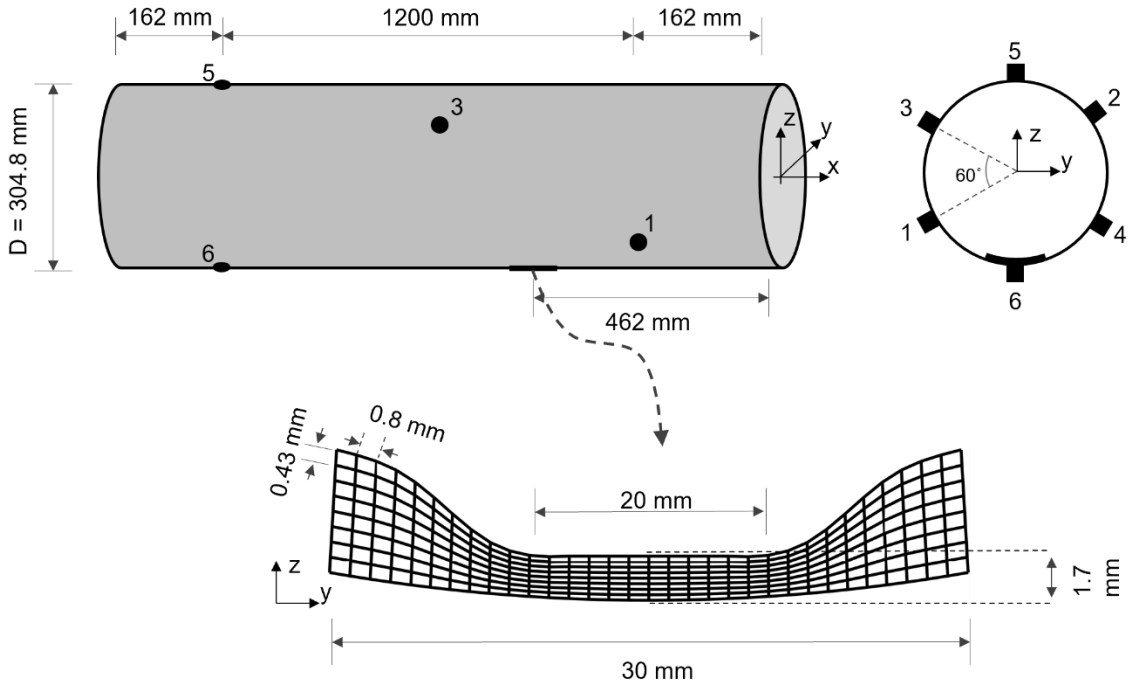

Figure 3.3: Finite element model constructed based on Experiment 1. The model geometry, the thickness loss profile, and the nodal recording locations.

Two different cases were considered. First, a defect free pipe was modeled. Then, corrosion-like damage (D1) was simulated on the inner surface of the pipe by reducing the wall thickness. This reduction was chosen to be 50% of the initial thickness of the pipe in order to be able to measure significant amplitude variation of the A_0 mode. Figure 3.3 shows the simulated damage, which was 30 mm × 30 mm (1.18 in. × 1.18 in.) in the longitudinal and hoop directions respectively. The damage-to-wavelength ratio was chosen to be around three to avoid total reflection or total transmission.

The accuracy of the ART localization relies on accurately measuring the differences of the modes in the pristine and damaged states of the pipe. Figure 3.4(a) presents the nine helical paths connecting sensors S1, S4 and Figure 3.4 (b) the corresponding typical time histories obtained from the numerical model. According to the helical paths presented, it is expected that the modes of the first, fourth, fifth, eight and nine helical orders will be affected by defect D1 as opposed to the rest of the helical order modes. This is demonstrated in Figure 3.4 (c) where the absolute value of the baseline subtraction is shown. Significant differences can be seen for the modes that interact with the damage and rather insignificant differences are observed for the rest. The presence of

edge reflections can be omitted for two main reasons. First, there is no temporal overlapping between reflections and the modes of interest. Second, any reflections from the edges of the pipe are usually being suppressed by the baseline subtraction. A close comparison of the arrival of the first helical order mode is made in Figure 3.4 (d). The direct interaction of the first helical order mode with the damage D1 seems to have significantly altered the phase velocity of the mode but at the same time has no impact on the group velocity, which basically remains the same. These quantitative differences can be observed in Table 3.2 after using Eq.(2.10). The damage coefficients of the modes interacting with the damage are notably higher compared to the rest of the modes.

The algebraic solution for the input set of damage coefficients $d_{i,j}^{m}$, calculated from the numerical model, is presented in Figure 3.5. The pixels having the largest absolute numeric value, belong to the area covered by the modeled damage as opposed to the rest of the image pixels which have significantly lower values. It should be noted at this point that the pixels corresponding to the locations of the sensors have naturally large numeric value after solution. This happens because there is a concentration of helical paths initiating at those pixels thus their effect is filtered out.

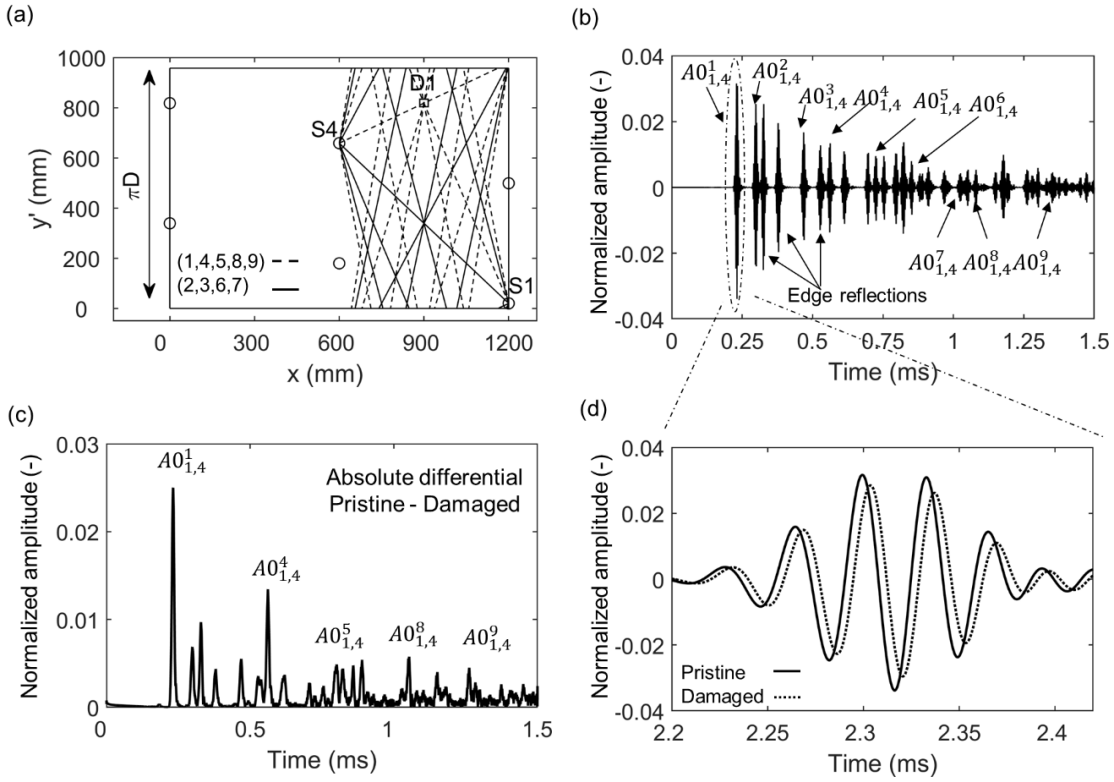

Figure 3.4: Demonstration of the interaction of the A0 mode with the simulated damage in the numerical model: (a) schematic of the nine helical paths between sensors S1 and S4, (b) typical normal-to-surface displacement at location of sensor S4, (c) the absolute value of the baseline subtraction, and (d) the magnified portion of the signal showing relative differences of the 1st helical order mode.

To isolate the locations in the reconstructed image with the highest numeric values, the following procedure had been followed. First the image is convoluted by a 3 × 3 moving window in order to accumulate contributions from nearby pixels, then the value of each pixel is normalized to the one with the maximum value and finally, cubic interpolation is performed to increase the resolution of the picture. The overall procedure is outlined in Figure 3.6. The final reconstructed image for the numerical model can be seen in Figure 3.6 (c). Perfect agreement between the exact location of the simulated defect and the reconstructed image can be observed. The image exhibits a minimum number of artifacts primarily due to exciting only the A_0 mode. Thus, without loss of generality, results obtained from the finite element model demonstrate the full capacity of the proposed algebraic reconstruction algorithm.

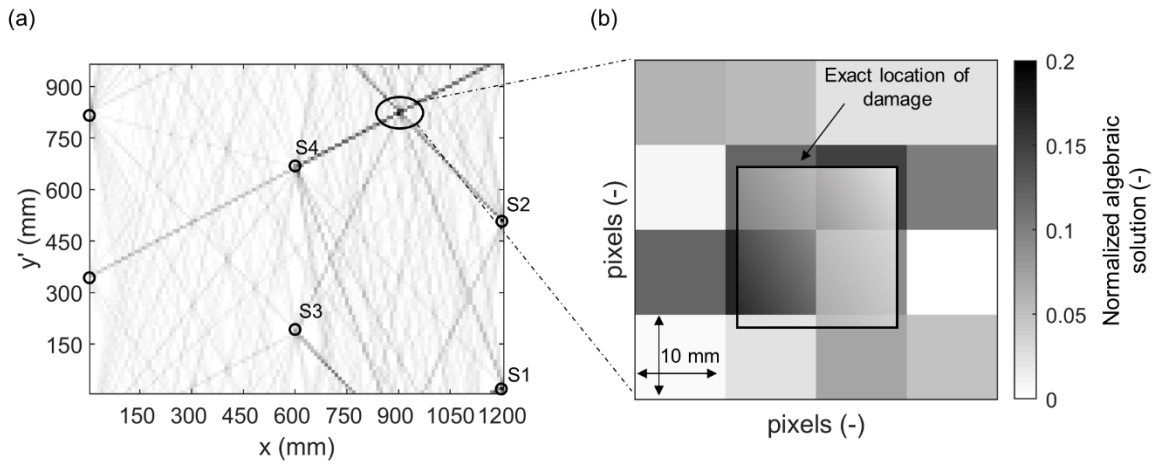

Figure 3.5: Normalized algebraic solution (before averaging) for the numerical model input damage coefficients $d_{i,j}^{m}$: a) unwrapped 2D pipe representation, b) focus on pixels corresponding to the actual damage location. Note: the color map is normalized with respect to the maximum in subfigure (a).

Table 3.2: Damage coefficient d when excitation happens at sensor S1

Sensor pair	1-3	1-4	1-5	1-6
d^1	0.00	0.50	0.01	0.00
d^2	0.00	0.08	0.58	0.00
d^3	0.00	0.14	0.05	0.16
d^4	0.06	0.70	0.16	0.04
d^5	0.02	0.07	0.00	0.08
d^6	0.06	0.05	0.05	0.22
d^7	0.09	0.58	0.02	0.03
d^8	0.18	0.63	0.04	0.27
d^9	0.20	0.10	0.05	0.09

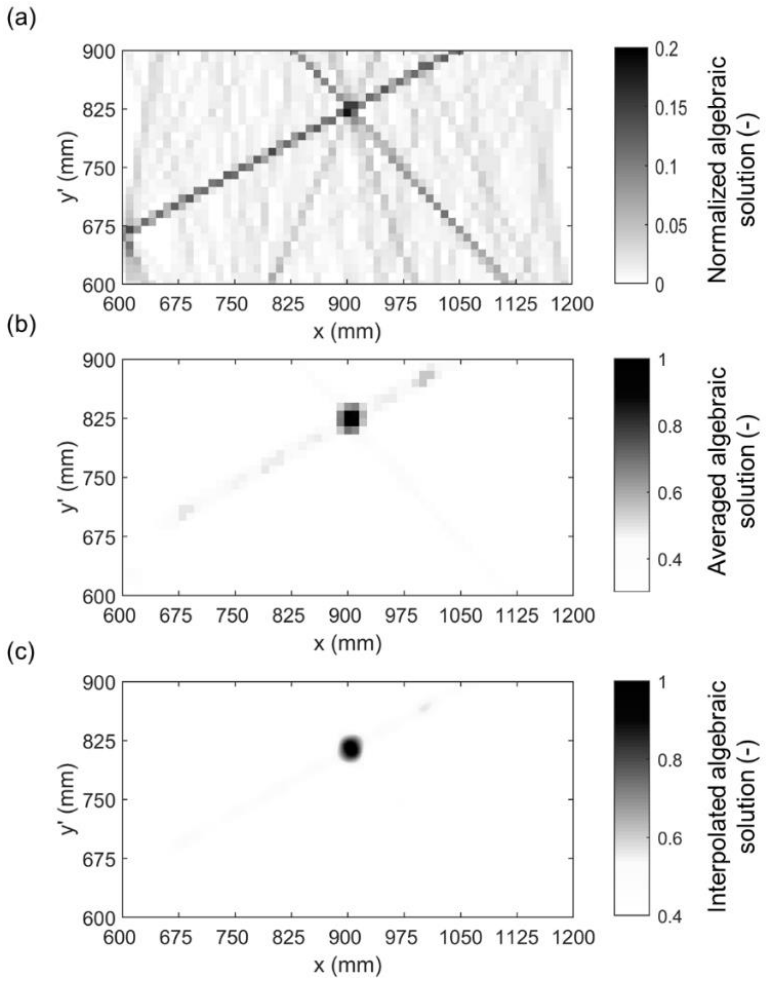

Figure 3.6: Procedure followed for isolating damage location and smoothing the reconstructed image a) solution from ART, b) averaged image, c) interpolated image

3.3. Scattering of the A_0 from a 50 mm × 30 mm, 30% uniform wall thinning

A 60-cm section of a 1.52 m (5 ft) long carbon steel pipe, with diameter and wall thickness of 30.48 cm (12 in.) and 3.416 mm (0.1345 in.) respectively was modeled according to Figure 3.7. The PZT sensors were modeled as displacement recording nodes, while the excitation was simulated by a tangential force on the surface of the pipe corresponding to the exact locations of the transmitting PZT sensor. The excitation frequency was chosen to be 300 kHz, which falls in the range of frequencies described in Chapter 2. Damage was introduced in the numerical model by reducing the wall thickness in the outer surface at the location corresponding to damage D1 by 30% which was the estimated in the experimental tests. In order to obtain adequate spatial and

temporal resolution, eight elements have been used in the thickness of the pipe, while 15 elements for the smallest wavelength in the propagation direction. Explicit solver was utilized to obtain time domain results with total duration 1 ms. Absorbing layers using the ALID have been used at the two edges of the cylindrical geometry to remove unwanted reflections.

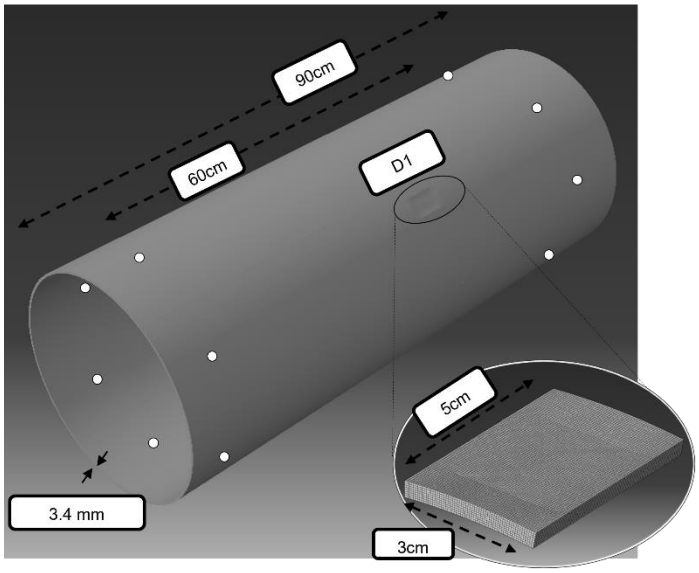

Figure 3.7: Finite element model details based on experimental test 2.

Figure 3.8 demonstrates the tomographic image obtained using the numerical model along with the typical time histories between sensors S3-S6. The reconstructed image has enough accuracy to localize the simulated damage and it is almost artifact free. The baseline subtraction signal between sensors S3-S6 clearly indicates that helical orders one, four and five have been significantly altered due to the interaction with the damage. The fact that the differential signal can isolate with such efficiency the affected modes, allows for the numerically obtained image to be accurate and experience minimal artifacts.

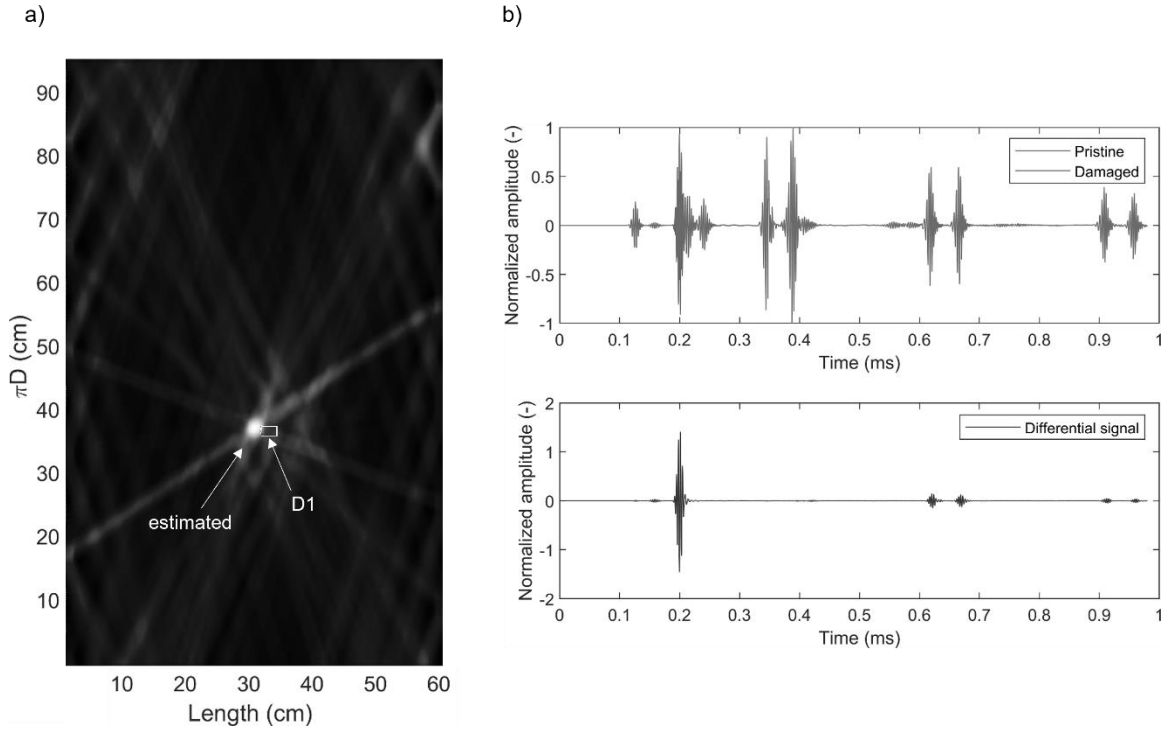

Figure 3.8: Results obtained from the numerical model a) reconstructed image b) time history and differential signals between sensors S3-S6.

3.4. Scattering of the S_0 & A_0 from a 250 mm × 100 mm, non-uniform wall thinning

A fundamental investigation of the sensitivity of the modal energy ratio E_{S_0/A_0} and the travel time lag δt was performed using a 3D finite-element model constructed using ABAQUS software. Solution of the guided wave problem was achieved using the time-domain explicit solver. Overall, the dimensions of the 3D model were identical to the pipe used in the experiment according to Figure 3.9. In a series of numerical analyses, the thickness profiles obtained experimentally using pulse-echo were incorporated in the model, more specifically for the damage free case and cycles 2,4,6,8,10 as it will be demonstrated in Section 2.4.3. Excitation of both the fundamental modes was achieved by using a Hanning modulated, 300 kHz tone burst in the longitudinal direction, tangent to the outer surface.

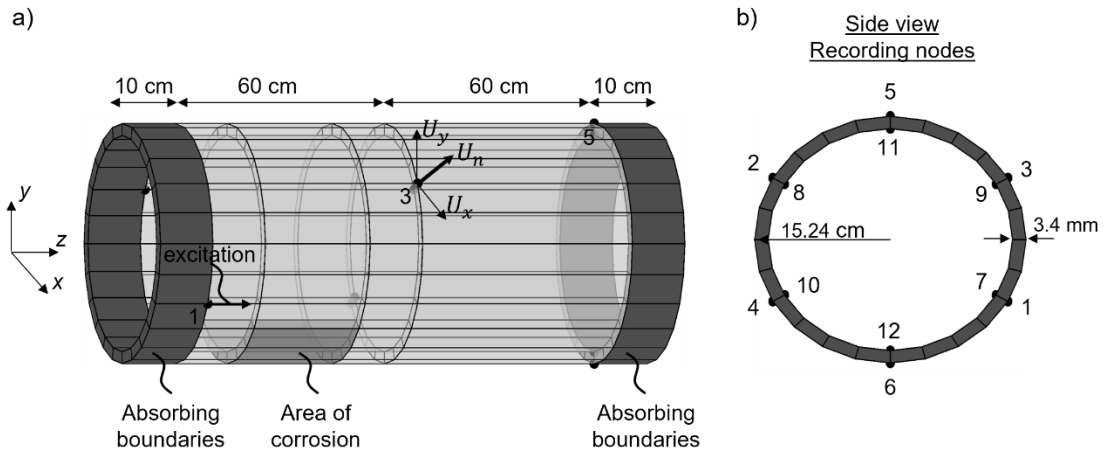

Figure 3.9: Finite element model in ABAQUS. a) 3D view of the pipe and b) side view showing the recording nodes

Cubic elements of approximate size 0.6 mm have been used to discretize the geometry resulting to approximate 32×10^6 nodes. Absorbing boundaries with a width of 10 cm were modeled at the ends of the cylinder using the absorbing layers with increased damping (ALID) to minimize any undesired reflections. In order to consider just the first five helical orders, the duration of the time domain analysis was set at 850 μs for all excitation-receiver pairs.

Two sets of nodes were introduced in the model, 1-6 representing the approximate locations of the PZT's used in the experiment, and 7-12 their inner opposite corners according to Figure 3.9(b**)**. Excitation of helical waves was happening one at a time from the nodes on the outer surface, while the remaining 11 were recording the displacement components in (x, y, z). Having the normal to surface displacement component at both free nodes of the cylinder, it was possible to use symmetry to isolate the A_o and S_o modes by adding and subtracting the signals [26].

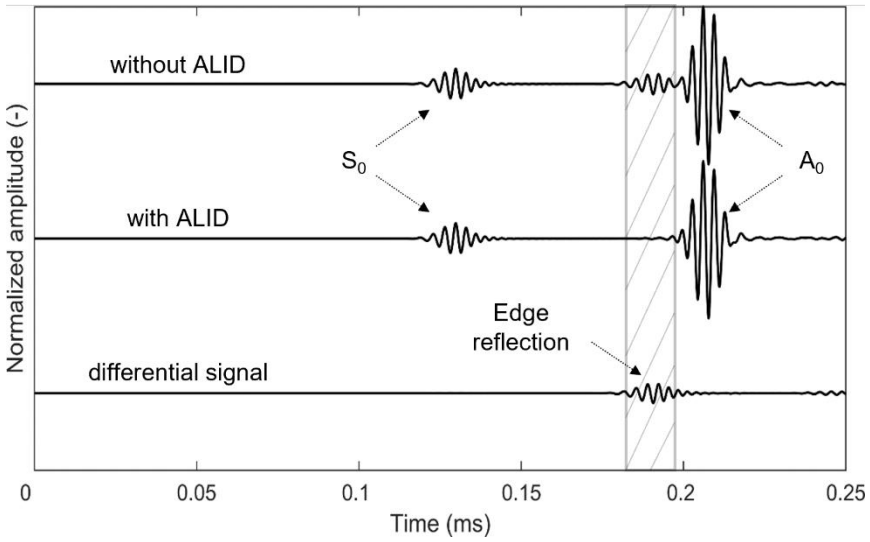

Figure 3.10: Typical waveform obtained using the FE model, depicting the first arrivals of the fundamental modes, with and without the use of absorbing layers (ALID).

The effectiveness of utilizing the ALID to dissipate the energy reflected from the edges of the model is demonstrated in Figure 3.10. In the case on the model without ALID, a reflection from edge of the cylinder is recorded prior to the arrival of the A_0 while for the second case this reflection disappears. In general, the introduction of damping tends to increase the computational time of the numerical integration although, the ability to suppress unwanted reflections distorting the helical modes outweighs the additional analysis time.

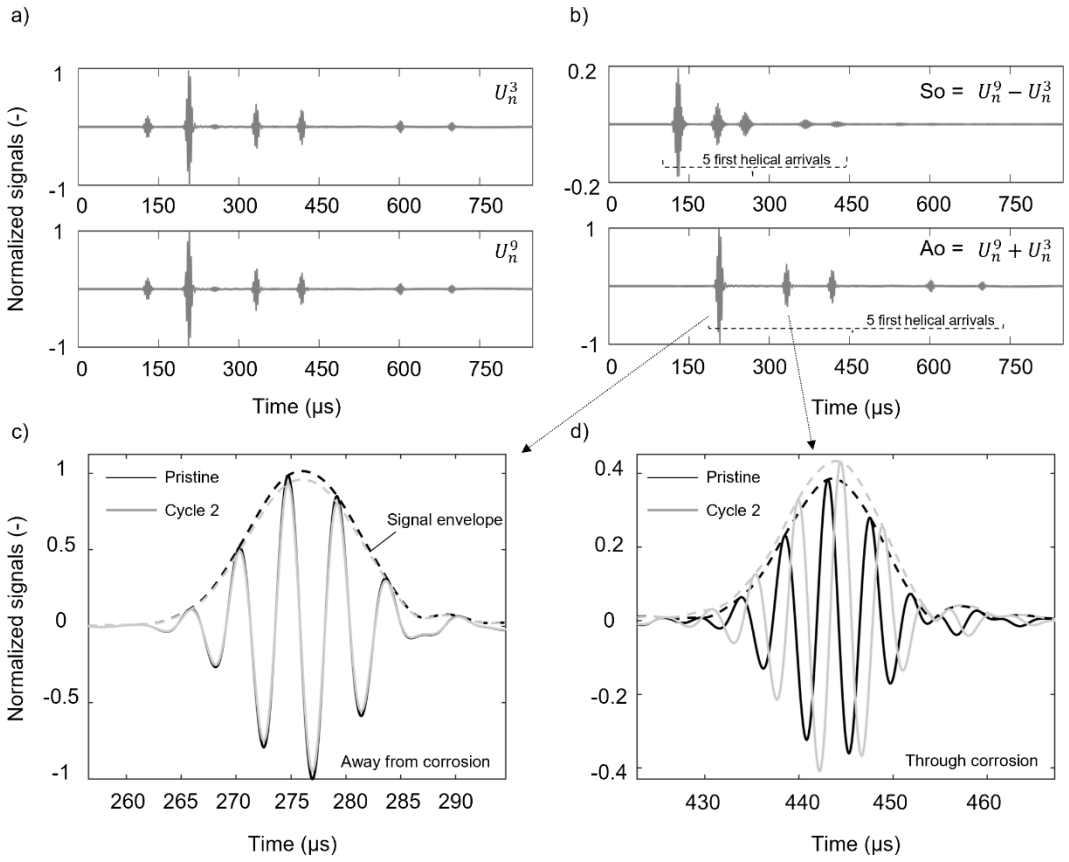

Figure 3.11: Extracting signals containing only symmetric S_0 and asymmetric A_0 modes from the numerical model. The signals recorded a) at the two free nodes, b) the isolated modes, c) first and d) second helical order A_o modes from isolated signal.

An example of the procedure followed to separate the fundamental modes in the numerical model is demonstrated in Figure 3.11, for excitation happening at node 1 (or PZT 1) and displacement being recorded at nodes 3 and 9 (see Figure 3.9). The normal to surface displacements are added and subtracted to yield signals containing only A_0 and S_0 respectively. The first two helical orders of the A_0 are shown for Figure 3.11 (c)(d) for the pristine state and simulated cycle 2 (~ 10% thickness loss). A simple comparison reveals that a given helical mode that does not intersect the simulated damage essentially remains the same, while for the other case, significant amplitude variation as well as phase shift is observed.

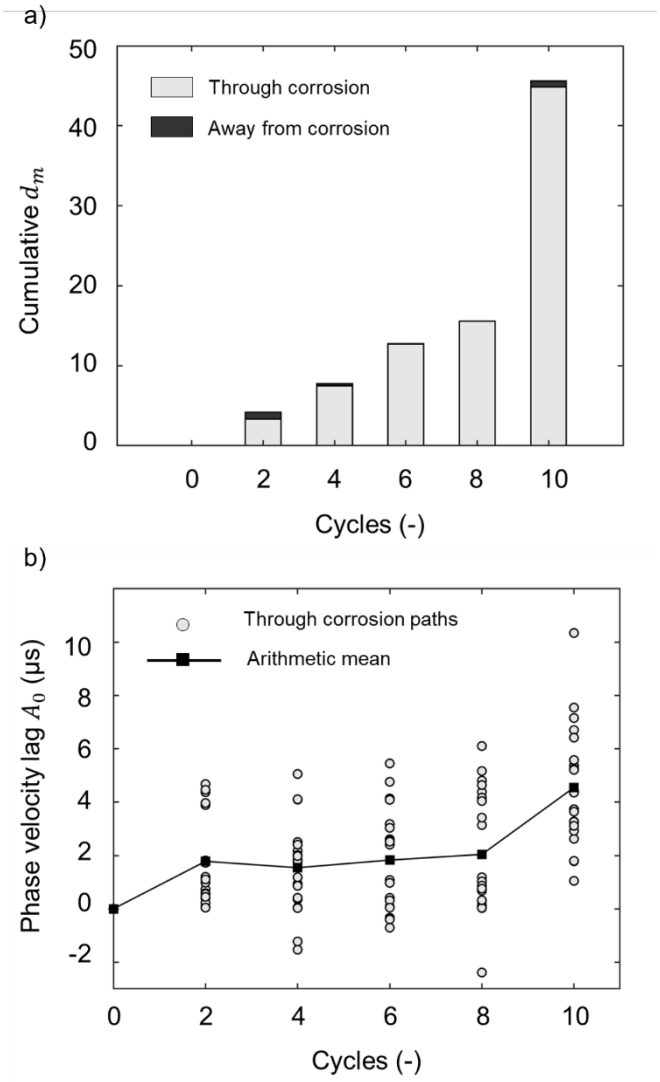

Figure 3.12: Sensitivity evaluation using the numerical model for a) the cumulative damage coefficient and b) the phase velocity lag of the A_0.

The sensitivity of the modal energy ratio and the travel time lag in numerical modeling for cycles 2,4,6,8,10 was estimated, and the results are illustrated in Figure 3.12. To evaluate the overall sensitivity of the energy ratio, the cumulative damage coefficient was defined as:

$$d_m = \sum_{1}^{N} d_{i-j,c}^{h} \tag{3.7}$$

which is simply the summation of the damage indices for the number of paths in each category (through and away from corrosion) N, for each state c of the simulated corrosion progress.

Figure 3.12(a) demonstrates that as corrosion progresses and the remaining thickness is smaller, the damage coefficient d and thus the energy ratio significantly grows for those helical paths that interfere with the corrosion. In contrast, for the same window, the fluctuation of the ratio of modes that propagate away from the damage, appears to be negligible. Such a high contrast in the damage coefficient is beneficial to the CL step since it improves the overall accuracy of the reconstructed localization image. Figure 3.12(b) illustrates the calculated phase velocity travel time lag, for the through corrosion paths. An increasing trend could be observed in the data meaning that the phase velocity is decreasing as the thickness reduces. This behavior agrees with the dispersion relations for the A_0 mode presented in Chapter 3**.** Some variability is also observed in the phase velocity estimations, which is primarily caused by those paths that have a minor interaction with the damage area and thus are less sensitive to the thickness variation. The phase velocity lag of the S_0 mode was estimated as well and it was found to be an order of magnitude smaller of the corresponding A_0 verifying again that in the fd region of interest, the latter contains much more information regarding the remaining thickness and thus better suited to be used in *CS*.

3.5. Energy of the S_0 & A_0 when excited in a wall-thinning

The effect of corrosion on the energy of helically propagating AE events was first investigated using a finite-element (FE) model developed in ABAQUS. The model was linear elastic with a modulus of elasticity, density, and Poisson's ratio equal to 210 MPa, 7850 kg/m^3, and 0.3 respectively. Time-domain explicit integration was used to solve the wave equation using ABAQUS-explicit. For modeling purposes, corrosion was approximated as a wall-thickness loss having approximate dimensions 20 cm in the longitudinal direction and 10 cm in the hoop direction, as shown in Figure 3.13. A variety of approaches exist that allow the excitation of Lamb-type waves in FE models, including longitudinal or shear dipoles for simulating cracks or distribution of nodal forces that excite either symmetric or anti-symmetric modes[47]. For simplicity, a point force in the longitudinal direction was used as the excitation at the center point of the assumed corroded area which is a common approach for exciting Lamb waves. This force was a short 3.5 Hanning-windowed toneburst, applied at the top node of the thickness of the pipe.

Two different central frequencies were considered, 60 kHz and 160 kHz which have been chosen according to experimental observations of the dominant peak frequencies during the accelerated corrosion test. The dimensions of the model were the same as the test specimen, although half the length was modeled due to the anti-symmetric positioning of the sensor pairs 1&6, 2&5, and 3&4. At the corresponding locations of sensors 1-3 (refer to as nodes 1-3), the displacement normal to the surface was recorded, since this is the component of displacement that is being sensed by the receiving sensors in real applications. To avoid reflections from the two edges of the model, 10 cm wide absorbing layers with increased damping (ALID) were added to the model according to [45]. The temporal and spatial resolution of the wave propagation was maintained by properly choosing the minimum integration time step and the maximum finite-element size according to guidelines reported in previous studies [36]. A total of nine analyses have been considered, including the damage-free pipe and steps of 10% thickness loss up to 80%. The duration of each analysis was set at 1.5 ms which approximately allowed 10 helical orders to propagate at each recording node.

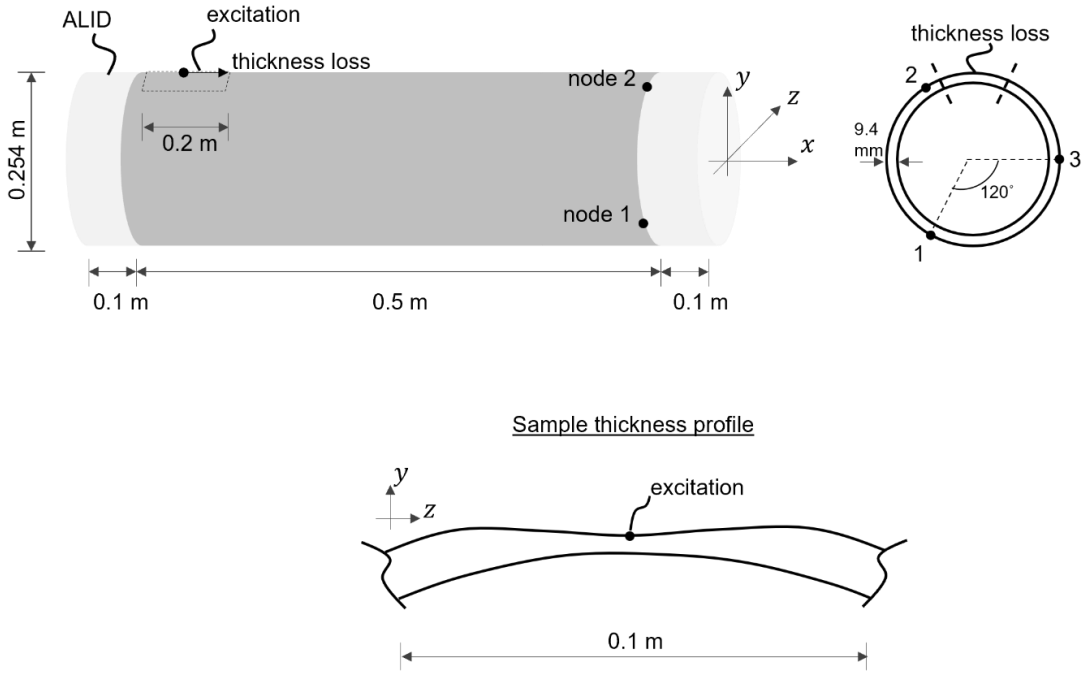

Figure 3.13: Schematic of the numerical model developed in ABAQUS. Nine different models have been considered with thickness-loss profiles from 0-80%.

Figure 3.14(a) shows the time domain radial displacement waveforms obtained at node 2 for a thickness loss of 0% and 80%, respectively. The multiple arrivals of the helical paths can be observed, as well as the dominance in amplitude of the A_0 in the radial direction. The geometric attenuation of the helical waves can also be noticed affecting primarily the higher orders of helical paths although significant energy can propagate even after 1.5 ms from the excitation. This highlights the importance of adjusting the timing parameters when recording HGW-type AE to avoid misclassification or omittance of these late arrivals. A close comparison of the first arrivals reveals that the amplitude and consequently the energy is significantly larger when the thickness loss is higher. One of the reasons causing this energy increase is the fact that the simulated excitation burst is occurring at a significantly thinner portion of the pipe in which Lamb waves have smaller attenuation. Considering that the end of the wall thinning is smooth, it is reasonable to assume that scattering is negligible. Thus, the propagating helical mode is shifting its group velocity based on a larger fd product according to the dispersion relationships, only this time carrying more energy. For the time that the wave was propagating in the wall thinning (1.9 mm) at a frequency of 160 kHz, its theoretical A_0 speed according to the dispersion relationships was 2575 m/s as compared to 3200 m/s for the remaining portion of the pipe. This delay in the time-of-flight can also be noted in Figure 3.14(a).

The energy of each recorded signal $S_{fem}(t)$ for every model was estimated by means of the root-mean square (RMS) according to

$$\mathrm{E_{fem}} = \sqrt{\frac{1}{N}\sum_{i=1}^{N}(s_{fem})\text{^}2} \tag{3.8}$$

where N is the length of the signal. The energy increase is demonstrated in Figure 3.14(b) showing the percentage difference of the RMS energy for excitations 60 kHz and 160 kHz at the three recording nodes. The propagated RMS energy of the simulated HGW-type AE source increases proportionally with the simulated thickness loss at all three nodes. This increase is not uniform between the nodes since their relative position to the simulated excitation affects the arrival of the helically propagated energy. Components of this energy can interfere constructively or destructively before reaching the sensor which might be the reason for observing energy loss in

the signal of node 1 for thickness loss between 30%-50%. Despite that, the RMS energy experiences a sudden increase between 50%-60% thickness loss and eventually doubles for all nodes for thickness loss of around 70%.

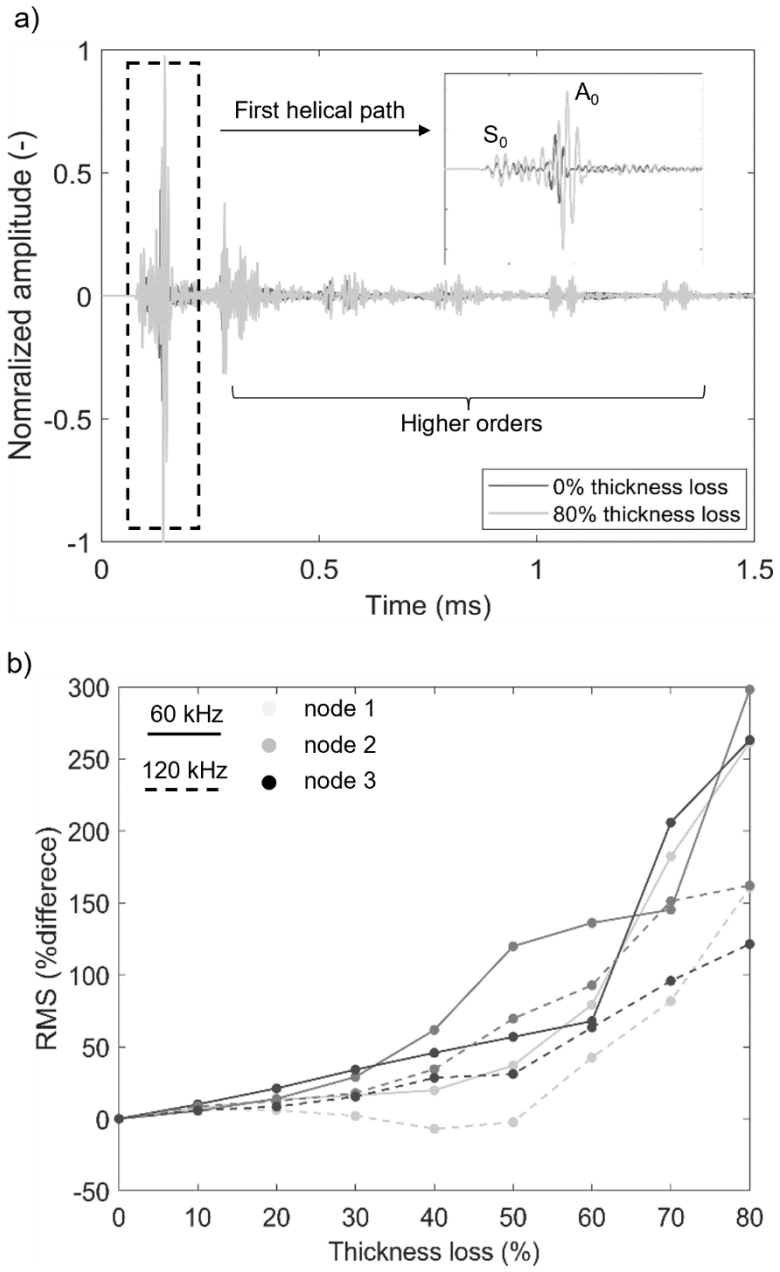

Figure 3.14: Time-domain waveforms from a pristine and the 80% thickness loss models of the pipe. Excitation happens in the simulated damage region and is recorded at node 2.

3.6. Summary

This chapter presented the framework for modeling the HGUW using the finite element method. It was reported that for accurate simulations special refinement of the mesh and the integration step is required which is defined by the operational frequency. A point force was utilized to excite the fundamental Lamb modes, due to the ease of modeling and accuracy in the excitation of the modes. Through four different models, the scattering of the fundamental modes was investigated by means of measuring either the amplitude or the ratio of the amplitudes of the multiple helical orders of the S_0 and A_0. The first three models considered through transmission propagation while the fourth model considered the HGUW to initiate at a local wall-thinning of the pipe.

Overall, the anti-symmetric A_0 was found to be extremely sensitive for all the different defect sizes that were considered. Due to having dominant normal-to-surface displacement component it was easier to monitor relative changes in the propagating energy. The amplitude variation of the baseline subtracted A_0 mode was used as the damage coefficient for the CL algorithm, and successfully localized the simulated damage in the first two models. In the case of a larger damage, like the third model, the ratio of the fundamental modes was found to be more accurate.

For the last simulation, which refers to the HGUW being generated during AE, a strong correlation was found between the RMS energy of helically propagating waves and the current thickness of the pipe. In particular, the rate that the energy increases changes when the remaining thickness is approximately 53% which can be used as the first indication of severe corrosion happening in the pipe.

4. Acoustic Emission monitoring using HGUW

Contrary to active guided ultrasonic testing, the acoustic emission (AE) depends on passively monitoring the acoustic activity in a structure without the need for providing an excitation. In theory, the state of stress in a structure variate during initiation and growth of defects like cracks and corrosion. This stress change is associated with the sudden release of mechanical energy whose intensity correlates with severity of the defect. Arrays of AE microphones are responsible to collect this activity and attempt to localize and assess the remnant capacity of the structure. The acoustic emission (AE) technique is an established NDE method and has been widely used for monitoring corrosion in pipes, tanks, and vessels [13], [14], [48]

In hit-driven AE, a threshold is commonly established based on the noise floor level, and whenever an acoustic event crosses that threshold, it is recorded as an AE hit. Several features can be extracted from the recorded waveforms including the energy, amplitude, and frequency content which are rich in information about the structure's integrity. For example, Jirarungsatian et al. [49] reported that by using the frequency and duration of recorded AE signals, is possible to identify and distinguish pitting and uniform corrosion. Jomdecha et al.[50] were able to correlate common AE features such as the count and amplitude to four different types of corrosion: uniform, pitting, crevice, and stress corrosion cracking. Li et al. [51] reported the identification of the different sources of AE during the corrosion of stainless steel. They applied a K-means clustering algorithm to AE features, such as count, duration, rise time, and amplitude, for distinguishing the pitting process from bubble break-up and cracking. Other studies investigated the attenuation of AE events in buried pipes caused by different types of soil as well as different types of transported fluids [52].

In thin-walled metallic structures, AE is typically associated with the propagation of Lamb-type guided waves. Due to the dispersive nature of these waves it is possible to correlate the frequency content of AE events with the depth of a crack in plate-like structures [53]. Another Lamb-wave-based AE approach was also used for assessing corrosion in the bottom plates of large tank reservoirs by using the time-of-flight of the fundamental Lamb modes [54]. Finite-element investigations were reported on the influence of wave propagation distance on AE features proposing various correction factors that can be introduced in post-processing [55]. AE has also

been used extensively for monitoring different failure modes of concrete structures[56] . Studies have demonstrated a strong correlation of AE features with micro-crack formation and growth [57] while others have used a topological analysis of AE features to monitor the corrosion process in prestressed concrete [58].

In this study, a new approach to monitor corrosion in steel pipes is presented using Lamb-type acoustic emission events propagating helically in the circumference of the pipe known as helical guided waves (HGW)[18]. Traditionally, the AE method is used in pipes and vessels by monitoring the absolute number of recorded events while the source and type of the received perturbation are typically ignored. The proposed approach is based on considering longer portions of each AE event and utilizes typical AE features like the energy and amplitude to infer the state of corrosion in the pipe. Specifically, the energy associated with a single AE event is considered to travel in helical trajectories around the pipe's circumference before reaching the receiving sensors thus longer than the typical time window is necessary to fully capture it. This is achieved by carefully selecting the AE timing parameters such as the hit-definition time (HDT) and the hit-lockout time (HLT) of the AE acquisition system. Through experimental and numerical testing, it has been shown that the energy of HGW is increasing as corrosion becomes more severe which can serve as an indicator of the current structural condition of the pipe. Furthermore, a b-value analysis has been applied to the AE data showing a strong correlation between the amplitude of the AE hits and the stage of corrosion

4.1. Corrosion assessment

4.1.1. Helical Lamb-type Acoustic Emission

Let's consider a steel pipe instrumented with a sensor and an AE source occurring at a random location on its surface as illustrated in Figure 4.1(a). Provided that the pipe's diameter is much larger than its thickness [59], these circumferential waves can be considered similar to Lamb waves in plates by replacing the cylinder with an equivalent unwrapped 2-dimensional (2D) plate [60]. Using the 2D representation, the previously helical trajectories can now be thought as a single AE source detected by multiple virtual sensors by straight paths according to Figure 4.1(b).

Theoretically, the number of the so-called helical paths can be infinite although in practical applications due to attenuation only a finite number can be considered. For an AE source located at (x_{AE}, y'_{AE}) to the i[th] sensor located at (x_i, y'_i), the length l_i^h of each helical path h can be calculated as:

$$l_i^h = \left((x_i - x_{AE})^2 + \left((n\pi D + y'_i) - y'_{AE}\right)^2\right)^{0.5} \qquad (4.1)$$
$$n_h = 0,1,-1,2,-2,\ldots,\infty$$

where D is the pipe diameter. Thus, the time-of-flight can be calculated according to:

$$t_i^h = \frac{l_i^h}{C} \qquad (4.2)$$

where C is the wave velocity. The velocity C is a function of the frequency and thickness (fd) of the pipe and can be estimated using the Lamb waves dispersion curves according to Figure 4.2.

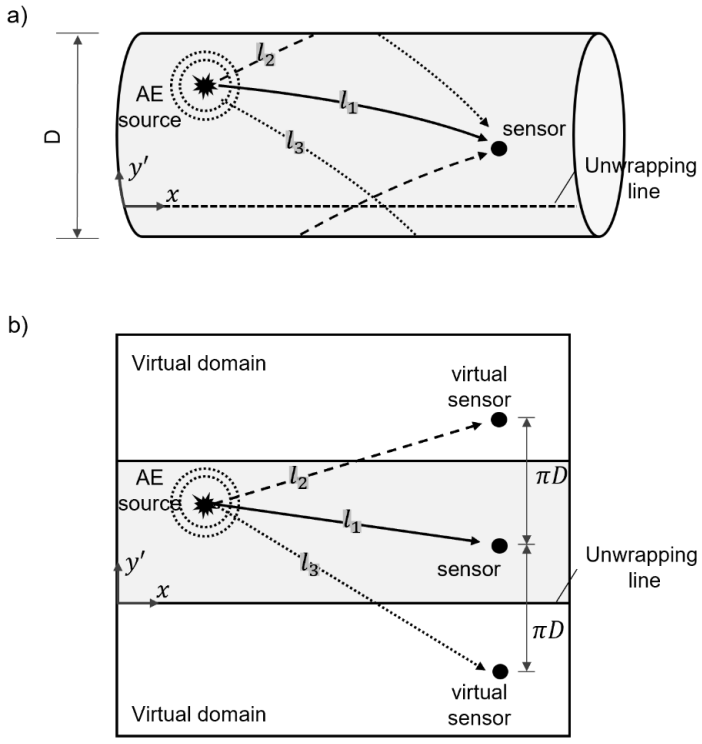

Figure 4.1: The first three helical paths from an AE source to the sensor. An illustration of the concept in a) 3D and b) the unwrapped 2D.

For AE sources with small profiles, like the microcracking, the velocity can be considered constant since the wave propagates in an almost similar thickness. However, if the AE originates within a large corrosion patch on the pipe's surface, a change in velocity is anticipated. According to experimental studies, the frequency of corrosion-related AE events in steel is normally lower than 200 kHz [49]. Given this frequency and a pipe thickness around 10 mm the maximum frequency-thickness product is near fd = 2 MHz-mm, at which the fundamental Lamb modes S_0 and A_0 are dominant with the first couple helical paths carrying most of the energy. Considering now a relatively large corrosion patch on the surface of the pipe according to Figure 4.3(a), it is reasonable to assume that a generated wave will travel through at least two different thicknesses before reaching the receiving sensor. For instance, the first two helical orders will propagate different lengths of the wall-thinning, R_1, R_2, with velocities $C_{(fd)_0}$ and $C_{(fd)_c}$ corresponding to the pristine and corroded parts of the pipe. Thus, their corresponding time-of-flights can be written as

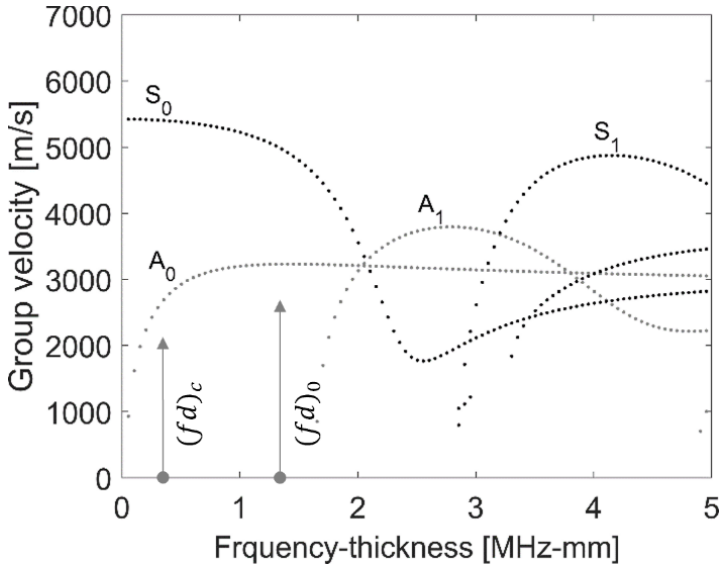

Figure 4.2: a) The dispersion relationship of the group-velocity of Lamb waves against the frequency-thickness product (fd). b) An AE event traveling in different thickness profiles before being recorded

$$t_i^1 = \frac{l_i^h - R_1}{C_{(fd)_0}} - \frac{R_1}{C_{(fd)_c}}$$

$$t_i^2 = \frac{l_i^h - R_2}{C_{(fd)_0}} - \frac{R_2}{C_{(fd)_c}} \tag{4.3}$$

and their difference in arrival time $\delta t_i^{21} = t_i^2 - t_i^1$. Depending on the extent of the wall-thinning, the location of the AE source and the remaining thickness, δt_i can vary significantly. A large δt_i essentially means that the possibility of consecutive helical paths from the same AE source to be recorded as multiple events is greater. For example, the time interval δt^{41} is calculated for a sensor with helical paths $l^1 = 0.4$ m and $l^4 = 1.4$ m considering the velocity of the antisymmetric A_0 and different values for R_1, R_2. According to Figure 4.3(b), it is possible that the time window required to capture all four helical paths can range from 350 μs to more than 650 μs. This interval becomes even greater when more helical paths are considered or when the extent of the wall-thinning is larger.

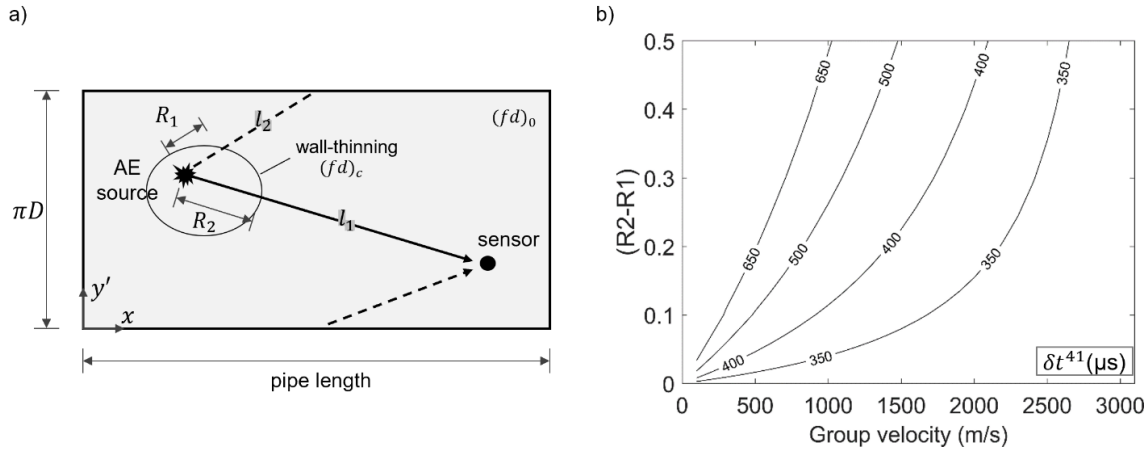

Figure 4.3: a) The difference in time-of-flight δt_i for the same pair of helical paths fluctuates depending on the values R_1, R_2 and the amount of wall-thinning of the pipe. b) The contour plot demonstrates an example of the estimated δt_i for a sensor with helical-path lengths $l^1 = 0.4$ m and $l^4 = 1.4$ m for different values R_1, R_2 and velocity

Based on the work demonstrated in previous chapters, different features of the helical waves such as the energy and attenuation, are associated with the state of corrosion in pipes [11]. Considering these remarks, it is important to collect as many helical paths as possible of a single

AE source in a single hit. With this aim, the timing parameters such as, Peak-Definition Time (PDT), Hit-Definition time (HDT), and Hit-Lockout time (HLT), should be properly defined as shown in Figure 4.4.

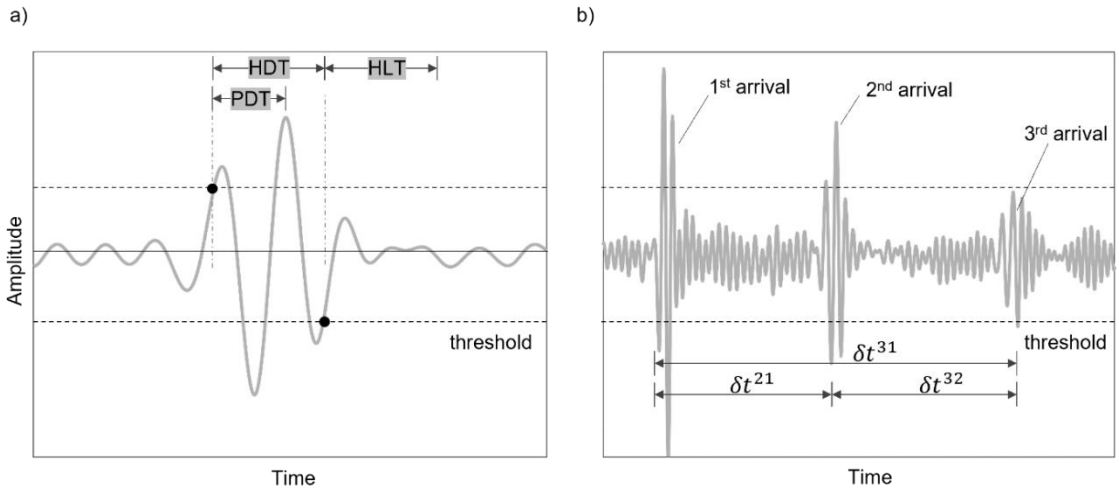

Figure 4.4: a) Demonstration of the timing parameters in hit-driven AE including the peak-definition time (PDT), hit-definition time (HDT), and hit-lockout time (HLT) that define the length of an AE hit. b) The combination of these parameters should allow for the assumed maximum number of helical paths to be recorded as a single AE hit.

When a threshold is recorded, the PDT controls the time between the first threshold crossing and the maximum amplitude while the HDT controls the time between the first and the last threshold crossings. The HLT defines the time to elapse before a new hit is recorded measured from the last threshold crossing. Among the three timing parameters, HDT and HLT have the major impact on the recorded AE hit. Figure 4.4 (b) demonstrates the effects of properly choosing the timing parameters using a synthetic waveform showing the arrival of three helical paths. If HDT is smaller than δt^{31}, the recorded hit will be terminated prior to the third helical path and a new hit will be recorded instead. Also, if the HDT is around δt^{21} and HLT larger than δt^{32} the third helical path will be omitted. One approach to estimating the HDT and HLT is to use Eq.(4.5) assuming typical values for the parameters R_1, R_2 and a specific number of helical paths to obtain a plot similar to Figure 4.3. Studies from the authors have suggested the consideration of at least 5 helical paths for sensors less than 1 m away from the corrosion [61]. Alternatively, an experimental approach may be used to determine these parameters. Pencil lead break (PLB) [62]

is a standardized method to simulate AE events which can easily be carried out at any location of interest on the pipe. By trial and error, a combination of values for HDT and HLT may be decided such that for each PLB on the pipe's surface a single hit is recorded. In practice, the presence of discontinuities like the pipe supports, welds or the end edges will cause the estimated HLT to increase due to reverberating energy.

4.1.2. b-value analysis

The qualitative assessment of corrosion is carried out using b-value analysis [63], [64]. It has been established in earthquake seismology that the frequency of occurrence of seismic events and the corresponding magnitude are directly related. This relationship is mathematically represented by the Gutenberg-Richter empirical equation

$$\log_{10} N = \alpha - \mathrm{b}(M) \tag{4.4}$$

where M is the Richter magnitude, N is the incremental frequency of seismic events (i.e., the number of events greater than M), α a constant and b the slope of the line corresponding to the b-value. This equation is relying on the observation that seismic events with lower intensity occur more frequently compared to those events with higher intensity. It has been reported that Eq.(4.4) can be effectively adapted in AE applications if the recorded AE amplitude is divided by a factor of 20 to compensate for the difference in measuring units, this being Richter for earthquakes and dB for AE events [65]. Thus, the Gutenberg-Richter equation takes the following form,

$$\log_{10} N = \alpha - \mathrm{b}(A_{dB}/20) \tag{4.5}$$

The process to calculate the b-value is outlined in Figure 4.5. First, the log-linear relationship between the AE events frequency and amplitude is constructed where the negative slope of this curve corresponds to the b-value. The resolution of the amplitude-axis depends on the AE DAQ which is often around 1 dB. At low and high amplitudes, the frequency of AE activity is disproportionate compared to the rest of the spectrum causing the curve to deviate from linearity. Thus, a linear fit is performed in the "linear descending branch" [65], which for this work corresponded to amplitudes approximately between 40-60 dB. These calculations are performed

based on groups of data n whose size is determined according to the total available hits and the frequency at which the b-value is desired. When n is large, it can reduce the frequency at which the b-value can be calculated. On the contrary, when n is small, the amplitude variance of hits is small which leads to an inaccurate b-value. In concrete applications with significant AE activity, this number can be around 100 events while in other instances with moderate AE activity this number usually is higher. Overall, the b-value is expected to be large during the initial stages of material deterioration where the amplitude of the AE data is usually lower [57]. As the corrosion becomes more severe, it is anticipated that the b-value will decrease eventually approaching values close to one [66].

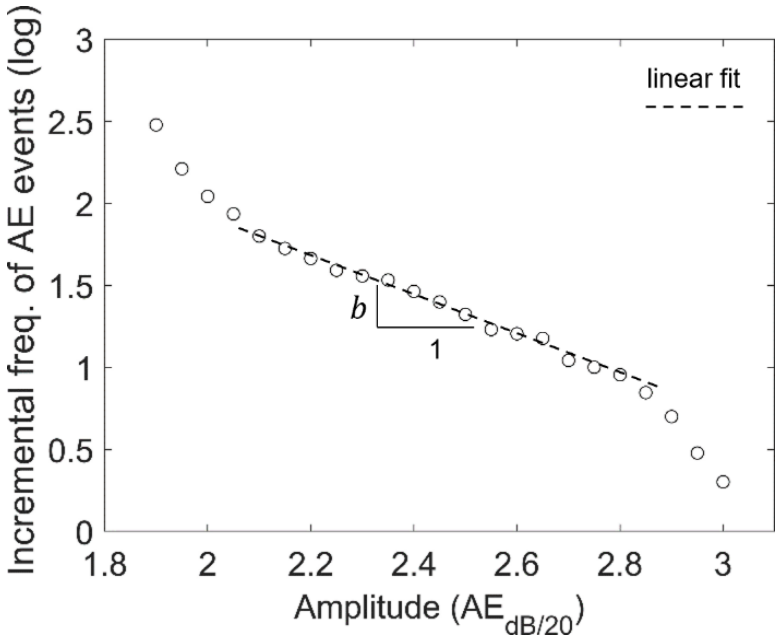

Figure 4.5: The log-linear AE frequency-magnitude plot. The negative slope of this curve corresponds to the b-value.

4.1.3. Machine Learning - Variational Auto Encoders

Variational autoencoder is selected due to its un-supervised nature (labels are never seen by model) and visualizable latent space. The parameters that the model has learned are summarized into 2D latent space which makes the result reviewable instead of reply solely on the testing set accuracy. The modeling is pipelined into three parts: feature extraction, variational autoencoder separation, and classification with data fed in. For the purposes of exploring variational

autoencoder, the other two parts will just be classical convolutional neural nets. Current approach is to compress a hit into 256 features then get fed to variational autoencoder for latent space modeling, the features has been normalized into [0,1] in order to apply binary cross entry to calculate expectation of log likelihood. The architect of the model itself is also convolutional neuron nets.

This study has modified the optimization target from normal distribution to mixture normal distribution aiming on making the model capture more information from one acoustic emission hit. The performance was evaluated through model evidence (mixture normal distributions, orange curves in Figure 4.6 over hits, which appears to follow the trend of distributions of wave forms with log-likelihood of around 1,000. The latent space plot (Figure 4.6) indicates the separation among hits that follows the distinction of each corrosion cycle in which the corrosion cycles relate to steel thickness reduction from the inference of constant corrosion rate.

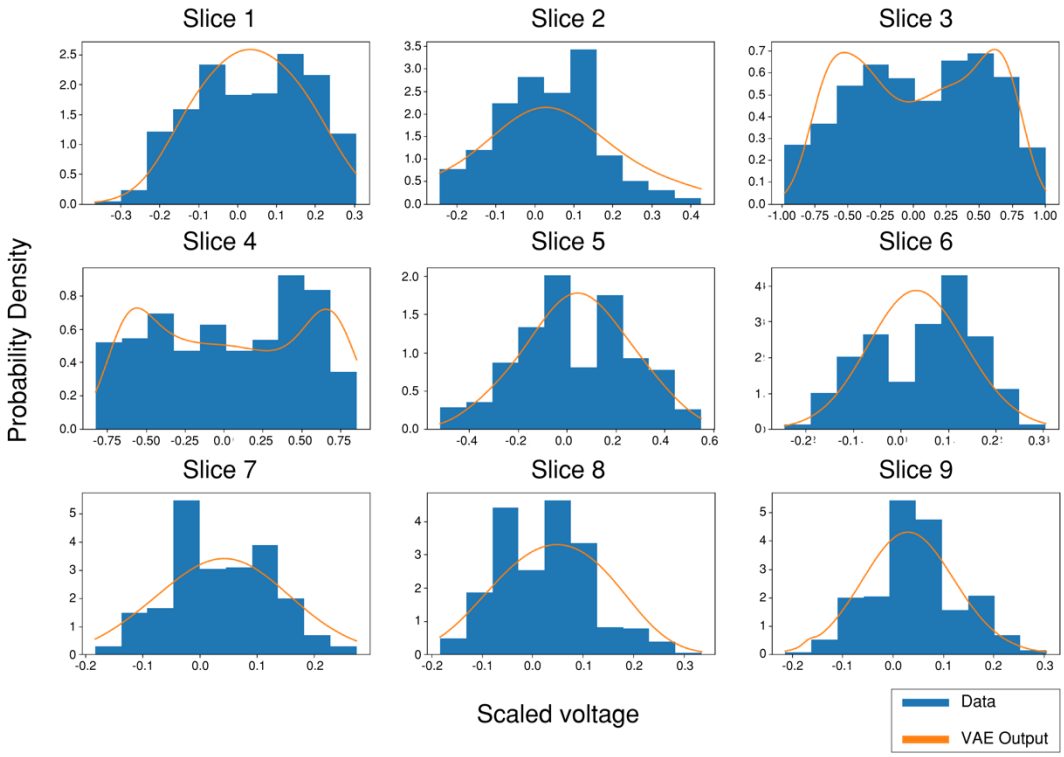

Figure 4.6: Model evidence result

One step further, given the model is picking mostly energy information from waveforms, the normalized energy was calculated to rationalize for such behavior. Normalization of energy is calculated through energy generated per microsecond. The normalized energy with inferred steel thickness reduction plot suggests that the difference may follow a spike of energy at the start of each corrosion cycle. The latent space of VAE provides support for distinction of AE hits generated from different remaining steel thickness that may correspond to spikes of energy in AE hits during corrosion cycles. The model can map AE hits to latent space that links to ranges (0.27mm increment) of remaining steel thickness. Future work involves expanding the work to the rest of the cycles in the dataset and generalizing their results.

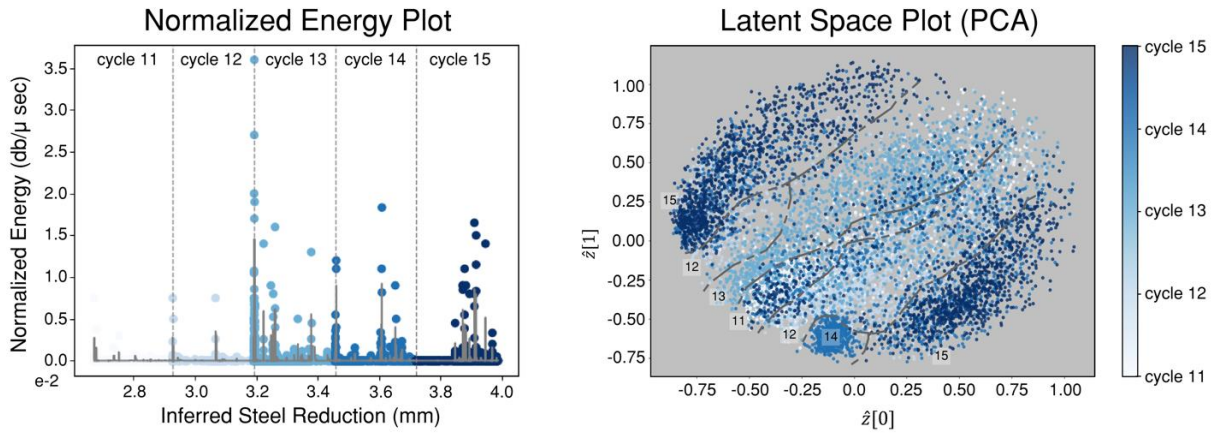

Figure 4.7: Latent Space Result

4.2. Experimental validation

4.2.1. Accelerated corrosion

An accelerated corrosion test was carried out using the impressed current technique [67]. The test specimen was a schedule 40 steel pipe with diameter equal to 0.25 m (10 in.) as shown in Figure 4.8. The pipe was 1.5 m (5 ft.) in length, 9.4 mm (0.37 in.) thick, and was supported at the two ends by two steel tripods. A rectangular plexiglass tank (0.2 m × 0.1 m) was attached to the center of the pipe using epoxy adhesive and sealed around with silicon to prevent any leakage. A power supply equipped with built-in ammeter and potentiometer was used to impress a direct

current (DC) to the pipe to induce significant corrosion in a short period of time. The direction of the current was adjusted so that the steel pipe served as the anode, while an iron wire mesh around the tank was used as the cathode. A 3% sodium chloride (NaCl) solution was used as electrolyte. Before the beginning of each cycle, the water tank was emptied, and fresh distilled water was added.

A constant current of 4A was provided through the power supply which corresponded to a potential ranging between 3-5V. The test comprised of a 5-hour continuous current supply, and it was repeated for a total of 34 cycles. Failure of the pipe occurred during the 35th cycle. Using Faraday's Law of electrolysis with the parameters of the test, it was estimated that the rate of thickness loss was approximately 0.25 mm/cycle which agrees with the actual failure of the pipe.

The pipe was instrumented with six R15a Physical Acoustics sensors which were bonded on the pipe's surface using hot glue. Sensors were placed 40 cm away from the center of the salt-water tank with the ones being at the same cross section having 120˚ angle difference and the 60˚ between the two cross-sections as shown in Figure 4.8. The threshold was set to 38dB. AE activity was continuously recorded with a Mistras Micro-II Express DAQ system. Signals were preamplified by 40 dB using 2/4/6 PAC preamplifiers and filtered using a 5 kHz – 1MHz bandpass filter.

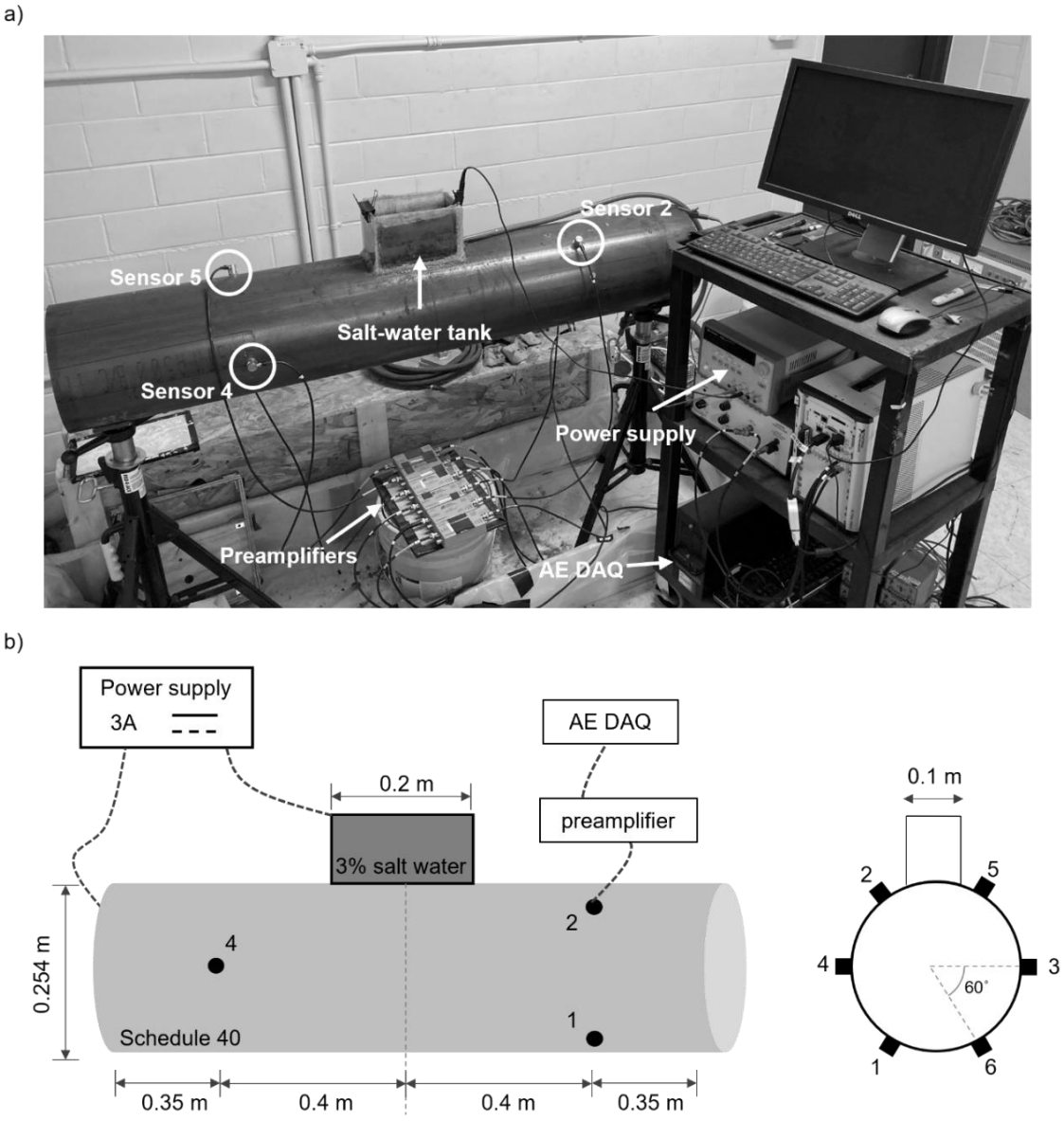

Figure 4.8: a) An overview of the experimental setup and b) a schematic of the experiment with details regarding the sensor placement along with various dimensions

4.2.2. Data Acquisition Parameters

According to the discussion in Section 4.1, the selection of data acquisition parameters of the AE activity is crucial for the effectiveness of the proposed methodology. The selected values are presented in Table 4.1. The calculation of HDT was based on considering five helical paths between the farthest sensor (i.e. sensor 1 or sensor 6) from the centroid of the corrosion. The

maximum difference of travel time δt^{51} was calculated using the procedure outlined in Section 4.1 for different values of R_1, R_2 and velocity. It was found that a value of 500 μs was adequate to cover the different scenarios of an AE hit happening in random locations inside the corroding area. Regarding the Hit-Lockout time (HLT), the rule of thumb is to be set equal to HDT which was not the case in this experiment. Based on multiple PLBs in various locations of the pipe it was found that 30 ms was an adequate time window for the HGW to propagate. This value is significantly larger compared to a theoretical prediction for HLT due to reflections from the pipe's ends that kept significant energy reverberating in the structure. In more realistic scenarios where pipes are continuous, the experimental and analytical predictions of the HLT should converge.

Table 4.1: AE data acquisition parameters

PDT (μs)	300
HDT (μs)	500
HLT (ms)	30
Duration(ms)	2

4.3. Results

4.3.1. Triangulation

To validate the hypothesis that AE activity recorded during the experiment was related to the material degradation due to corrosion, source localization was first performed. The localization was performed using an optimization-based technique for isotropic plates with unknown was speed. triangulation [68]. If the unknown source location is (x_0, y_0) then the error function $E(x_0, y_0)$ is defined as:

$$\mathrm{E}(x_0, y_0) = \sum_{i=1}^{n-1} \sum_{j=i+1}^{n} \sum_{k=1}^{n-1} \sum_{l=k+1}^{n} \left[t_{ij}(d_k - d_l) - t_{kl}(d_i - d_j) \right]^2 \qquad (4.6)$$

with t_{ij} the time difference between the pair of sensors i, j, n the number of sensors, and d the Euclidean of (x_0, y_0) to each sensor. A standard minimization algorithm can be used to calculate the unknown coordinates of the AE source.

The outcome of the source localization is presented in Figure 4.9. It can be observed that, most of the events originated at the center or near the area where corrosion was taking place. Localizations of AE sources outside the corrosion area might be caused by noise, instabilities occurring from the localization technique or even reflecting waves from the pipe's edges.

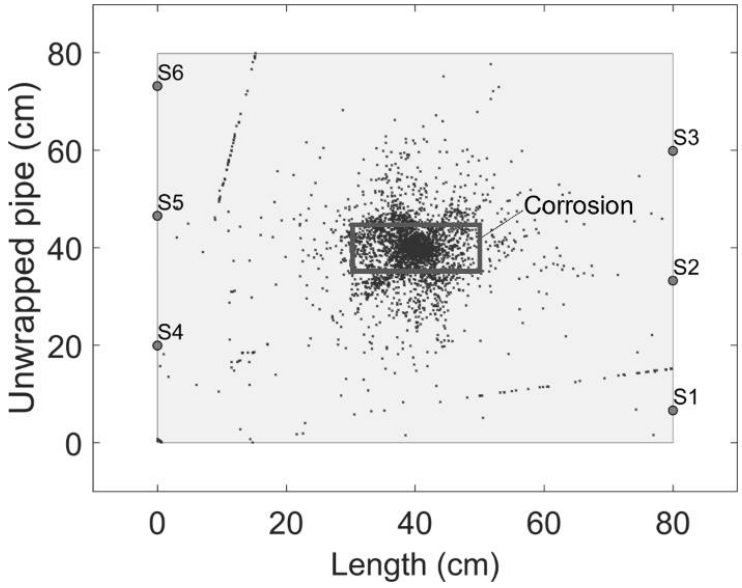

Figure 4.9: Source localization results for the accelerated corrosion experiment.

4.3.2. Time-frequency analysis

To examine the theoretical assumptions made for the helical propagation of corrosion-related AE events, signals from the experiment have been compared with pencil-lead-break signals. The comparison was carried out using a time-frequency analysis based on a continuous wavelet transform (CWT) [69], [70]. The CWT was performed on a signal $f(t)$ according to

$$\mathrm{CWT(s,b)} = \frac{1}{\sqrt{s}} \int_{-\infty}^{\infty} f(t) \Psi * \left(\frac{t-b}{s} \right) \mathrm{d}t \tag{4.7}$$

where s, b the dilatation and translation parameters of the complex conjugate Morlet mother wavelet $\Psi(t)$. Based on the output of the CWT, the arrival times of the helical Lamb modes could be extracted as well as the distribution of the energy between the helical paths could be estimated. PLB tests were carried out after the completion of the accelerated corrosion experiment. These tests were performed on the opposite side (bottom side of the pipe, see Figure 4.8(b)) of the water tank approximately at the center-point. Due to symmetry, waveforms were collected only at sensors 1-3.

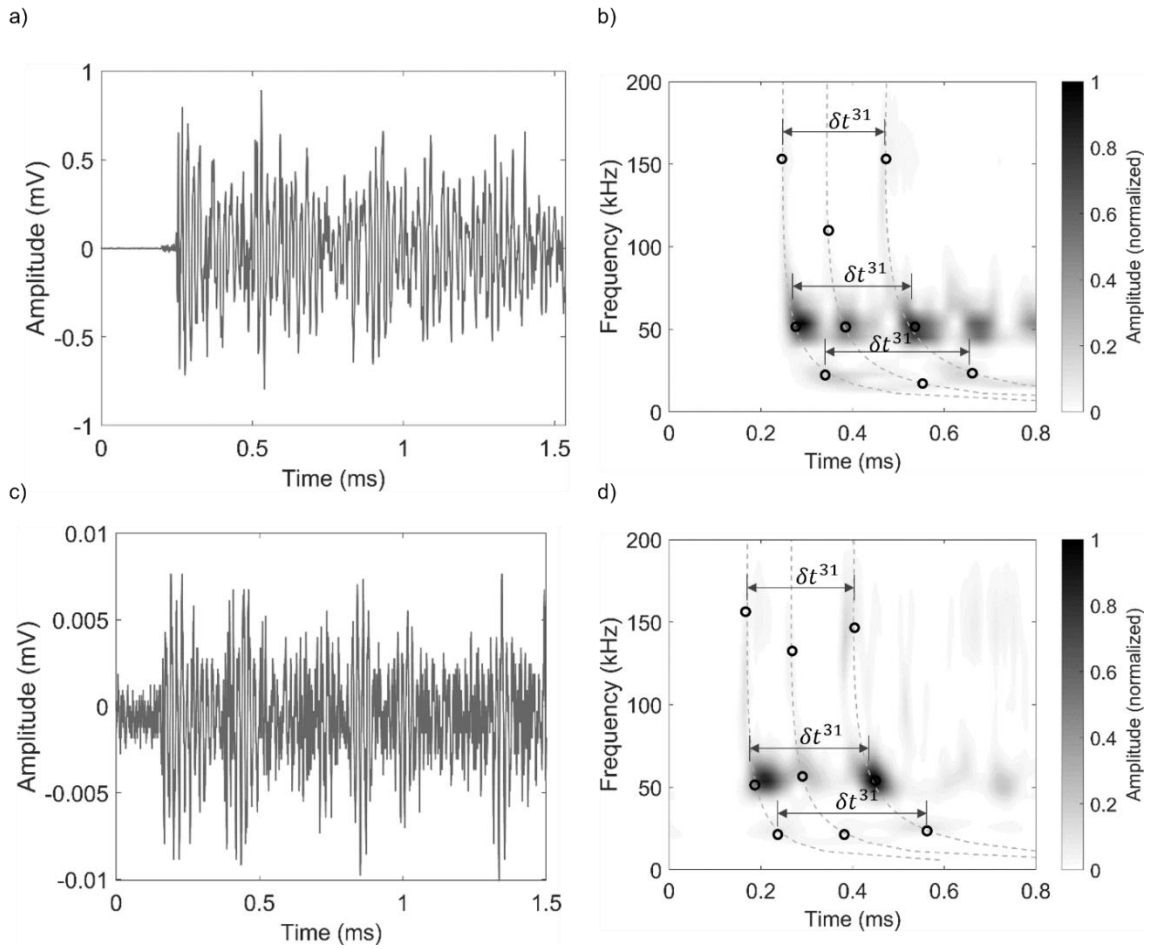

Figure 4.10: Time domain signals and continuous wavelet transform of pencil lead breaks and experiments. a) PLB signal, b) CWT of PLB signal, c) Experimental signal, d) CWT of Experimental signal.

Figure 4.10(a) and (c) show the PLB and experimental signal recorded by sensor 3 and Figure 4.10(b) and (d) show their respective wavelet transforms. In the frequency spectrum plots, the dispersion relationship of the group velocity of the fundamental A_0 mode is overlayed which is calculated for the specific thickness of the pipe. It can be observed that both the received signals contain frequencies below 200 kHz, and within this range the arrival of the energy agrees well with the theoretical dispersion relationship. The arrival of the first three helical paths is also noticed, each containing three distinct wavepackets with frequencies between 20-200 kHz. Furthermore, it is possible that the peak energy arrival occurs after the first helical arrival validating the initial assumption made about the HGW and the need for adjusting the timing parameters to incorporate these reverberations into a single AE hit. In this case, δt^{31} increases significantly at lower frequencies.

4.3.3. Energy and *b*-value analysis

The cumulative energy and amplitude of the AE data is demonstrated in Figure 4.11. The trend of the energy increase is approximately divided into two legs around the 53% loss. For the second leg, the AE hits have significantly more energy which is partly due to the breaking of corrosion products and partly due to the small remaining thickness that can sustain higher amplitude guided waves. A similar trend in terms of the point where the recorded energy starts to increase at a lager rate was observed in the numerical model. In practice, the identification of such a point can flag the existence of large corrosion in the pipes while the pipe has still significant thickness to operate until a repair is made. Regarding the cumulative amplitude, a sudden increase around the 30th hour of the experiment can be associated with the first significant loss of material from the pipe's surface. Prior to this point is possible that corrosion products have been accumulating on the surface without any major wall-thickness loss. Past this point, the cumulative amplitude of the AE hits follows an almost linear trend through the end of the test. In fact, it was anticipated to observe such a trend due to the cycles of accelerated corrosion being identical in terms of the current supply, saltwater solution, and duration. Although, the range in values of

amplitude in consecutive intervals was expected to shift depending on the severity of corrosion and thus the b-value analysis was carried out to aid this distinction.

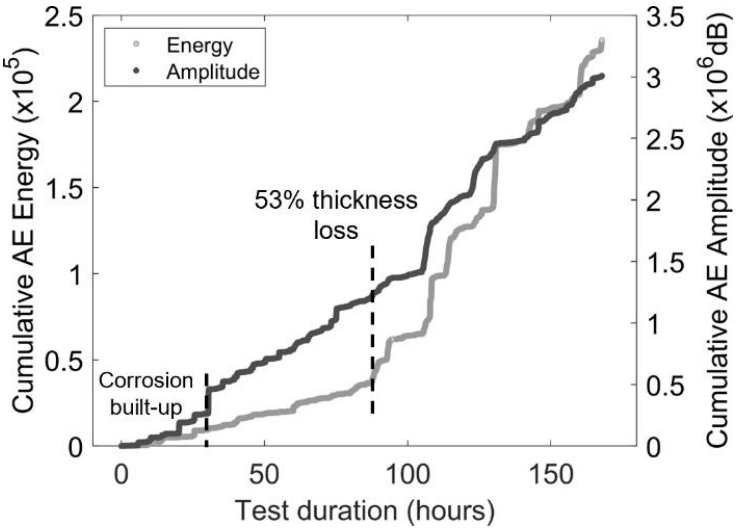

Figure 4.11: The cumulative Energy and Amplitude of the recorded AE data during the experiment.

Figure 4.12 demonstrates the calculated b-value for sensors 1-6 and the corresponding amplitude history for the duration of the corrosion experiment. Three different values of n were considered in solving Eq.(4.4) to examine its influence on the b-value. It was found that approximately 260-340 hits could result in a similar b-value for the duration of the experiment, as depicted in Figure 4.12, thus n = 300 was chosen. Furthermore, to increase the accuracy of the b-value it was found that a threshold of 53 dB could restrict the b-value from overshooting. For instance, if the maximum amplitude in a group of n hits was smaller than 53dB, the b-value calculation was omitted. This led to skipping portions of the test where the AE activity was low which can be seen mainly in the case of sensor 2.

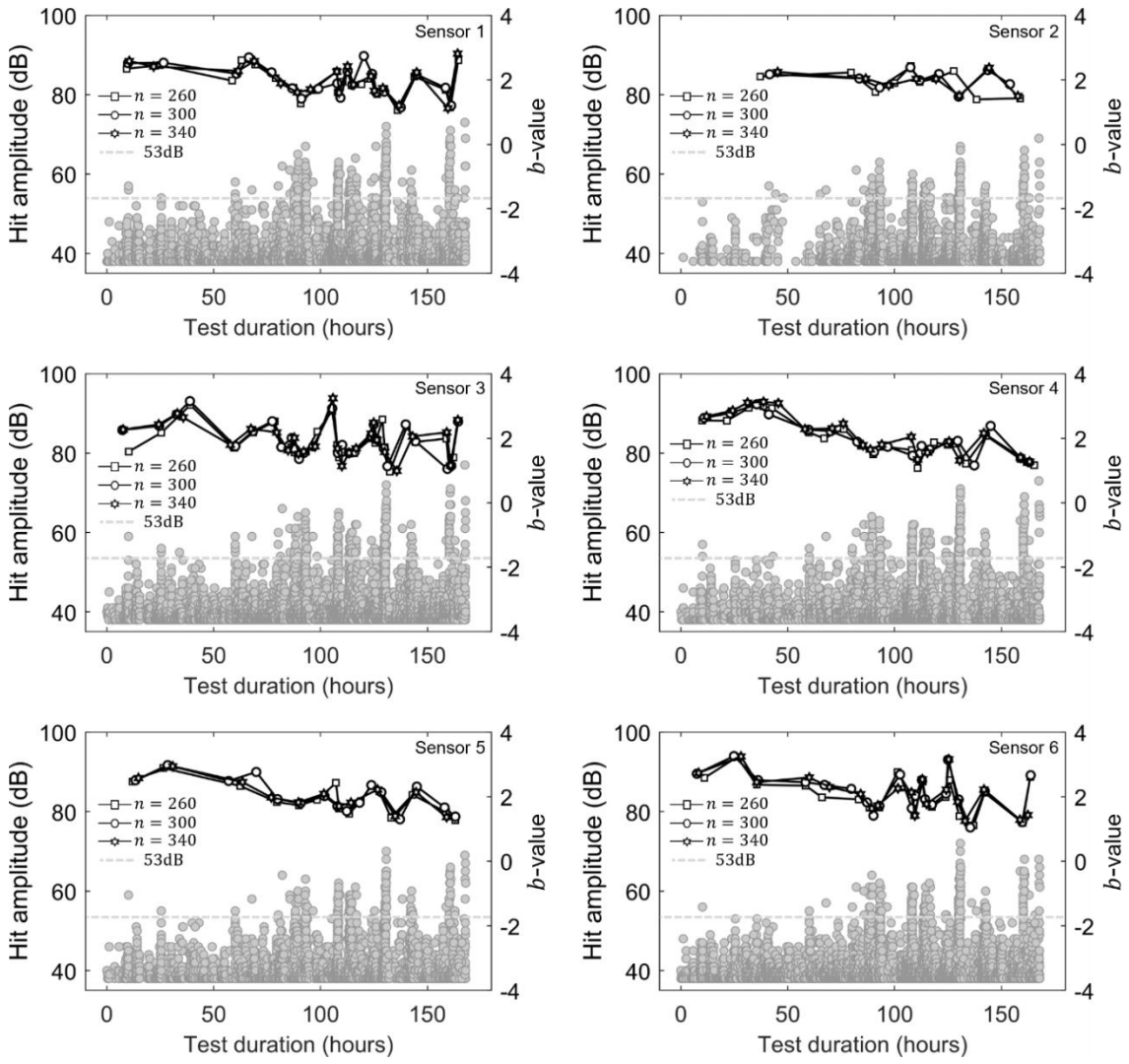

Figure 4.12: The cumulative Energy and Amplitude of the recorded AE data during the experiment.

Overall, the b-value trend appears to be similar across the sensors except for sensor 2. The estimated values, range from near 2.5 at first hours of the test to values close to 1.5 at later stages of the test. The largest b-values are observed between 30-50 hours in the corrosion test, denoting the initiation of the corrosion which agrees with the observation made from the cumulative amplitude plot. During this period, the maximum amplitude of the AE hits is smaller than 60 dB. Past this point, the amplitude of the hits becomes significantly larger forcing the b-value to become smaller. In terms of sensor 2, the estimated b-value is not comparable to the rest of the sensors.

This can be attributed to a less sensitive sensor or poor contact with the pipe's surface which is also verified by inspecting the relatively sparse hit amplitude history.

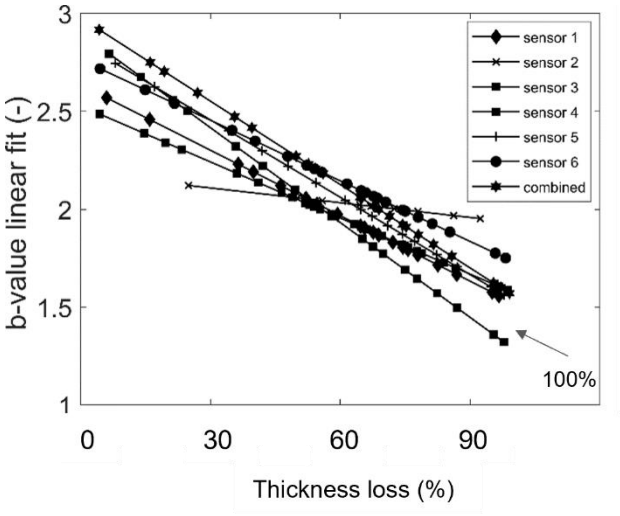

Figure 4.13: Linear fit of b-values for all sensors individually and combined.

To qualitatively compare the b-value trend across the sensors, a basic linear fit has been performed using the least-squares method. In addition, the b-value was calculated on the combined AE hits. The linear fit of the b-value is presented in Figure 4.13. These results highlight two important findings. First, an overall similarity in the slope of the b-value is observed, with the main outlier being sensor 2. It is noteworthy that four of these lines intersect that at the failure of the pipe for a b-value near 1.6. Using the b-value fitted lines, is possible to assess the corrosion rate which in this case is similar for all sensors. Also, it is possible to create an envelope of b-values corresponding to different types of corrosion. The second finding reveals the ability to use the same methodology for calculating the b-value on individual or combined sensor AE hits working as a type of filter for sensors or instances of low-amplitude AE history.

4.4. Summary

The use of the acoustic emission of Lamb-type helical waves for monitoring corrosion in steel pipes has been investigated in this work. It has been demonstrated through numerical investigations and an experimental test, that the use of this type of wave has the potential to

qualitatively assess the corrosion progress. Specifically, it has been highlighted that for the effective measurement of the HGW, hit-driven AE data acquisition parameters like the HLT must be increased such that for every event occurring from the corrosion progress, a single AE hit is recorded. Two metrics have been also introduced based on which the state of corrosion is estimated. First, it has been demonstrated that the energy of the AE events increases as the corrosion becomes more severe in the pipe. In particular, the rate that energy increases changes when the remaining thickness is approximately 53% which was observed both numerically and experimentally. Second, the b-value analysis has also been performed on the recorded AE data. It has been found that the material degradation due to corrosion can be described by a linear trend of b-values estimated for every 300 AE hits. The estimated b-value was near 2.5 at the initiation of corrosion and near 1 when the corrosion penetrated through the pipe wall. Several assumptions have been made in this work including that each AE event is isolated in time from the previous and consequent in addition to the pipe sustaining no liquid nor being pressurized. Future work should examine scenarios of liquid-filled pipes experiencing corrosion to verify the efficacy of the proposed methodology.

5. Conclusion

5.1. Contributions and remarks

This report demonstrated the use of helical guided ultrasonic waves for monitoring the structural integrity of steel pipelines. Specifically, it was reported that the HGUW can be exploited for both active and passive monitoring, to localize, quantify and predict corrosion in pipes. The use of the HGUW can potentially offer a shift in paradigm which can accommodate both real-time monitoring and in-situ routine inspections. It was shown that HGUW hold certain advantages over the traditional guided wave inspection for pipes, like the need for fewer sensors that can be permanently attached to the pipe as well as their capacity to perform tomographic reconstructions. Overall, the HGUW can be effectively utilized in large diameter pipes, typically greater than six inches, using less than 10 piezoelectric sensors for every two meters of pipe length.

As far as active monitoring is concerned, the use of the fundamental helical Lamb modes has been investigated. Findings suggested that the amplitude of the anti-symmetric A_0, as well as the energy ratio S_0/A_0 below the first cut-off frequencies, can be used as damage indicators in an adopted algebraic reconstruction technique to localize different defects. The accuracy of the ART is heavily dependent on the size of the scatterer and the excitation frequency. The reconstruction of the defect profile was possible using 2D acoustic modeling which is a high-frequency approximation. It was shown that for large defects, it is possible to reduce the wave propagation problem to 2D thus achieving faster calculations of HGUW travel time. The developed two-step corrosion localization-quantification algorithm was validated experimentally, and results suggest that it is highly efficient and robust when utilized in quantifying high-contrast corrosion-type defects.

For the second part of this report, a methodology was proposed for passively interrogating pipelines using a helical-type acoustic emission technique. It was found that developing corrosion mechanisms can be correlated with the energy and amplitude of the recorded AE activity. A new approach for recording the AE activity was proposed which considered an extended time window of each AE event in order for the helically propagated energy of a single AE source to be recorded as a single hit. The results of an accelerated corrosion test suggested that the rate of growth of large

uniform corrosion can be estimated using a b-value analysis on the amplitude of AE data recorded from a sparse sensor network.

5.2. Recommendations for future work

Based on the assumptions and major findings of this project, different elements of the active/passive HGUW inspection technique require further investigation. First, an extended numerical and experimental study should be conducted to establish the probability of detection (POD) of different corrosion sizes and profiles using the developed methodology. Such a study will define the confidence intervals of the method while highlighting the scenarios for which it is not effective. The two-step algorithm can be benefited by introducing additional parameters that describe the corrosion shape, beyond the longitudinal, circumferential, and remaining thickness that are already used. Also, an advance method to detect and classify the different orders of helical modes will be essential to avoid the manual mode selection and thus eliminate the ambiguity in mode identification. Furthermore, additional field testing on in-service pipelines will allow to examine the influence of noise and vibrations during data collection as well as to study the effect of internal pressure and pipeline coatings on the attenuation of the HGUW. In addition, this work pertains to straight pipes, although it has the potential to be expanded to account for complex geometries like pipe bends. A fundamental requirement for using the two-step algorithm is the baseline information of the pipe. Considering that in many instances this information is not available, baseline-free methods should be investigated. For example, an advanced numerical model can be developed instead, which can serve as an approximate predictor of the HGUW propagation on the pristine pipe. The present study was based on using contact transducers (i.e. PZT's) but future work can also examine the potential of using non-contact transducers like the air-coupled. Regarding the helical-type AE method, additional experimental testing is required with the consideration of internal pressure in the pipe. Typically, AE events correlate with the state of stress in a structure thus it is vital to establish the connection between the AE activity produced by a developing corrosion attack on the pipe and the stress redistribution. Lastly, the helical-type AE could also be applied for distinguishing different mechanisms of corrosion, like pitting, uniform, or stress corrosion.

5.3. Community outreach

During the 3rd year of the project, our team has been in close contact with Amerapex to discuss the overall progress of the project as well as identify potential field-testing applications. These virtual meetings took place in late Spring and Summer of 2021. The field test at Monroe Energy in Philadelphia was possible with the coordination and assistance of Dr. Ahmed Megharbi of Amerapex as well as Stephan Grossnicklaus of Amerapex who provided access to the facility and valuable information on the testing site. We have also established a connection with the Pipeline Research Council International (PRCI) and discussed possible applications of the HGUW inspection at their Technology Development Center in Houston. Multiple pipeline specimens have been identified with different corrosion levels and defects that we are interested in applying the developed technology.

5.4. Student involvement

A new Ph.D. student, Guan Wei Lee participated in the testing in Philadelphia. He was involved in all steps of the experimental testing from preparing the sensing units, instrumenting the pipe, and acquiring data. His involvement was critical and allowed him to gain experience in designing and executing field tests. Also, Konstantinos Sitaropoulos, a continuing Ph.D. student, has been involved with the experimental testing of the accelerated corrosion using the Acoustic Emission. Konstantinos research is dealing with the detection of leaks in underground water network systems thus his experience and input to this project have been extremely important.

References

[1] M. Askari, M. Aliofkhazraei, and S. Afroukhteh, “A comprehensive review on internal corrosion and cracking of oil and gas pipelines,” *J. Nat. Gas Sci. Eng.*, vol. 71, no. August, p. 102971, 2019.

[2] N. Sridhar, B. Thacker, A. Kale, C. Waldhart, O. Moghissi, and D. Burwell, “Internal corrosion direct assessment of gas transmission and storage lines,” Final Report 18.06484-200, Office of Pipeline Safety (OPS), Washington, DC, 2004.

[3] D. N. Alleyne, B. Pavlakovic, M. J. S. Lowe, and P. Cawley, “Rapid, long range inspection of chemical plant pipework using guided waves,” *Key Eng. Mater.*, vol. 270–273, no. I, pp. 434–441, 2004.

[4] P. Cawley, F. Cegla, and A. Galvagni, “Guided waves for NDT and permanently-installed monitoring,” *Insight Non-Destructive Test. Cond. Monit.*, vol. 54, no. 11, pp. 594–601, 2012.

[5] M. J. S. Lowe, D. N. Alleyne, and P. Cawley, “Defect detection in pipes using guided waves,” *Ultrasonics*, vol. 36, no. 1–5, pp. 147–154, 1998.

[6] H. Kwun, S. Y. Kim, and G. Light, “The magnetostrictive sensor technology for long range guided wave testing and monitoring of structures,” *Mater. Eval.*, vol. 61, pp. 80–84, Jan. 2003.

[7] M. J. S. Lowe, P. Cawley, J.-Y. Kao, and O. Diligent, “The low frequency reflection characteristics of the fundamental antisymmetric Lamb wave a0 from a rectangular notch in a plate,” *J. Acoust. Soc. Am.*, vol. 112, no. 6, pp. 2612–2622, 2002.

[8] A. Galvagni and P. Cawley, “The reflection of guided waves from simple supports in pipes,” *J. Acoust. Soc. Am.*, vol. 129, no. 4, pp. 1869–1880, 2011.

[9] P. Huthwaite and F. Simonetti, “High-resolution guided wave tomography,” *Wave Motion*, vol. 50, no. 5, pp. 979–993, 2013.

[10] P. Huthwaite, “Evaluation of inversion approaches for guided wave thickness mapping,” *Proc. R. Soc. A Math. Phys. Eng. Sci.*, vol. 470, no. 2166, p. 20140063, 2014.

[11] S. Livadiotis, A. Ebrahimkhanlou, and S. Salamone, “An algebraic reconstruction imaging approach for corrosion damage monitoring of pipelines,” *Smart Mater. Struct.*, vol. 28, no. 5, p. 055036, 2019.

[12] K. R. Leonard and M. K. Hinders, “Lamb wave tomography of pipe-like structures,” *Ultrasonics*, vol. 43, no. 7, pp. 574–583, 2005.

[13] J. R. Kwon, G. J. Lyu, T. H. Lee, and J. Y. Kim, “Acoustic emission testing of repaired storage tank,” *Int. J. Press. Vessel. Pip.*, vol. 78, no. 5, pp. 373–378, 2001.

[14] D. S. Dean, *Advances in acoustic emission*, vol. 14, no. 6. 1981.

[15] P. Cole and J. R. Watson, “Acoustic emission for corrosion detection,” *Adv. Mater. Res.*, vol. 13–14, pp. 231–236, 2006.

[16] K. R. Leonard and M. K. Hinders, “Guided wave helical ultrasonic tomography of pipes,” *J. Acoust. Soc. Am.*, vol. 114, no. 2, pp. 767–774, 2003.

[17] J. Fong, “A study of curvature effects on guided elastic waves,” PhD thesis, Imperial College London, London, UK, 2005.

[18] E. Dehghan-Niri and S. Salamone, “A multi-helical ultrasonic imaging approach for the structural health monitoring of cylindrical structures,” *Struct. Heal. Monit.*, vol. 14, no. 1, pp. 73–85, 2015.

[19] P. Belanger and P. Cawley, “Feasibility of low-frequency straight-ray guided wave tomography,” *AIP Conf. Proc.*, vol. 1096, pp. 153–160, 2009.

[20] B. Dubuc, A. Ebrahimkhanlou, and S. Salamone, “Effect of pressurization on helical guided wave energy velocity in fluid-filled pipes,” *Ultrasonics*, vol. 75, pp. 145–154, 2017.

[21] A. C. Kak and M. Slaney, *Principles of Computerized Tomographic Imaging*. IEEE Press. (C) 1988 Institute for Electrical and Electronic Engineers.

[22] Y. Lu and J. E. Michaels, “A methodology for structural health monitoring with diffuse ultrasonic waves in the presence of temperature variations,” *Ultrasonics*, vol. 43, no. 9, pp. 717–731, 2005.

[23] X. Zhao *et al.*, “Active health monitoring of an aircraft wing with embedded piezoelectric sensor/actuator network: I. Defect detection, localization and growth monitoring,” *Smart Mater. Struct.*, vol. 16, no. 4, pp. 1208–1217, 2007.

[24] E. B. Flynn and M. D. Todd, “Optimal placement of piezoelectric actuators and sensors for detecting damage in plate structures,” *J. Intell. Mater. Syst. Struct.*, vol. 21, no. 3, pp. 265–274, 2010.

[25] A. Ebrahimkhanlou, B. Dubuc, and S. Salamone, “Damage localization in metallic plate structures using edge-reflected lamb waves,” *Smart Mater. Struct.*, vol. 25 085035, 2016.

[26] P. Wilcox, “Modeling the Excitation of Lamb and SH Waves by Point and Line Sources,” vol. 206, no. April 2004, pp. 206–213, 2004.

[27] V. Giurgiutiu, “Tuned lamb wave excitation and detection with piezoelectric wafer active sensors for structural health monitoring,” *J. Intell. Mater. Syst. Struct.*, vol. 16, no. 2, pp. 291–305, 2005.

[28] P. B. Nagy, F. Simonetti, and G. Instanes, “Corrosion and erosion monitoring in plates and pipes using constant group velocity Lamb wave inspection,” *Ultrasonics*, vol. 54, no. 7, pp. 1832–1841, 2014.

[29] J. A. Sethian, “A fast marching level set method for monotonically advancing fronts,” *Proc. Natl. Acad. Sci. U. S. A.*, vol. 93, no. 4, pp. 1591–1595, 1996.

[30] K. R. Leonard, E. V Malyarenko, and M. K. Hinders, “Ultrasonic Lamb wave tomography,” *Inverse Probl.*, vol. 18, no. 6, pp. 1795–1808, 2002.

[31] A. J. Brath, F. Simonetti, P. B. Nagy, and G. Instanes, “Acoustic formulation of elastic guided wave propagation and scattering in curved tubular structures,” *IEEE Trans. Ultrason. Ferroelectr. Freq. Control*, vol. 61, no. 5, pp. 815–829, 2014.

[32] S. Livadiotis, A. Ebrahimkhanlou, and S. Salamone, “An algebraic reconstruction imaging approach for corrosion damage monitoring of pipelines,” *Smart Mater. Struct.*, vol. 28, no. 5, p. 055036, 2019.

[33] E. Ž. L. Mažeika, L. Draudvilienė, “Influence of the dispersion on measurement of phase and group velocities of Lamb waves,” *Ultrasound*, vol. 64, no. 4, pp. 18–21, 2009.

[34] R. Goldaran and A. Turer, “Application of acoustic emission for damage classification and assessment of corrosion in pre-stressed concrete pipes,” *Meas. J. Int. Meas. Confed.*, vol. 160, p. 107855, 2020.

[35] J. Rao, M. Ratassepp, D. Lisevych, M. H. Caffoor, and Z. Fan, “On-line corrosion monitoring of plate structures based on guided wave tomography using piezoelectric sensors,” *Sensors (Switzerland)*, vol. 17, no. 12, p. 2882, 2017.

[36] F. Moser, L. J. Jacobs, and J. Qu, “Modeling elastic wave propagation in waveguides with the finite element method,” *NDT E Int.*, vol. 32, no. 4, pp. 225–234, 1999.

[37] R. Howard and F. Cegla, “On the probability of detecting wall thinning defects with dispersive circumferential guided waves,” *NDT E Int.*, vol. 86, no. March 2016, pp. 73–82, 2017.

[38] R. Howard and F. Cegla, “Detectability of corrosion damage with circumferential guided waves in reflection and transmission,” *NDT E Int.*, vol. 91, no. July, pp. 108–119, 2017.

[39] C. L. Willey, F. Simonetti, P. B. Nagy, and G. Instanes, “Guided wave tomography of pipes with high-order helical modes,” *NDT E Int.*, vol. 65, pp. 8–21, 2014.

[40] B. K. and P. S. D. Hibbit, “ABAQUS / CAE User ’ s Manual,” *Ver. 6.10.1. ABAQUS Inc*, pp. 1–847, 2001.

[41] D. Alleyne and P. Cawley, “A two-dimensional Fourier transform method for the measurement of propagating multimode signals,” *J. Acoust. Soc. Am.*, vol. 89, no. 3, pp. 1159–1168, 1991.

[42] M. B. Drozdz, “Efficient Finite Element Modelling of Ultrasound Waves in Elastic Media,” PhD thesis, Imperial College London, London, UK, 2008.

[43] I. Bartoli, F. Lanza Di Scalea, M. Fateh, and E. Viola, “Modeling guided wave propagation with application to the long-range defect detection in railroad tracks,” *NDT E Int.*, vol. 38, no. 5, pp. 325–334, 2005.

[44] Y. Shen and V. Giurgiutiu, “Effective non-reflective boundary for Lamb waves: Theory, finite element implementation, and applications,” *Wave Motion*, vol. 58, pp. 22–41, 2015.

[45] M. Drozdz, L. Moreau, M. Castaings, M. J. S. Lowe, and P. Cawley, “Efficient numerical modelling of absorbing regions for boundaries of guided waves problems,” *AIP Conf. Proc.*, vol. 820 I, no. 2006, pp. 126–133, 2006.

[46] P. Rajagopal, M. Drozdz, E. A. Skelton, M. J. S. Lowe, and R. V. Craster, “On the use of absorbing layers to simulate the propagation of elastic waves in unbounded isotropic

media using commercially available Finite Element packages," *NDT E Int.*, vol. 51, pp. 30–40, 2012.

[47] B. Dubuc, S. Livadiotis, A. Ebrahimkhanlou, and S. Salamone, "Crack-induced guided wave motion and modal excitability in plates using elastodynamic reciprocity," *J. Sound Vib.*, vol. 476, 2020.

[48] P. T. Cole and J. R. Watson, "Acoustic Emission for Corrosion Detection," *Adv. Mater. Res.*, vol. 13–14, pp. 231–236, Feb. 2006.

[49] C. Jirarungsatian and A. Prateepasen, "Pitting and uniform corrosion source recognition using acoustic emission parameters," *Corros. Sci.*, vol. 52, no. 1, pp. 187–197, 2010.

[50] C. Jomdecha, A. Prateepasen, and P. Kaewtrakulpong, "Study on source location using an acoustic emission system for various corrosion types," *NDT E Int.*, vol. 40, no. 8, pp. 584–593, 2007.

[51] J. Li, G. Du, C. Jiang, and S. Jin, "The classification of acoustic emission signals of 304 stainless steel during stress corrosion process based on K-means clustering," *Anti-Corrosion Methods Mater.*, vol. 59, no. 2, pp. 76–80, 2012.

[52] S. Yuyama and T. Nishida, "Acoustic Emission Evaluation of Corrosion Damages in Buried Pipes of Refinery," *Acoust. Emiss. XI*, vol. 21, pp. 1–8, 2002.

[53] B. Dubuc, A. Ebrahimkhanlou, S. Livadiotis, and S. Salamone, "Inversion algorithm for Lamb-wave-based depth characterization of acoustic emission sources in plate-like structures," *Ultrasonics*, vol. 99, p. 105975, 2019.

[54] M. Takemoto, H. Cho, and H. Suzuki, "Lamb-Wave Acoustic Emission for Condition Monitoring of Tank Bottom Plates," *J. Acoust. Emiss.*, vol. 24, pp. 5–10, 2006.

[55] D. G. Aggelis and T. E. Matikas, "Effect of plate wave dispersion on the acoustic emission parameters in metals," *Comput. Struct.*, vol. 98–99, pp. 17–22, 2012.

[56] A. Farhidzadeh, S. Salamone, B. Luna, and A. Whittaker, "Acoustic emission monitoring of a reinforced concrete shear wall by b-value-based outlier analysis," *Struct. Heal. Monit.*, vol. 12, no. 1, pp. 3–13, 2013.

[57] I. S. Colombo, I. G. Main, and M. C. Forde, " Assessing Damage of Reinforced Concrete Beam Using ' b -value' Analysis of Acoustic Emission Signals ," *J. Mater. Civ. Eng.*, vol. 15, no. 3, pp. 280–286, 2003.

[58] B. Dubuc, A. Ebrahimkhanlou, and S. Salamone, “Corrosion monitoring of prestressed concrete structures by using topological analysis of acoustic emission data,” *Smart Mater. Struct.*, vol. 28, no. 5, 2019.

[59] J. Fong and M. J. S. Lowe, “Curvature Effect on the Properties of Guided Waves in Plates,” *AIP Conf. Proc.*, vol. 700, no. 1, pp. 126–133, 2004.

[60] E. Dehghan Niri, A. Farhidzadeh, and S. Salamone, “Determination of the probability zone for acoustic emission source location in cylindrical shell structures,” *Mech. Syst. Signal Process.*, vol. 60, pp. 971–985, 2015.

[61] S. Livadiotis, A. Ebrahimkhanlou, and S. Salamone, “Monitoring internal corrosion in steel pipelines: A two-step helical guided wave approach for localization and quantification,” *Struct. Heal. Monit.*, 2020.

[62] A. E. V Ciarlante, “Hsu, N.N. Acoustic Emissions Simulator. US Patent 4018084 A, 19 April 1977,” vol. 57, no. 3, 1977.

[63] B. Gutenberg, *Seismicity of the earth and associated phenomena*. Read Books Ltd, 2013.

[64] W. D. Smith, “The b-value as an earthquake precursor,” *43. Henthorn, D. I. 17th A. Rtp. Rts. ln,t. Afr. Gtol*, vol. 81, no. 2, pp. 57–62, 1971.

[65] M. V. M. S. Rao and K. J. Prasanna Lakshmi, “Analysis of b-value and improved b-value of acoustic emissions accompanying rock fracture,” *Curr. Sci.*, vol. 89, no. 9, pp. 1577–1582, 2005.

[66] C. G. Hatton, I. G. Main, and P. G. Meredith, “A comparison of seismic and structural measurements of scaling exponents during tensile subcritical crack growth,” *J. Struct. Geol.*, vol. 15, no. 12, pp. 1485–1495, 1993.

[67] “ASTM Standard F2832-11, Standard Guide for Accelerated Corrosion Testing for Mechanical Fasteners,” 2011.

[68] T. Kundu, “Acoustic source localization,” *Ultrasonics*, vol. 54, no. 1, pp. 25–38, 2014.

[69] C. Torrence and G. P. Compo, “Wavelet-Guide,” 1995.

[70] S. A Mallat, *A wavelet tour of signal processing*. Elsevier, 1999.